

BOSTON UNIVERSITY
GRADUATE SCHOOL OF ARTS AND SCIENCES

Dissertation

**STUDIES OF NON-STANDARD EFFECTS IN ATMOSPHERIC NEUTRINO
OSCILLATIONS AT SUPER-KAMIOKANDE**

by

WEI WANG

B.E., Harbin Institute of Technology, 1995
M.S., Harbin Institute of Technology, 1998
M.A., Boston University, 2001

Submitted in partial fulfillment of the
requirements for the degree of
Doctor of Philosophy

2007

Approved by

First Reader

Edward T. Kearns, Ph.D.
Associate Professor of Physics

Second Reader

Martin Schmaltz, Ph.D.
Assistant Professor of Physics

Third Reader

Ulrich Heintz, Ph.D.
Associate Professor of Physics

Acknowledgments

I must first express my deep gratitude to the North American graduate school system. It is only under this system that I was given the chance to pursue a Ph.D. degree in a field that I had little knowledge and background to start with. With its openness, I was able to build up my physics knowledge and eventually start advanced research.

Professor Ed Kearns, my academic advisor, is always a supporting mentor. Only with his patience could I conquer the difficulties and get back onto the right track in the field of research. His knowledge and understanding of experimental HEP gave me many enlightening moments. Professor Chris Walter who now is at Duke University helped me to start my research. I learned many things from him and have benefited much from his cheerful personality and high spirit. Thanks to Professor Mark Messier of Indiana University for his initiation on the studies in this dissertation. His early work provides much guidance for me in this field.

Working in the SciFi group of the K2K collaboration at the beginning of my Ph.D. program taught me many things. I would like to thank Professor Sakuda for his kindly support and guidance.

I would like to express my great appreciation to my other committee members: Professor Kenneth Lane, Professor Sidney Redner, Professor Ulrich Heintz and Professor Martin Schmaltz. I also include Professor James Rohlf, Professor Andrew Cohen, Professor Sekhar Chivukula and Professor Michael El-Batanouny. I have taken classes and sought other academic help from all of them. Some of them taught me when I knew little about advanced physics; some of them entered my physics life later while I started to take on more advanced topics. They are all great teachers and without their teaching, I could not have accomplished the research presented in this dissertation.

I want to thank the people in the ATMPD group: Professor Kajita, Professor Su-

lak, Professor Scholberg, Professor Habig, Professor Moriyama, Professor Okumura, Dr. Nakayama and Dr. Ishitsuka. I learned many things from them and I also had wonderful time working together with them.

Thanks to Professor Totsuka, Professor Suzuki, Professor Sobel, and Professor Stone; they led and are leading a very successful collaboration within which I learned how to do research and finished my Ph.D. program. Thanks to Professor Nakahata for his effort toward taking care of the Super-Kamiokande detector.

Thanks to the Kamioka Observatory faculty members and staff for taking care of the experiment and providing excellent technical support. Thanks to the SciFi group members for the great experience of working together.

I am very much grateful to Professor Kostelecky of Indiana University, Professor Pakvasa and Professor Learned of Hawaii University for their valuable suggestions and comments during my study.

I would also like to thank the people in the physics department of Carleton University, especially Professor Armitage and Professor Karlen, for their hospitality, kindness and teaching. I stayed only one year but I learned much.

Thanks to my fellow colleagues at Boston University. They are wonderful and helpful. The fun moments we shared those years are going to be an important part of my lifelong treasures.

At last, I would like to thank my parents for their constant encouragement since the very first day I entered school. Without their support, it would have been impossible for me to come to this point.

**STUDIES OF NON-STANDARD EFFECTS IN ATMOSPHERIC NEUTRINO
OSCILLATIONS AT SUPER-KAMIOKANDE**

(Order No.)

WEI WANG

Boston University Graduate School of Arts and Sciences, 2007

Major Professor: Edward T. Kearns, Associate Professor of Physics

ABSTRACT

Neutrino oscillation due to mass eigenstate mixing has become the standard theory accounting for both solar and atmospheric neutrino data. This explanation indicates that neutrinos have small but non-vanishing masses, which is a sign of new physics beyond the Standard Model. In this dissertation, we will compare the standard explanation with three types of alternative theories using Super-Kamiokande (SK) atmospheric neutrino data.

The first type of non-standard theory involves sterile neutrinos. By using the neutral current enhanced data samples of SK and by considering matter effect, we conclude it is unlikely that sterile neutrinos are responsible for SK atmospheric neutrino zenith angle distributions. Furthermore, we study the allowance of sterile neutrino admixture in atmospheric neutrino mixing and find an admixture of 23% sterile neutrino is allowed at 90% confidence level based on a 2+2 mass hierarchy model.

The second type of non-standard theory involves neutrino oscillation induced by violations of Lorentz invariance (LIV) and CPT symmetry (CPTV). The neutrino oscillations induced by the temporal components of the LIV and CPTV terms in the minimal Standard Model Extension (SME) have different energy and pathlength dependences compared to the standard oscillation. Our analysis indicates that it is unlikely to explain SK atmospheric neutrino data with the oscillation effects induced by the temporal components of the minimal SME separately. By treating LIV- and CPTV-induced oscillations as sub-dominant effects, limits on symmetry-breaking parameters are established.

The third category of non-standard theory involves vanishing neutrinos caused by neutrino decoherence and neutrino decay. Our study shows that it is unlikely to explain SK atmospheric neutrino zenith angle distributions using these two non-oscillatory models. By treating them as sub-dominant effects, limits on these two types of new physics are set based on several specific models.

Our study shows that the oscillation between muon neutrinos and tau neutrinos is the best model explaining SK atmospheric neutrino data among the models we test. In most cases, limits on new physics established in this study using SK atmospheric neutrino data are the best currently available.

Contents

Acknowledgements	iii
Abstract	v
Table of Contents	vi
List of Tables	x
List of Figures	xi
List of Abbreviations	xvi
1 Introduction	1
1.1 A brief history of the Standard Model neutrinos	1
1.2 Neutrino mass	2
1.3 Neutrino mixing and oscillation	4
1.3.1 Two-Flavor oscillation in vacuum	6
1.3.2 Two-flavor oscillation in matter	7
1.4 Beyond neutrino oscillation	9
2 Atmospheric Neutrinos	11
2.1 Primary cosmic rays	11

2.2	Atmospheric neutrino energy spectrum	14
2.3	Flavor ratios	15
2.4	Neutrino pathlength	18
2.5	Summary	20
3	Super-Kamiokande Experiment	22
3.1	Detector setup	23
3.2	Electronics and data acquisition	25
3.3	Detector calibration	26
3.3.1	Water properties	26
3.3.2	The absolute energy calibration	27
3.4	Neutrino interaction simulation	29
3.4.1	Elastic and quasi-elastic scattering	30
3.4.2	Single meson production	30
3.4.3	Deep inelastic scattering	31
3.4.4	Nuclear effects	32
3.5	The detector simulation	34
3.6	Summary	35
4	Super-Kamiokande Atmospheric Data	37
4.1	Data reduction	37
4.1.1	Reduction of fully-contained events	38
4.1.2	Reduction of partially-contained events	46
4.1.3	Reduction of upward-going muons	51
4.2	Event reconstruction	54
4.2.1	Vertex reconstruction	54
4.2.2	Ring counting	56

4.2.3	Particle identification	57
4.2.4	Precise vertex fitter	57
4.2.5	Momentum reconstruction	58
4.2.6	Upward-going muon event reconstruction	59
4.3	Summary	59
4.3.1	Systematic uncertainties of data reduction	60
4.3.2	Systematic uncertainties of event reconstruction	61
5	Mass-Induced $\nu_\mu - \nu_\tau$ Oscillation	63
5.1	Data preparation	64
5.1.1	Data binning	65
5.2	Oscillation Analysis	67
5.3	Results and Discussion	69
6	Constraints on Sterile Neutrinos	73
6.1	Comparison of $\nu_\mu - \nu_\tau$ and $\nu_\mu - \nu_s$ oscillations	74
6.1.1	Signatures of $\nu_\mu - \nu_s$ oscillation	74
6.1.2	Best-fits of two models	76
6.2	An admixture model	80
7	Violations of Lorentz Invariance and CPT	83
7.1	An overview LIV and CPTV	84
7.2	Allowed limits on LIV parameter	88
7.3	The violation of CPT symmetry	90
7.3.1	Testing the LSND mass squared splitting scale	90
7.3.2	Allowed limits of CPTV	92
7.4	Discussion	93

8	Neutrino Decay and Neutrino Decoherence	96
8.1	Neutrino decoherence	97
8.1.1	A pure neutrino decoherence model	99
8.1.2	Allowed limits of neutrino decoherence	102
8.2	Neutrino decay	106
8.2.1	Comparisons between neutrino decay and neutrino oscillation	107
8.2.2	Decay as a sub-dominant effect	109
8.3	Discussion	112
9	Conclusion	115
A	Outer Detector MC Tuning	116
A.1	An overview of OD Monte Carlo simulation	117
A.2	Tuning MC parameters	121
B	PC Reduction Systematic Uncertainty	125
B.1	Overview	126
B.2	Evaluation of ID cut uncertainties	128
B.3	The Uncertainty of OD cuts	131
B.4	Summary	132
	Bibliography	133

List of Tables

2.1	Systematic uncertainties on the atmospheric neutrino flux	21
3.1	Super-K detector related systematic uncertainties	35
3.2	Neutrino interaction related systematic uncertainties	36
4.1	Super-K data reduction uncertainties	62
4.2	Systematic uncertainties in event reconstruction	62
6.1	Portions of NC and CC events in the NC enhanced data samples	75
6.2	Chi-square difference breakdown ($\Delta\chi^2 = \chi_{\nu_\mu-\nu_s}^2 - \chi_{\nu_\mu-\nu_\tau}^2$)	79
8.1	Chi-square difference breakdown between the standard oscillation and the decoherence model ($\Delta\chi^2 = \chi_{decoherence}^2 - \chi_{\nu_\mu-\nu_\tau}^2$)	101
8.2	Chi-square difference breakdown between the standard oscillation and the decay case II model ($\Delta\chi^2 = \chi_{decayII}^2 - \chi_{\nu_\mu-\nu_\tau}^2$)	110

List of Figures

2.1	Primary cosmic ray fluxes of protons and helium nuclei [1]	12
2.2	Neutron flux fluctuation [2].	13
2.3	(top) The direction averaged atmospheric neutrino energy spectrum for $\nu_\mu + \bar{\nu}_\mu$; (bottom) The ratio of the calculated neutrino flux.	15
2.4	The flux ratio of $\nu_\mu + \bar{\nu}_\mu$ to $\nu_e + \bar{\nu}_e$ averaged over all zenith and azimuth angles versus neutrino energy.	16
2.5	The flux ratios of ν_μ to $\bar{\nu}_\mu$ and ν_e to $\bar{\nu}_e$ versus neutrino energy. The solid line is from [3], the dashed line is from [4] and dotted line is from [5]. . .	17
2.6	Distributions of neutrino pathlength in air	18
2.7	The averaged pathlength versus cosine of zenith angle	19
2.8	The flux of atmospheric neutrinos versus zenith angle. The solid line is from [3], the dashed line is from [4] and dotted line is from [5].	20
2.9	The flux of upward-going atmospheric neutrinos versus zenith angle. The solid line is from [3], the dashed line is from [4] and dotted line is from [5].	21
3.1	A schematic drawing of the Super-K detector (the number of ID PMTs during SK-II period was reduced by half)	24
3.2	The reconstructed $\pi^0 \rightarrow \gamma\gamma$ invariant mass	28

3.3	The determination of the absolute energy scale of Super-Kamiokande based on various techniques	28
3.4	The mean reconstructed energy of cosmic ray stopping muons divided by their range (upper) and muon-decay electron (lower) as a function of elapsed days during SK-I.	29
3.5	The scattering angle distribution by neutrino interactions off the H_2O target from the K2K experiment (data are from Fig.1(b) of Ref. [6]).	32
3.6	Charged current total cross section divided by E_ν for (a) neutrino and (b) anti-neutrino nucleon charged current interactions.	33
4.1	The number of hits in the largest outer detector cluster. Solid histogram is the MC prediction with neutrino oscillation considered.	39
4.2	Parent neutrino energy spectra	61
5.1	Binning strategy for the oscillation analysis	67
5.2	Chi-square contours on the $\Delta m^2 - \sin^2 2\theta$ parameter plane for $\nu_\mu - \nu_\tau$ mixing	70
5.3	Chi-square contours on the $\Delta m^2 - \sin^2 2\theta$ parameter plane for $\nu_\mu - \nu_\tau$ mixing	70
5.4	1D chi-square projections	71
5.5	The distribution of normalized pulls with its Gaussian fit results	72
6.1	Zenith angle distributions of neutral current enhanced samples. Left: sub-GeV; right: multi-GeV	75
6.2	Survival probabilities of muon neutrinos crossing the Earth	76
6.3	χ^2 contours of $\nu_\mu - \nu_\tau$ oscillation (with NC enhanced samples)	77
6.4	χ^2 contours of the $\nu_\mu - \nu_s$ oscillation (with NC enhanced samples)	78

6.5	Comparison of the best-fit zenith angle distributions of $\nu_\mu - \nu_\tau$ and $\nu_\mu - \nu_s$ oscillations	79
6.6	Distributions of the normalized pull terms of $\nu_\mu - \nu_\tau$ and $\nu_\mu - \nu_s$ oscillations	80
6.7	A case of 2+2 mass hierarchy and four-flavor mixing	81
6.8	The ν_s admixture allowance	82
7.1	Allowed regions for parameters κ and α	87
7.2	χ^2 versus α for a general oscillation formula	88
7.3	Chi-square contours of LIV. Left: $\eta = 0$; Right: $\eta = \pi$	90
7.4	Contour plot of the <i>ad hoc</i> CPTV model chi-square. Dash line is defined by $\Delta m^2 = \Delta \bar{m}^2$	91
7.5	Chi-square contours considering CPTV as a sub-dominant effect	93
8.1	Chi-square contours on the $\sin^2 2\theta - \gamma_0$ plane	100
8.2	Comparison of pull terms of $\nu_\mu - \nu_\tau$ and decoherence	102
8.3	Comparison of pull terms of $\nu_\mu - \nu_\tau$ and decoherence	103
8.4	Allowed decoherence limits for $\gamma = \gamma_0$ case	104
8.5	Allowed decoherence limits for $\gamma = \gamma_0/E$ case	104
8.6	Allowed decoherence limits for $\gamma = \gamma_0(E/GeV)^2$ case	105
8.7	Chi-square contours of neutrino decay case I	108
8.8	Chi-square contours of neutrino decay case II	109
8.9	Comparison of pull terms of the $\nu_\mu - \nu_\tau$ oscillation and the neutrino decay case 2	110
8.10	Comparison of pull terms of the $\nu_\mu - \nu_\tau$ oscillation and the neutrino decay case 2	111
8.11	Chi-square contours of neutrino oscillation + neutrino decay in linear scale	112

8.12	Chi-square contours of neutrino oscillation + neutrino decay in logarithm scale	113
8.13	The non-zero local minimum of neutrino decay	114
A.1	OD MC performance before this tuning. Upper two: charge distributions inside/outside of the time window and; lower two: hit time and number of hits distributions (dots are observation and solid histograms are MC) . . .	118
A.2	SPE pulse height distribution of Hamamatsu R1408	119
A.3	Measured charge distribution of Hamamatsu R1408	119
A.4	Distribution of centroids using exponential SPE distribution model (the conversion factor to number of photoelectrons is around 2 in <code>apdet sim</code>)	120
A.5	OD charge distribution inside/outside of time window with the tuned MC simulation compared with observation	123
A.6	OD hit distribution with the tuned MC simulation compared with observation	124
B.1	Distributions of n_{pe200} of the final PC sample. The circles are the final PC sample; triangle are MC	128
B.2	$\cos \theta_{fit-first}$ distributions of MC and observed data	129
B.3	Distribution of <i>mugood</i> with <i>mudistance</i> ≥ 3000	130
B.4	Distribution of d_{corner}	130
B.5	Distributions produced by another set of MC parameters	132

List of Abbreviations

ADC	Analog to Digital Converter
CC	Charged Current
CPTV	CPT Violation
DAQ	Data Acquisition
FC	Fully Contained
FRP	Fiber Reinforced Plastic
GPS	Global Positioning System
GRB	Gamma-ray Burst
GUT	Grand Unified Theories
HE	High Energy
ID	Inner Detector
IMB	Irvine Michigan Brookhaven
K2K	KEK to Kamioka
KEK	Ken Energy Kenkyusho (High Energy Accelerator Research Organization)
LE	Low Energy
LEP	Large Electron-Positron Storage Ring
LIV	Lorentz Invariance Violation
LSND	Liquid Scintillator Neutrino Detector
MACRO	Monopole and Cosmic-ray Observatory

MC	Monte Carlo
MINOS	Main Injector Neutrino Oscillation Search
NC	Neutral Current
OD	Outer Detector
PC	Partially Contained
PMT	Photomultiplier Tube
QTC	Charge to Time Converter
SK	Super-Kamiokande
SLE	Super low energy
SM	Standard Model
SNO	Sudbury Neutrino Observatory
SPE	Single Photoelectron
TDC	Time to Digital Converter
TQ	Time Charge
VME	Versa Module Europe

Chapter 1

Introduction

Neutrinos were first postulated by W. Pauli in December 1930 [7] to explain the continuous energy spectrum of electrons from nuclear β decay. Ever since then, physicists have been performing different experiments and proposing many kinds of theories to explore and to explain the behavior of this “ghostly” particle.

In this chapter, we will first briefly go through the history of neutrinos. Then, after introducing neutrino mass theories and experimental results, we will talk about the phenomenology of neutrino mixing and neutrino oscillation.

1.1 A brief history of the Standard Model neutrinos

Twenty-six years after W. Pauli postulated neutrinos, in 1956, they were detected by F. Reines and C. Cowan [8]. The neutrinos they detected were anti-neutrinos of electron type from nuclear reactors. In the following year, M. Goldhaber, L. Grodzins and A. W. Sunyar experimentally deduced that neutrinos are always “left-handed” [9]. In 1962, J. Steinberger, M. Schwartz, L. Lederman and their collaborators found a new kind of neutrino and confirmed that neutrinos actually have different flavors [10]. The new neutrino

they found was of muon type since it was always associated with muon creation or decay.

In 1975, a group of scientists led by Martin L. Perl found a new kind of lepton, τ , at Stanford Linear Accelerator Center (SLAC) [11]. This is the first member of the third generation of the Standard Model (SM) and the discovery strongly suggested the existence of the tau type neutrino ν_τ . Though tau neutrinos were not directly detected until 2000 at the DONUT experiment in Fermilab [12], people have not doubted their existence.

In late 1980's, by measuring the invisible decay width of the Z^0 produced in the e^+e^- collider LEP, particle physicists confirmed there are only three generations of light active neutrinos [13].

In the Standard Model, neutrinos are spin half and left-handed (right-handed for antineutrinos) fermions, and they only participate weak interaction. The results from collider experiments indicate neutrinos only have three different flavors. The absence of right-handed neutrinos suggests that neutrinos are massless since right-handed neutrinos are needed by the mass term in the Lagrangian.

1.2 Neutrino mass

Although the Standard Model considers neutrinos as massless particles, the experimental efforts to measure their masses have never stopped since the postulation of neutrinos. However, all the measurements so far are consistent with zero. The current best limit from direct measurements comes from the tritium β decay experiments at Mainz and Troitsk [14]. Their sensitivity reaches around $2 \text{ eV}/c^2$. The first experimental support for non-zero neutrino masses came from the discovery of neutrino oscillations [15]. We will discuss the phenomenology of neutrino oscillations briefly in the next section.

Due to neutrino mixings, the masses measured in β decay experiments are effective masses which have contributions from all three mass eigenstates and three mixing angles.

The next generation direct measurement experiment Karlsruhe Tritium Neutrino Experiment (KATRIN) expects to enhance the sensitivity by one order of magnitude down to $\sim 0.2 \text{ eV}/c^2$ [16]. There are also indirect constraints from cosmological large scale structure measurements, which are sensitive to the sum of all the neutrino masses [17, 18]. By combining the Wilkinson Microwave Anisotropy Probe (WMAP) measurements on the anisotropies of the cosmic microwave background (CMB) and the Sloan Digital Sky Survey (SDSS) data on galaxy clustering properties, Tegmark *et al* set a limit of $\sum m_\nu < 1.7 \text{ eV}$ at 95% confidence level [19]. This limit can be improved further down to 0.42 eV by including weak lensing, Ly α forest, and supernovae data [20].

Theoretically, we can give neutrinos masses by doing some extensions to the Standard Model. Basically, there are several ways [21, 22]. The standard approach is that neutrino masses come from the interaction with Higgs field, just like other fermions in the Standard Model (SM), the neutrino mass term reads as:

$$\mathcal{L}_D = -(\bar{\nu}_L m_D^\dagger \nu_R + \bar{\nu}_R m_D \nu_L). \quad (1.1)$$

Where $m_D = Y_\nu \langle H \rangle$ is the Dirac mass generated by interacting with the Higgs field H and Y_ν is the coupling constant. This requires the presence of right-handed neutrinos ν_R which must be sterile, *i.e.* they do not interact with matter. However, it is rather unnatural that the coupling of neutrinos with the Higgs field Y_ν must be extremely small compared to other fermions due to the smallness of neutrino masses.

Neutrinos have zero conserved charges (electric and color), which gives the possibility that neutrinos could be Majorana particles, *i.e.* neutrinos and antineutrinos are the same particles. A Majorana mass term can be written as $-\frac{1}{2}m\bar{\psi}\psi$ for a Majorana spinor ψ , where ψ is self-conjugate: $\psi = \psi^c$. This possibility gives rise to a very elegant and natural way to generate the smallness of neutrino masses: “seesaw mechanism” [23, 24, 25, 26, 27].

Using the charge conjugate fields ν_L^c and ν_R^c , $\bar{\nu}_R\nu_L$ can be rewritten as $\frac{1}{2}(\bar{\nu}_R\nu_L + \bar{\nu}_L^c\nu_R^c)$ and $\bar{\nu}_L\nu_R$ can be rewritten in the similar way. Then, the Lagrangian term has both Dirac masses and Majorana masses can be written as [28]:

$$\mathcal{L}_{seesaw} = -\frac{1}{2}(\overline{\nu_L^c} \quad \overline{\nu_R}) \begin{pmatrix} m_L & m_D^T \\ m_D & M_R \end{pmatrix} \begin{pmatrix} \nu_L \\ \nu_R^c \end{pmatrix} + \text{h.c.}$$

Where m_D is the Dirac mass matrix, m_L is the Majorana mass matrix of left-handed neutrinos and M_R is the Majorana mass matrix of right-handed neutrinos. Seesaw mechanism can be best explained in a case with just one family of neutrinos. Further, let us assume $m_L = 0$ and $M_R \gg m_D$. We have a 2×2 mass matrix

$$M = \begin{pmatrix} 0 & m_D \\ m_D & M_R \end{pmatrix}.$$

This matrix has two eigenvalues, given approximately by M_R and $-m_D^2/M_R$. Though m_D is naturally at the scale of charged lepton masses, a tiny neutrino mass of scale $\sim m_D^2/M_R$ can still be generated since $M_R \gg m_D$.

1.3 Neutrino mixing and oscillation

Along with the early discoveries of neutrino physics in 1958, Pontecorvo proposed the possibility that neutrino and antineutrino might oscillate in a way resembling the $K^0 - \bar{K}^0$ system [29]. In 1962, after the discovery of the muon neutrino flavor, Maki, Nakagawa and Sakata proposed that if neutrino mass eigenstates do not coincide with neutrino flavor eigenstates, then mixing will happen, which will cause oscillation phenomenon of the sort we discovered with Super-K [30]. In 1968, Gribov and Pontecorvo in Ref. [31] pro-

posed neutrino oscillation as a solution to the solar neutrino deficit problem discovered by R. Davis *et al* [32, 33]. Super-Kamiokande provided strong evidence of atmospheric neutrino oscillations in 1998 [15] and long baseline neutrino experiments K2K and MINOS have consistent results with Super-Kamiokande [6, 34]. Solar and reactor neutrino experiment data are also explained by neutrino oscillations [35, 36].

In the case of three flavors, the mass eigenstates and the flavor eigenstates are connected by an unitary matrix U_{PMNS} ,

$$\begin{pmatrix} \nu_e \\ \nu_\mu \\ \nu_\tau \end{pmatrix} = U_{PMNS} \begin{pmatrix} \nu_1 \\ \nu_2 \\ \nu_3 \end{pmatrix},$$

where the mixing matrix U_{PMNS} is generally expressed in three mixing angles, θ_{12} , θ_{23} , and θ_{13} , and a phase term δ ,

$$U_{PMNS} = \begin{pmatrix} 1 & 0 & 0 \\ 0 & \cos \theta_{23} & \sin \theta_{23} \\ 0 & -\sin \theta_{23} & \cos \theta_{23} \end{pmatrix} \begin{pmatrix} \cos \theta_{13} & 0 & \sin \theta_{13} e^{-i\delta} \\ 0 & 1 & 0 \\ -\sin \theta_{13} e^{i\delta} & 0 & \cos \theta_{13} \end{pmatrix} \\ \times \begin{pmatrix} \cos \theta_{12} & \sin \theta_{12} & 0 \\ -\sin \theta_{12} & \cos \theta_{12} & 0 \\ 0 & 0 & 1 \end{pmatrix}$$

Based on the results from Chooz and Palo Verde experiments, θ_{13} is very small, less than 0.16 at 90% C.L. [37, 38, 39] and the scale of the solar mass-squared splitting is several orders of magnitudes smaller than the atmospheric one. So, for most experiments, two-

flavor mixing analysis is sufficient.

1.3.1 Two-Flavor oscillation in vacuum

Let's study the $\nu_\mu - \nu_\tau$ mixing case:

$$\begin{pmatrix} \nu_\mu \\ \nu_\tau \end{pmatrix} = \begin{pmatrix} \cos \theta & \sin \theta \\ -\sin \theta & \cos \theta \end{pmatrix} \begin{pmatrix} \nu_2 \\ \nu_3 \end{pmatrix}$$

In the relativistic limit, which applies to most cases due to the small masses of neutrinos, the dispersion relation could be written as $E = p + m^2/2p$. Assuming the two mass eigenstates have the same momentum, the Hamiltonian of the system is:

$$H = \begin{pmatrix} p + \frac{m_2^2}{2p} & 0 \\ 0 & p + \frac{m_3^2}{2p} \end{pmatrix}. \quad (1.2)$$

What are produced and detected in experiments are weak interaction, *i.e.* flavor eigenstates. If a neutrino is produced at time $t = 0$, after time t , the wave packets will be at a flavor eigenstate: $|\psi(t)\rangle = \sum_{i=2}^3 \phi_i(t)|\nu_i\rangle$. And the evolution equation is:

$$i \frac{d}{dt} \begin{pmatrix} \phi_2(t) \\ \phi_3(t) \end{pmatrix} = H \begin{pmatrix} \phi_2(t) \\ \phi_3(t) \end{pmatrix}, \quad (1.3)$$

where $\phi_i(0) = U_{\alpha i}$, $\alpha = \mu$ or τ depending the initial flavor state of the experiment. The solution to Eq. 1.3 is:

$$\begin{pmatrix} \phi_2(t) \\ \phi_3(t) \end{pmatrix} = e^{-iHt} \begin{pmatrix} \phi_2(0) \\ \phi_3(0) \end{pmatrix}.$$

For the atmospheric neutrino case, if a ν_μ with energy E was created in the upper atmosphere, after traveling a distance L , the system is in the following state:

$$|\psi(t)\rangle = \cos \theta e^{i\Delta m^2 L/2E} |\nu_2\rangle + \sin \theta e^{-i\Delta m^2 L/2E} |\nu_3\rangle,$$

where $\Delta m^2 = m_3^2 - m_2^2$, assuming $m_3 > m_2$. We have applied approximations $E \simeq p$ and $L \simeq ct$ during the derivation. Then the probability we find it still in the muon neutrino state, *i.e.*, the survival probability is,

$$P_{\nu_\mu \rightarrow \nu_\mu} = |\langle \nu_\mu | \psi(t) \rangle|^2 = 1 - \sin^2 2\theta \sin^2 \frac{\Delta m^2 L}{4E}, \quad (1.4)$$

1.3.2 Two-flavor oscillation in matter

In the previous section, we derived the neutrino survival probability due to mass eigenstate mixing in the vacuum. However, when neutrinos propagate in matter, if different interaction states have different forward scattering potentials due to the different interactions with the medium, then the Hamiltonian is different from Eq. 1.2, thus the survival probability formula is modified. This phenomenon is called matter effect and it was first pointed out by L. Wolfenstein in [40, 41].

Among the three SM flavors, the matter effect only exists between the mixing of ν_e and ν_μ or ν_e and ν_τ for media containing electrons, which give ν_e 's an extra forward scattering potential due to the extra charged current interaction. The neutral current interaction is the same for all three flavors. However, if there are new flavor eigenstates, say sterile neutrinos, which we will discuss in later chapters, their interactions with matter are different from the SM interactions, and there will also be matter effects between them and the three SM flavors.

Without losing generality, we study a two-flavor case here: the mixing between two interaction eigenstates α and β , the mass eigenvalues are m_a and m_b ($m_b > m_a$ and $\Delta m^2 \equiv m_b^2 - m_a^2$), and the mixing angle between them is θ . Let us assume the interaction eigenstate α gains an extra forward scattering potential ζ in the medium considered, then the Hamiltonian becomes (in the previous section, we see that $pI_{2 \times 2}$ plays no role in the final results so we omit it from the Hamiltonian. Also we will apply $p \simeq E$ and $x \simeq ct$ from now on:

$$H = \begin{pmatrix} \frac{m_a^2}{2E} & 0 \\ 0 & \frac{m_b^2}{2E} \end{pmatrix} + \begin{pmatrix} \cos \theta & -\sin \theta \\ \sin \theta & \cos \theta \end{pmatrix} \begin{pmatrix} \zeta & 0 \\ 0 & 0 \end{pmatrix} \begin{pmatrix} \cos \theta & \sin \theta \\ -\sin \theta & \cos \theta \end{pmatrix}. \quad (1.5)$$

If ζ does not depend on time, by diagonalizing this Hamiltonian, we can solve the evolution Eq. 1.3.

Suppose we obtain two eigenvalues: $\frac{M_2^2}{2E} > \frac{M_1^2}{2E}$, by diagonalizing H in Eq. 1.5, we can calculate the effective mass-squared splitting Δm_M^2 and the effective mixing angle θ_M in matter:

$$\begin{cases} \Delta m_M^2 = M_2^2 - M_1^2 = \Delta m^2 \sqrt{(\cos 2\theta - \frac{2E\zeta}{\Delta m^2})^2 + \sin^2 2\theta} \\ \sin 2\theta_M = \sin 2\theta \frac{\Delta m^2}{M_2^2 - M_1^2} = \frac{\sin 2\theta}{\sqrt{(\cos 2\theta - \frac{2E\zeta}{\Delta m^2})^2 + \sin^2 2\theta}} \end{cases}.$$

However, in the medium with varied density, which means ζ is time dependent, the analytical results above are not valid any more. In this case, we can divide the neutrino trajectory into different sections, x_1, x_2, \dots, x_n , approximating each small section with a constant densities and calculate the survival probability by evolution method:

$$\begin{pmatrix} \phi_a(x) \\ \phi_b(x) \end{pmatrix} = e^{-iH_n x_n} e^{-iH_{n-1} x_{n-1}} \dots e^{-iH_1 x_1} \begin{pmatrix} \phi_a(0) \\ \phi_b(0) \end{pmatrix}, \quad (1.6)$$

which form a flavor state $|\psi(x)\rangle = \sum_{i=a}^b \phi_i(x)|\nu_i\rangle$, and the probability finding flavor α is $P_\alpha = |\langle\nu_\alpha|\psi(x)\rangle|^2$ [42].

1.4 Beyond neutrino oscillation

Recently, mass eigenstate mixing induced neutrino oscillation has become the standard theory accounting for the solar, atmospheric and long baseline neutrino experiments. However, there are other alternative theories which can also induce neutrino oscillations or can cause effects similar to some of the experimental observations.

Mass eigenstate mixing induced neutrino oscillations are basically due to the fact that different mass eigenstates have different energies for the same momentum: $E_i = pc + p^2/2m_i$. Thus, in principle, any theories which can modify the dispersion relation to meet this condition can induce neutrino oscillations, such as Fermi point splitting [43], violations of Lorentz invariance (LIV) and CPT (CPTV) [44, 45].

Besides the non-standard theories which can induce neutrino oscillations, there is also another category of alternatives which can cause neutrino vanishing instead of oscillation, for example, neutrino decoherence [46, 47, 48, 49, 50] and neutrino decay [51]. Some models based on these theories can also explain some experimental data quite well.

Whether these non-standard effects can explain neutrino experiment data is certainly worth investigating. On the other hand, these alternatives are new physics beyond the Standard Model and testing them is of many theoretical importance. Atmospheric neutrino data, as we will introduce later, cover a wide range of energies, pathlengths and matter densities, will prove to be a powerful tool to explore new physics.

In the following chapters, we will introduce atmospheric neutrinos, the Super-Kamiokande experiment with which we do the observation, present the studies on mass-induced neutrino oscillations, introduce some of the alternative theories and test their plausibility and

allowed limits based on the current data.

Chapter 2

Atmospheric Neutrinos

In the neutrino oscillation section of Chapter 1, we showed that neutrino oscillation probability basically depends on two kinetic variables: the energy and the pathlength. Naturally, we also need the flavor information. We will briefly introduce the properties of atmospheric neutrino fluxes from these three perspectives. One fact needs to be pointed out is that the neutrino flux presented here is calculated before considering the neutrino oscillation effect and except for the general principles, the values are for the Super-Kamiokande site only, since the flux is affected by the geomagnetic field.

2.1 Primary cosmic rays

Atmospheric neutrinos are produced in cosmic ray interactions in the upper atmosphere. Thus, the atmospheric neutrino flux is a convolution of the primary cosmic ray spectrum at the production point with the yield of neutrinos per primary particle. Roughly speaking, primary cosmic ray consists of 90% protons, 9% alpha particles and a small portion of other kinds of heavy nuclei [52]. Figure 2.1 shows the measured fluxes of protons and helium nuclei by different experiments [1].

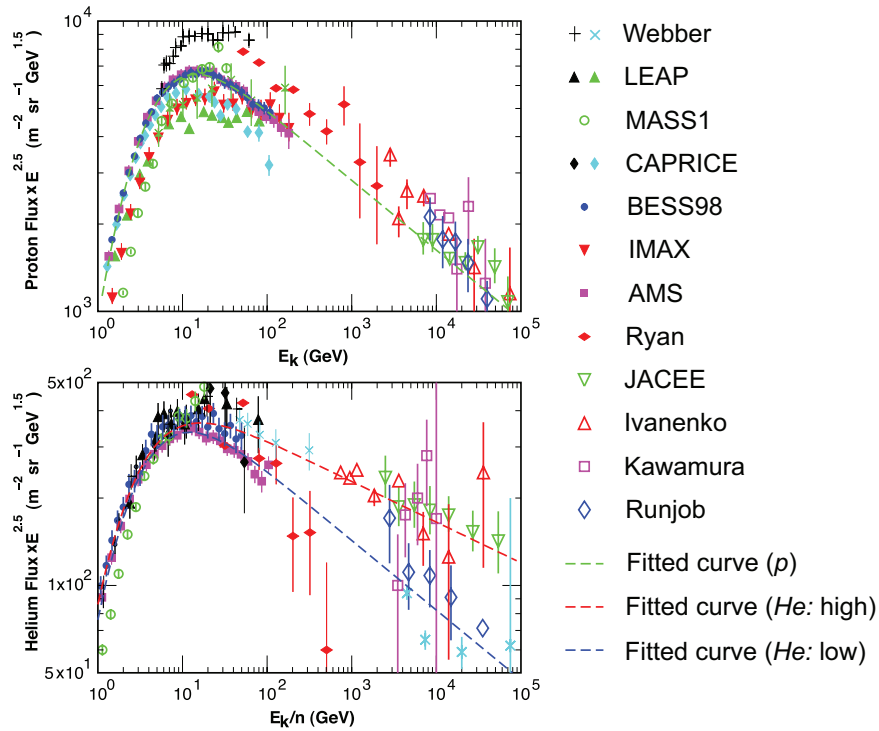


Figure 2.1: Primary cosmic ray fluxes of protons and helium nuclei [1]

Cosmic rays are isotropic when they reach the vicinity of the Earth. But, in order to reach the upper atmosphere and interact with the air nucleus, these charged particles have to pass through the geomagnetic field, which produces local effects — the neutrino flux is location dependent [1] since the geomagnetic field varies at different locations. The flux data we present here is for the Super-Kamiokande site only.

Interactions of primary cosmic ray particles with air nuclei produce mesons which are mainly pions and kaons. Subsequently, neutrinos are produced in the decay chains of these mesons. For example, the decay chain from pions are:

$$\begin{aligned}
 \pi^{\pm} &\rightarrow \mu^{\pm} + \nu_{\mu}/\bar{\nu}_{\mu} \\
 \mu^{\pm} &\rightarrow e^{\pm} + \nu_e/\bar{\nu}_e + \bar{\nu}_{\mu}/\nu_{\mu}
 \end{aligned}
 \tag{2.1}$$

Kaon decays follow the similar chains.

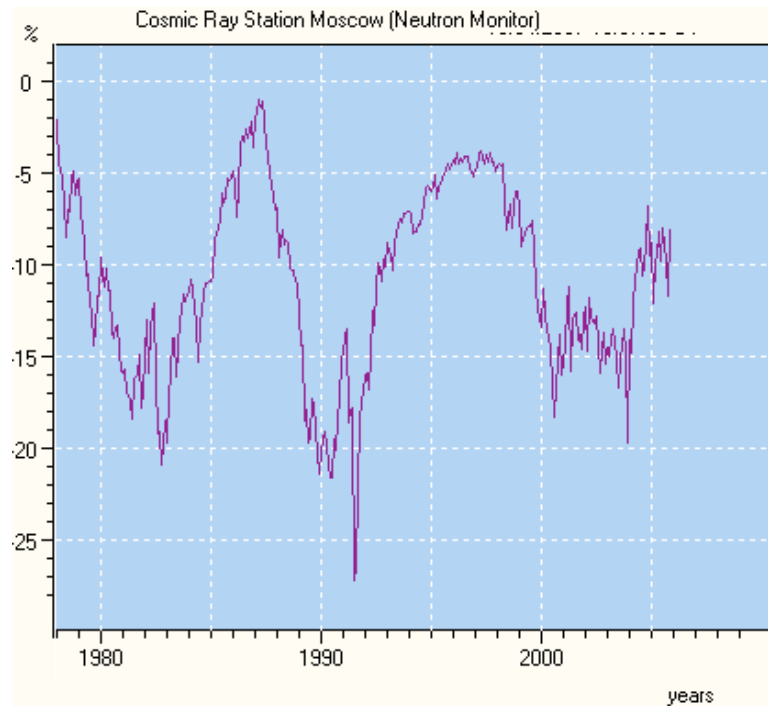


Figure 2.2: Neutron flux fluctuation [2].

Solar activity effects the primary cosmic rays and thus on the atmospheric neutrino flux. The minimum neutrino flux occur at times of high solar activity.

Figure 2.2 shows the neutron monitor data from Moscow Neutrino Monitor [2]. According to the cosmic ray proton, helium and neutron measurements [53, 54, 2], during the SK-I period, the cosmic ray flux was near the solar minimum until the summer of 1999, rapidly decreased during the next year, and was at the minimum value consistent with solar maximum from summer of 2000 until Super-Kamiokande I stopped taking data in July 2001. Therefore, the atmospheric neutrino Monte Carlo is calculated for 3 years of solar minimum, 1 year of changing activity, and 1 year of solar maximum for Super-K I. During the SK-II period, which is from Jan 2003 to October 2005, there are about one year solar minimum in 2003, and two years of changing activity during the 2004 and 2005 period.

2.2 Atmospheric neutrino energy spectrum

Roughly speaking, low energy neutrinos around 1 GeV are mainly produced by the primary fluxes around 10 GeV. At this energy range, cosmic ray fluxes are affected by solar activity and by the geomagnetic field due to their low rigidities. Neutrinos above 100 GeV are mainly from primary cosmic rays with energies greater than 1000 GeV which are free of the effects of solar activity and the rigidity cutoff. But details of the higher energy primary cosmic ray flux are not as well measured.

Following the primary interactions of cosmic ray particles with the air nuclei, the propagation and decay of secondary particles are simulated [1]. The calculated energy spectra of atmospheric neutrinos at Kamioka site are shown in Fig. 2.3 (top). Fig. 2.3(bottom) shows the comparison of different calculations. The fluxes calculated in Ref. [4] (solid line) and Ref. [5] (dashed line) are normalized by the flux in Ref. [3].

Below 10 GeV, the difference among different calculations is around 10%. This is the combined effects of the uncertainty of the primary cosmic ray flux measurements [55, 56], which is about 5% below 100 GeV, and different hadronic interaction models used in calculations.

Above 100 GeV, the primary cosmic ray spectrum and compositions are less well known. Therefore, for neutrino energies much higher than 10 GeV, the uncertainties in the absolute neutrino flux are much larger. The index of low energy (<100 GeV) proton spectra is -2.74 ± 0.01 according to Ref. [1]. However, this spectrum does not fit well to the high energy part. Ref. [3] suggests allowing a different spectral index for the protons above 100 GeV: the best fit value is -2.71 . Also, it is discussed in Ref. [1] that the spectrum index for the He flux can be fit by either -2.64 or -2.74 , shown in Fig. 2.1. So, there could be 0.10 uncertainty in the spectrum index for He. The spectrum indices for heavier nuclei have uncertainties larger than 0.05 [1].

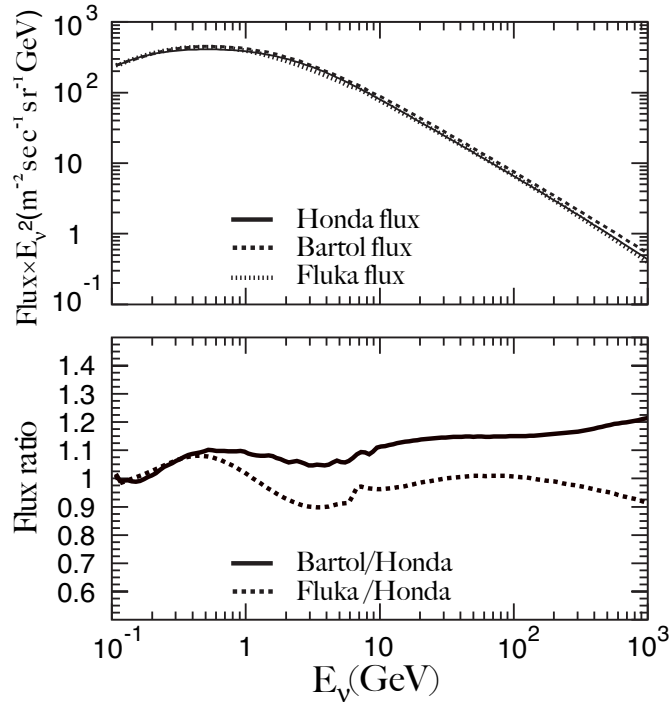


Figure 2.3: (top) The direction averaged atmospheric neutrino energy spectrum for $\nu_\mu + \bar{\nu}_\mu$; (bottom) The ratio of the calculated neutrino flux.

Taking the flux weighted average of these spectrum index uncertainties, we assign 0.03 and 0.05 for the uncertainties in the energy spectrum index in the primary cosmic ray energy spectrum below and above 100 GeV, respectively.

2.3 Flavor ratios

There are mainly two factors affecting the flavor ratio: neutrino energy and the relative contributions from kaons and pions. Figure 2.4 shows the ratio of $\nu_\mu + \bar{\nu}_\mu$ to $\nu_e + \bar{\nu}_e$ as a function of the neutrino energy. Solid, dashed and dotted lines show the prediction by [3], [4] and [5], respectively. The angle dependence has been integrated out. In the low energy region less than about 5 GeV, most of the neutrinos are produced by the decay chain of pions in Eq. 2.1. To a very good approximation, the ratio is around 2. The uncertainty

of this energy range is about 3%, which is estimated by comparing the three calculation results.

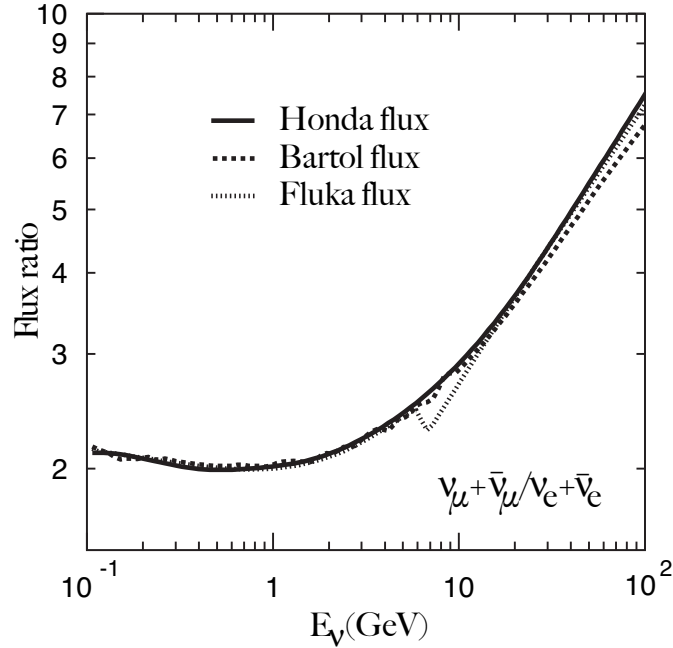


Figure 2.4: The flux ratio of $\nu_\mu + \bar{\nu}_\mu$ to $\nu_e + \bar{\nu}_e$ averaged over all zenith and azimuth angles versus neutrino energy.

However, as neutrino energy increases, the parent muons are more likely to reach the ground before they decay and the contribution from K decay increases: at 10 GeV, about 10% of electron type neutrinos and 20% of muon type are from K ; it increases to more than 30% at 100 GeV for both flavors. And the uncertainty of K/π production ratio [57, 58] in this energy region is as big as 20%, which causes a bigger uncertainty on the flavor ratio in the energy range of 10 to 100 GeV. As seen from Fig. 2.4, the difference of the calculated $\nu_\mu + \bar{\nu}_\mu$ to $\nu_e + \bar{\nu}_e$ ratio is as large as 10% at 100 GeV. Above 5 GeV, we assumed that the uncertainty linearly increases with $\log E_\nu$ from 3% at 5 GeV to 10% at 100 GeV.

Although the Super-K detector does not distinguish the signs of the charges, the observation is still affected by $\nu/\bar{\nu}$ ratio since they have different interaction cross sections and the oppositely charged final state particles produce different responses in the detector.

Also, some physics effects are indeed sensitive to the $\nu/\bar{\nu}$ ratio, *e.g.*, the matter effect and CPT violation (CPTV) models which we will discuss in this dissertation.

Figure 2.5 shows the calculated flux ratios ν_μ to $\bar{\nu}_\mu$ and ν_e to $\bar{\nu}_e$. Solid, dashed and dotted lines show the prediction by Honda *et al* in Ref. [3], Barr *et al* in Ref. [4] and Battistoni *et al* in Ref. [5], respectively (same key as Fig. 2.4). Below 10 GeV, for both ratios, different calculations agree to about 5%. But the disagreement gets larger as neutrino energy increases. The systematic uncertainties on the $\nu/\bar{\nu}$ ratio are assumed to be 5% below 10 GeV and linearly increase with $\log E_\nu$ to 10% and 25% at 100 GeV, for the ν_e to $\bar{\nu}_e$ and ν_μ to $\bar{\nu}_\mu$ ratios, respectively.

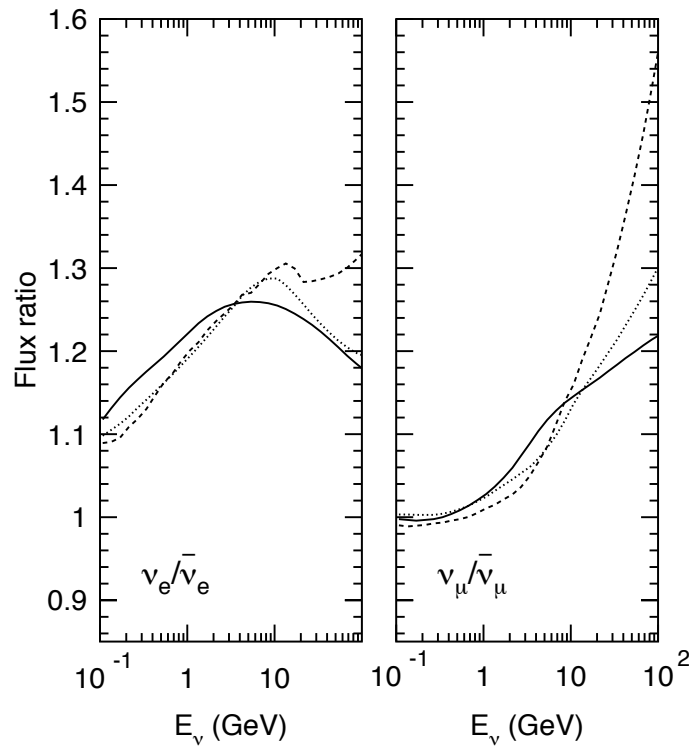


Figure 2.5: The flux ratios of ν_μ to $\bar{\nu}_\mu$ and ν_e to $\bar{\nu}_e$ versus neutrino energy. The solid line is from [3], the dashed line is from [4] and dotted line is from [5].

2.4 Neutrino pathlength

The pathlength of a neutrino is the function of the production height and the zenith angle. The typical production height for neutrinos is around 15 km [1]. We use a Monte Carlo method to simulate a distribution of the neutrino production heights. Figure 2.6 shows the pathlength distributions in air of different neutrino energies and neutrino flavors for both vertical and horizontal cases. Including the production height, Fig. 2.4 shows the averaged pathlength for 1 GeV ν_μ as a function of zenith angle. It is not hard to imagine that the uncertainty on pathlength for neutrinos passing a great distance crossing the Earth is relatively small and for horizontal and downward going neutrinos, is relatively larger since the baselines are shorter.

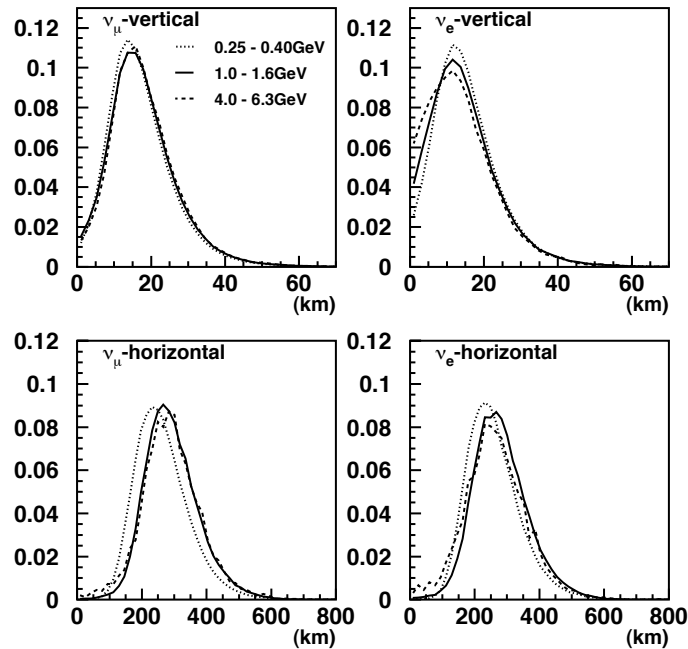


Figure 2.6: Distributions of neutrino pathlength in air

Cosmic rays are isotropic at the vicinity of the Earth. Therefore, geometrically, the neutrino flux should be up-down symmetric. However, due to the geomagnetic effect, low energy neutrinos are up-down asymmetric.

Figure 2.8 shows the zenith angle dependence of the atmospheric neutrino fluxes for several neutrino energies. Solid, dashed and dotted lines show the predictions in Ref. [3], Ref. [4] and Ref. [5], respectively (same key as Fig. 2.4). At low energies, and at the Kamioka location, the fluxes of downward-going neutrinos are lower than those of upward-going neutrinos. This is due to the deflection of primary cosmic rays by the geomagnetic field, roughly characterized by a minimum rigidity cutoff. For neutrino energies higher than a few GeV, the calculated fluxes are essentially up-down symmetric, because the primary particles are more energetic than the rigidity cutoff.

For upward going muons, which are produced by neutrinos interacting with rock beneath the Super-K detector, the typical energies are relatively higher and the decay K contribution becomes larger. We assume that the K/π production ratio uncertainty is 20% in the whole energy region [57, 58]. The uncertainties in the zenith angle and energy distributions due to the K/π production uncertainty are included in the systematic errors in the

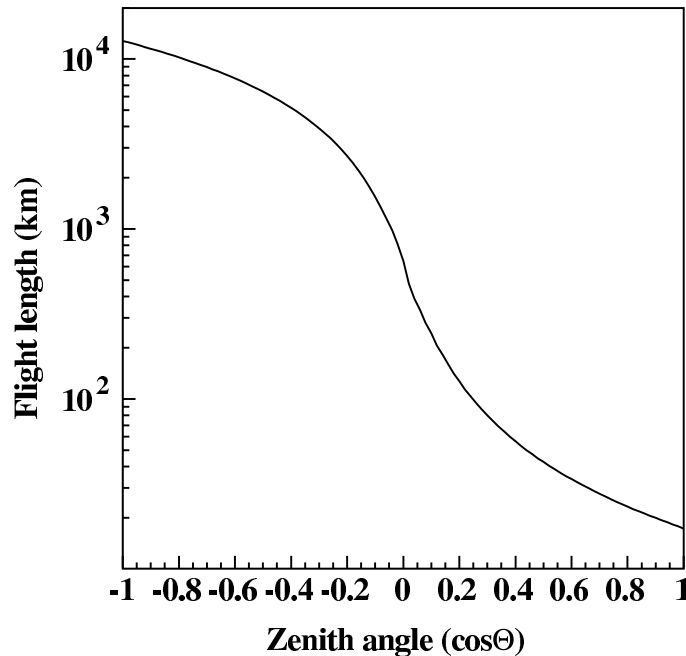


Figure 2.7: The averaged pathlength versus cosine of zenith angle

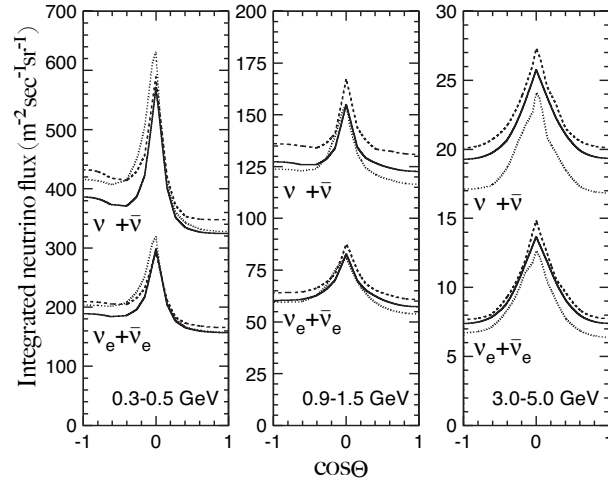


Figure 2.8: The flux of atmospheric neutrinos versus zenith angle. The solid line is from [3], the dashed line is from [4] and dotted line is from [5].

analysis. Figure 2.9 shows the zenith angle dependence of the atmospheric neutrino fluxes for higher energy region observed as upward muons in Super-Kamiokande. Again, solid, dashed and dotted lines show the prediction in Ref. [3], Ref. [4] and Ref. [5], respectively (same key as Fig. 2.4).

2.5 Summary

In summary, the uncertainty on the absolute flux is very large, but we do have pretty accurate knowledge on the flavor ratio and up-down flux ratio, which will provide the most important information on neutrino oscillation analysis. Table 2.1 has all the systematic uncertainties which show our understanding on atmospheric neutrino flux at Super-Kamiokande.

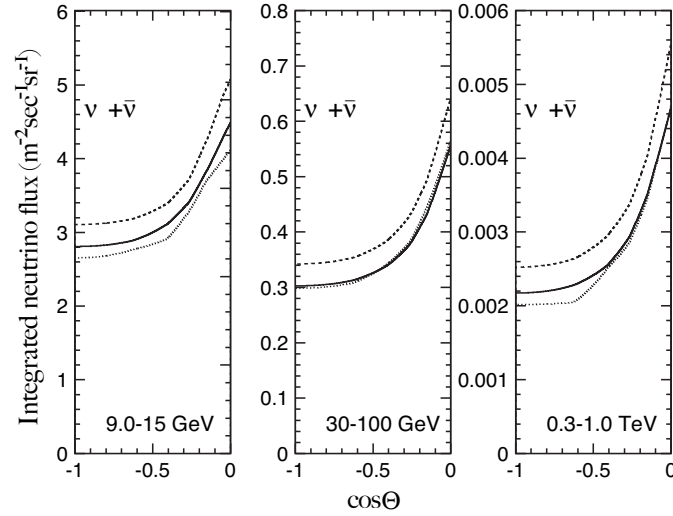


Figure 2.9: The flux of upward-going atmospheric neutrinos versus zenith angle. The solid line is from [3], the dashed line is from [4] and dotted line is from [5].

Table 2.1: Systematic uncertainties on the atmospheric neutrino flux

Systematic Uncertainty	$\sigma(\%)$	Index
Absolute Normalization	free	1
$(\nu_\mu + \bar{\nu}_\mu)/(\nu_e + \bar{\nu}_e)$ ($E_\nu < 5\text{GeV}$)	3.0	2
$(\nu_\mu + \bar{\nu}_\mu)/(\nu_e + \bar{\nu}_e)$ ($E_\nu > 5\text{GeV}$)	3.0	3
$\nu_e/\bar{\nu}_e$ ($E_\nu < 10\text{GeV}$)	5.0	4
$\nu_e/\bar{\nu}_e$ ($E_\nu > 10\text{GeV}$)	5.0	5
$\nu_\mu/\bar{\nu}_\mu$ ($E_\nu < 10\text{GeV}$)	5.0	6
$\nu_\mu/\bar{\nu}_\mu$ ($E_\nu > 10\text{GeV}$)	5.0	7
Up/down ratio	1.0	8
Horizontal/vertical	1.0	9
K/π ratio	20.0	10
Production height	10.0	11
Spectral index of primary cosmic ray above 100GeV	3.0	12
Sample-by-sample spectral index (FC Multi-GeV)	5.0	13
Sample-by-sample spectral index (PC and Up μ)	5.0	14
Solar activity	50.0	48

Chapter 3

Super-Kamiokande Experiment

The Super-Kamiokande detector is a 50 kiloton water Cherenkov detector located at the Kamioka Observatory of the Institute for Cosmic Ray Research, University of Tokyo. This facility is in the Mozumi mine in Gifu prefecture, Japan, under the peak of Mt. Ikenoyama which provides a 1,000 meters rock overburden (2,700 meters water equivalent). It is a multi-purposed underground experiment.

As the successor of the Kamiokande and IMB experiments [59, 60], the main physics goals of Super-Kamiokande are to study nucleon decay [61], solar [62] and atmospheric neutrinos [63]. Its low threshold, low-background environment, large target mass and large aperture make the detector a promising facility for many other research topics, for example but not limited to: supernova neutrinos, exotic properties of neutrinos [64], exotic particle searches [65], astrophysical [66, 67, 68, 69] and cosmological [70, 71] studies; it served as the far detector of K2K experiment [72]; it will also served as the far detector of fore-coming T2K experiment [73].

The Super-K experiment has three running periods so far. Super-K I (SK-I) started operation from April 1996 and continued until July 2001. In July 2001, the first upgrade was started to refurbish the failed photomultipliers (PMT) and cables and to partially replace

the outer detector (OD) reflector. The upgrade finished in October 2001 but in November 2001, a broken PMT at the bottom of the inner detector (ID) triggered a chain reaction and destroyed 70% of the PMTs in the detector. More information about the accident can be found in [74]. The second upgrade started in March 2002 and finished in December 2002, the rebuilt Super-K detector, Super-K II (SK-II), has a fully recovered OD but ID only has half of the PMTs that SK-I has. SK-II ran from January 2003 to October 2005 and has a livetime of 804 days for atmospheric neutrino observation. The fully recovered Super-K III (SK-III) started operation in July 2006.

This chapter will be mainly focused on factors relevant to the atmospheric neutrino sector. More details on all the technical respects of the detector can be found in Ref. [75, 62, 63].

3.1 Detector setup

Shown in Fig. 3.1, the Super-K detector consists of two concentric, optically separated water Cherenkov detectors contained in a stainless steel tank 42 meters high and 39.3 meters in diameter, holding 50 kilotons of pure water. The top of the detector, under the hemisphere, consists of electronics huts and open work area. Super-K water is supplied from the spring water inside the mine. The water in the tank is continuously circulated through the water purification system to filter out any microparticle contaminations to keep the transparency and, more importantly, radioactive materials from air, mainly radon (Rn). The water temperature in SK tank is controlled at ~ 12 °C.

The ID holds a cylindrical volume of pure water 16.9 m in radius and 36.2 m high. During SK-I running period, the inner detector (ID) has 11,146 Hamamatsu R3600 50 cm diameter photomultiplier tubes (PMTs) mounted on the inner wall, comprising a photocathode coverage of about 40%. The number of ID PMTs during SK-II period is reduced

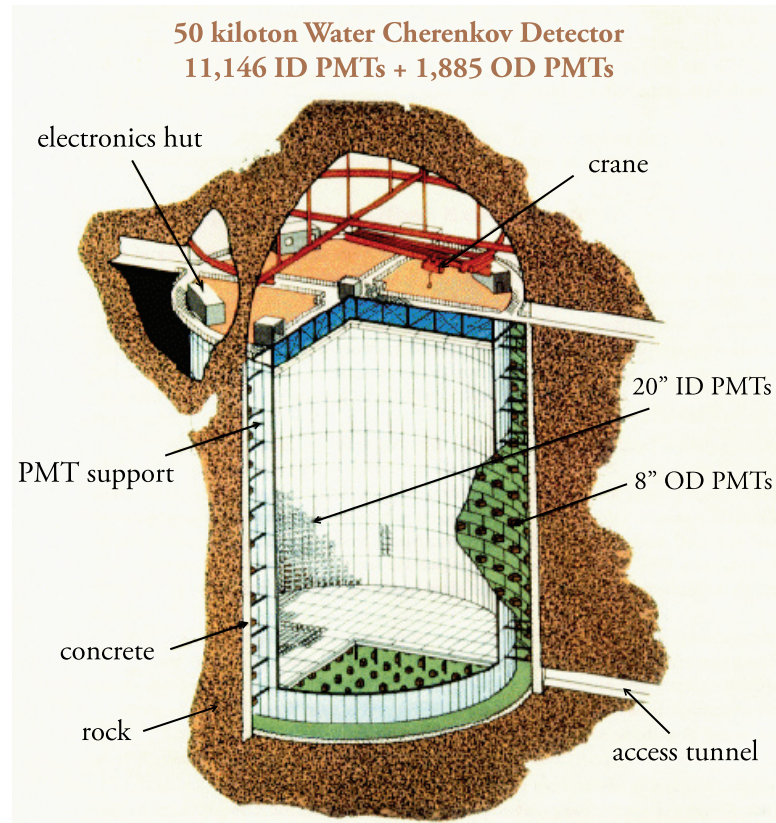


Figure 3.1: A schematic drawing of the Super-K detector (the number of ID PMTs during SK-II period was reduced by half)

by half due to the lack of supply. The photocathode coverage thus becomes around 20%. The 50 cm PMTs were specially designed [76] to have good single photoelectron (p.e.) response, with a root-mean-squared timing resolution of 2.5 nsec. The space between PMTs is covered by black plastics to prevent reflection.

The ID is surrounded by the outer detector (OD), a cylindrical shell of water 2.6-2.75 m thick including a dead space 55 cm. The OD is optically isolated from the ID and mainly functions as a 4π active veto — to identify the incoming and outgoing muons. The OD is instrumented with 1,885 outward-facing Hamamatsu R1408 20 cm PMTs. A $50\text{cm} \times 50\text{cm} \times 1.3\text{cm}$ wavelength shifter [77] is attached to every OD PMT to increase light collection efficiency. The interior of OD is covered with reflective Tyvek to further

increase light collection. We will discuss OD PMTs performance and the OD Monte Carlo in Appendix A. Besides functioning as the veto, the OD is also a thick passive radioactivity shield.

Each PMT is connected to high voltage (HV) supplies and signal processing electronics via coaxial cables. For the ID, signal and HV cables are separated, while the OD uses a single cable. The high voltages on the PMTs are set to make sure they have approximately equal gains within the ID and OD respectively in order to reduce the overall systematic uncertainty. These cables are all brought up to the open work area on the top of the tank, where they are distributed into four electronic huts. Every hut contains electronic racks and front-end data acquisition computers serving ID and OD PMTs for one quadrant of the detector. There are four cable holes on top of the detector to let the four cable bundles pass into the four electronic huts. Due to the big volumes occupied by the cable bundles in the OD, the cosmic ray muons passing through those “dead” volumes can not be detected by the OD so four plastic scintillators are installed on top of them outside the OD to veto these cosmic ray muons.

3.2 Electronics and data acquisition

Both ID and OD PMT signals are processed by asynchronous, self-triggering circuits that record the time and charge of each PMT hit over a threshold. Each ID PMT signal is digitized with custom Analog Timing Modules (ATMs) [78, 79] which provide $1.2 \mu\text{sec}$ timing range at 0.3 nsec resolution and 550 pC charge range at 0.2 pC resolution ($\sim 0.1 \text{ p.e.}$). The ATM has automatically-switched dual channels to provide deadtime-free data acquisition. The outer PMT signals are processed with custom charge-to-time conversion modules and digitized with LeCroy 1877 multi-hit TDCs over a $-10 \mu\text{sec}$ to $+6 \mu\text{sec}$ window centered on the trigger time. More details about the DAQ system of Super-K detector can be found

in [75, 63].

An event used in the atmospheric neutrino analysis is triggered by the coincidence of at least 30 PMT hits in a 200 nsec window which is the time for photons crossing the detector diagonally. The hit threshold for each individual PMT is about 1/4 p.e. This trigger condition corresponds to the mean number of hit PMTs for a 5.7 MeV electron. The trigger rate is 10-12 Hz so the total number of events in the raw data is of order $\sim 10^6$ per day. The trigger rate due to cosmic ray muons is 2.2 Hz. Digitized data are saved at a total rate of 12 GB per day.

3.3 Detector calibration

3.3.1 Water properties

The optical attenuation length L_{atten} of water is parameterized in the following way,

$$I = I_0 e^{-l/L_{\text{atten}}} / l^2,$$

where I is the light intensity after traveling a distance of l in water; I_0 is the initial intensity. At Super-K, L_{atten} is measured through both direct and indirect ways. The direct measurement uses a system consisting of a titanium-sapphire laser, a diffuser ball and a CCD camera. To measure the attenuation length, the diffuser ball which is pumped with laser is lowered into different positions in the SK tank and the light intensity on the surface is monitored by the CCD camera. A two inch PMT is used to monitor the stability of the laser and also to measure the initial light intensity. Since water quality is expected to change with time, this kind of measurements is made at regular intervals. The indirect measurements use through-going cosmic ray muons. Through-going muons lose almost

same amount energy per unit distance in SK tank, $\sim 2\text{MeV}/\text{cm}$, which makes them “standard” light sources for calibration purposes. Through-going muons also have advantages being continuous and plentiful so they can be used to monitor the attenuation length as a function of time.

L_{atten} is actually the combined effects of absorption and scattering on the intensity of light: $L_{\text{atten}} = \alpha_{\text{abs}} + \alpha_{\text{scat}}$. To measure them separately, a combination of dye and N^2 lasers of wavelengths 337, 371, 400 and 420 nm are used as light sources. The laser beam is brought into the SK tank through optical fibers pointing at the bottom of the tank. Each laser fires every 6 seconds during normal data taking. From the spatial and the timing distributions of the photons detected by PMTs, both absorption and scattering coefficients are studied with the help of Monte Carlo and incorporated into the detector simulation. Every 5 days, accumulated data are combined and analyzed as a single set.

3.3.2 The absolute energy calibration

Super-K employs several different sources to calibrate the absolute energy scale. For low energy from ~ 5 MeV to ~ 15 MeV, an electron linear accelerator (LINAC) [80] and a deuterium-tritium neutron generator (DTG) [81] are used and a small uncertainty (better than 1%) in hit counting is achieved [75]; for high energy, which is more relevant to atmospheric neutrino data, the following sources are used: the total number of photo-electrons as a function of muon track length, where the muon track length is estimated by the reconstructed muon entrance point and the reconstructed vertex point of an electron from the muon-decay; the total number of photo-electrons as a function of Cherenkov angle for low energy cosmic ray muons; the spectrum of muon-decay electrons; and the invariant mass of π^0 s produced by neutrino interactions, see Fig. 3.2. Figure 3.3 summarizes the absolute energy scale calibration by these studies.

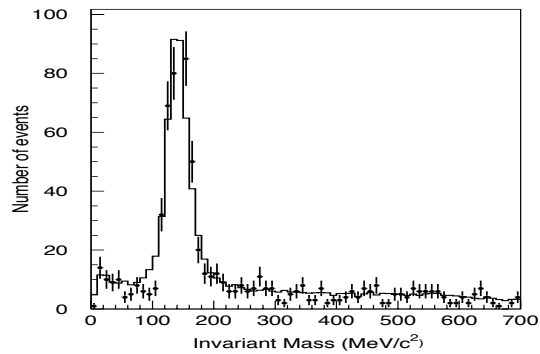


Figure 3.2: The reconstructed $\pi^0 \rightarrow \gamma\gamma$ invariant mass

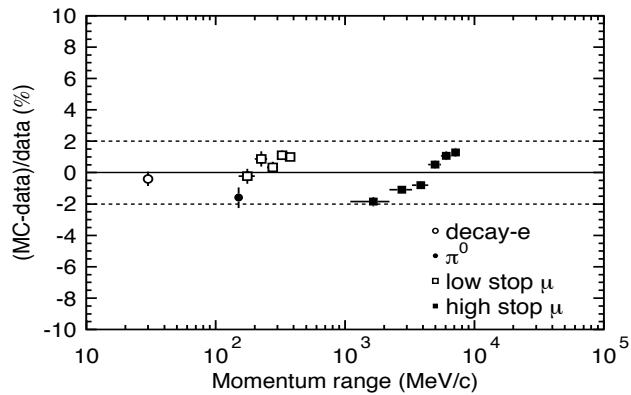


Figure 3.3: The determination of the absolute energy scale of Super-Kamiokande based on various techniques

The stability of the energy scale was also monitored continuously using stopping muons and muon-decay electrons. Figure 3.4 shows the time variation of the mean reconstructed energy of stopping muons divided by muon range and the mean reconstructed electron energy from muon-decays. Vertical axes in both figures are normalized to mean values and each data point corresponds to two month period. The root-mean-square of the energy scale variation is $\pm 0.9\%$ over the time of the experiment. From combining the absolute energy scale accuracy study ($\pm 1.8\%$) and the energy scale time variation ($\pm 0.9\%$), the total uncertainty of the energy scale of atmospheric neutrino detection was estimated to be $\pm 2.0\%$.

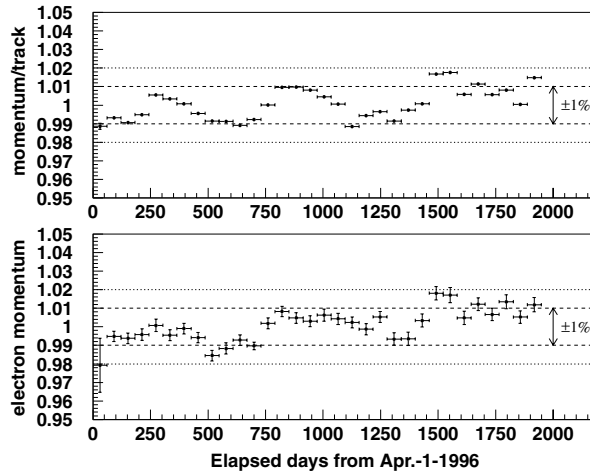


Figure 3.4: The mean reconstructed energy of cosmic ray stopping muons divided by their range (upper) and muon-decay electron (lower) as a function of elapsed days during SK-I.

3.4 Neutrino interaction simulation

Atmospheric neutrino oscillation analysis relies heavily on the comparison of the experimental data with the theoretical expectation. Thus, we need detailed simulations of both neutrino interactions and the Super-K detector. For atmospheric neutrino interactions, we need to simulate the interactions of neutrinos ranging from 10 MeV to 100 TeV with the water nuclei. In the case of upward muons, we need to simulation the interactions with the rock nuclei surrounding the detector. At Super-K, we have two neutrino interaction simulation programs: NEUT [82] and NUANCE [83]. We will only describe NEUT briefly. NEUT considers the following charged and neutral current neutrino interactions are considered:

1. (quasi-)elastic scattering, $\nu N \rightarrow lN'$,
2. single meson production, $\nu N \rightarrow lN'm$,
3. coherent π production, $\nu^{16}\text{O} \rightarrow l\pi^{16}\text{O}$,
4. deep inelastic scattering, $\nu N \rightarrow lN'hadrons$.

Here, N and N' are the nucleons (proton or neutron), l is the lepton, and m is the meson, respectively. For single meson production, K and η production are simulated as well as the dominant π production processes. If the neutrino interaction occurred in the oxygen nuclei, generated particles like pions and kaons interact with the nucleus before escaping.

3.4.1 Elastic and quasi-elastic scattering

The formalization of quasi-elastic scattering off a free proton was described by Llewellyn-Smith [84]. For scattering off nucleons in ^{16}O , the Fermi motion of the nucleons and Pauli Exclusion Principle were taken into account. The nucleons are treated as quasi-free particles using the relativistic Fermi gas model of Smith and Moniz [85]. The momentum distribution of the nucleons were assumed to be flat up to the fixed Fermi surface momentum of $225 \text{ MeV}/c$. This Fermi momentum distribution was also used for other nuclear interactions. The nuclear potential was set to $27 \text{ MeV}/c$.

3.4.2 Single meson production

Rein and Sehgal's model was used to simulate the resonance productions of single π , K and η [86, 87]. In this method, the interaction is separated into two parts:

$$\begin{aligned}\nu + N &\rightarrow l + N^*, \\ N^* &\rightarrow m + N',\end{aligned}$$

where m is a meson, N and N' are nucleons, and N^* is a baryon resonance. The hadronic invariant mass, W , the mass of the intermediate baryon resonance, is restricted to be less than $2 \text{ GeV}/c^2$. In addition to the dominant single π production, K and η production is considered.

To determine the angular distribution of pions in the final state, we also use Rein and Sehgal's method for the $P_{33}(1232)$ resonance. For the other resonances, the directional distribution of the generated pions is set to be isotropic in the resonance rest frame. The angular distribution of π^+ has been measured for $\nu p \rightarrow \mu^- p \pi^+$ [88] and the results agree well with the Monte Carlo prediction. We also consider the Pauli blocking effect in the decay of the baryon resonance by requiring that the momentum of nucleon should be larger than the Fermi surface momentum. Pion-less delta decay is also considered, where 20% of the events do not have the pion and only the lepton and nucleon are generated [89].

The quasi-elastic and single meson production models have a parameter (axial vector mass, M_A) that must be determined by experiments. For larger M_A values, interactions with higher Q^2 values (and therefore larger scattering angles) are enhanced for these channels. The M_A value was tuned using the K2K [6] near detector data. In our atmospheric neutrino Monte Carlo simulation, M_A is set to 1.1 GeV for both the quasi-elastic and single-meson production channels, but the uncertainty of the value is estimated to be 10%. Figure 3.5 shows the K2K 1-kton water Cherenkov detector data on the scattering angle for single Cherenkov ring events [6] together with the prediction by the Monte Carlo used in this analysis. The scattering angle agrees well between the data and Monte Carlo overall.

Coherent single-pion production, the interaction between the neutrino and the entire oxygen nucleus, is simulated using the formalism developed by Rein and Sehgal [90].

3.4.3 Deep inelastic scattering

In order to calculate the cross-sections of deep inelastic scattering, the GRV94 [91] parton distribution function is used. In the calculation, the hadronic invariant mass, W , is required to be greater than $1.3 \text{ GeV}/c^2$. However, the multiplicity of pions is restricted to be greater than or equal to 2 for $1.3 < W < 2.0 \text{ GeV}/c^2$, because single pion production is sepa-

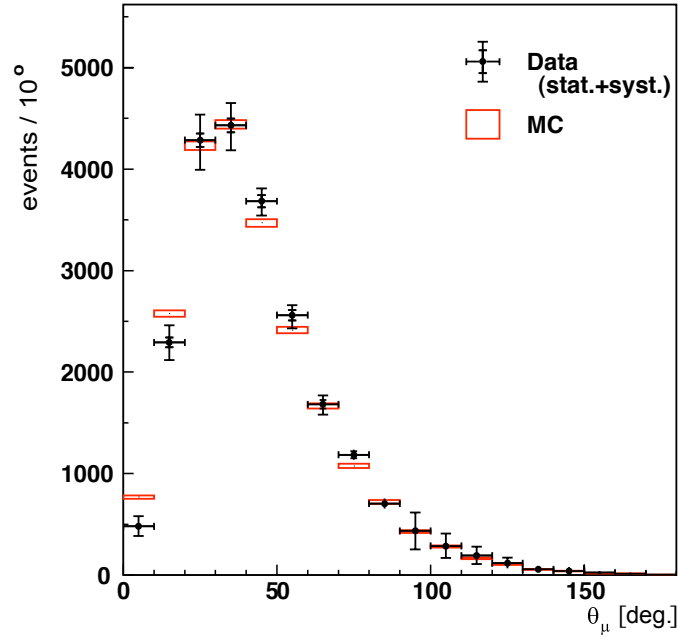


Figure 3.5: The scattering angle distribution by neutrino interactions off the H_2O target from the K2K experiment (data are from Fig.1(b) of Ref. [6]).

rately simulated as previously described. In order to generate events with multi-hadron final states, two models are used. For W between 1.3 and 2.0 GeV/c^2 , a custom-made program [92] is used to generate the final state hadrons; only pions are considered in this case. For W larger than 2 GeV/c^2 , PYTHIA/JETSET [93] is used.

Total charged current cross sections including quasi-elastic scattering, single meson productions and deep inelastic scattering are shown in Fig. 3.6. The solid line shows the calculated total cross section. The dashed, dot and dash-dotted lines show the calculated quasi-elastic, single-meson and deep-inelastic scatterings, respectively. Data points are taken from different experiments [63].

3.4.4 Nuclear effects

The interactions of mesons within the ^{16}O nucleus are also important for the atmospheric neutrino analysis. Basically, all of the interactions are treated by using a cascade model.

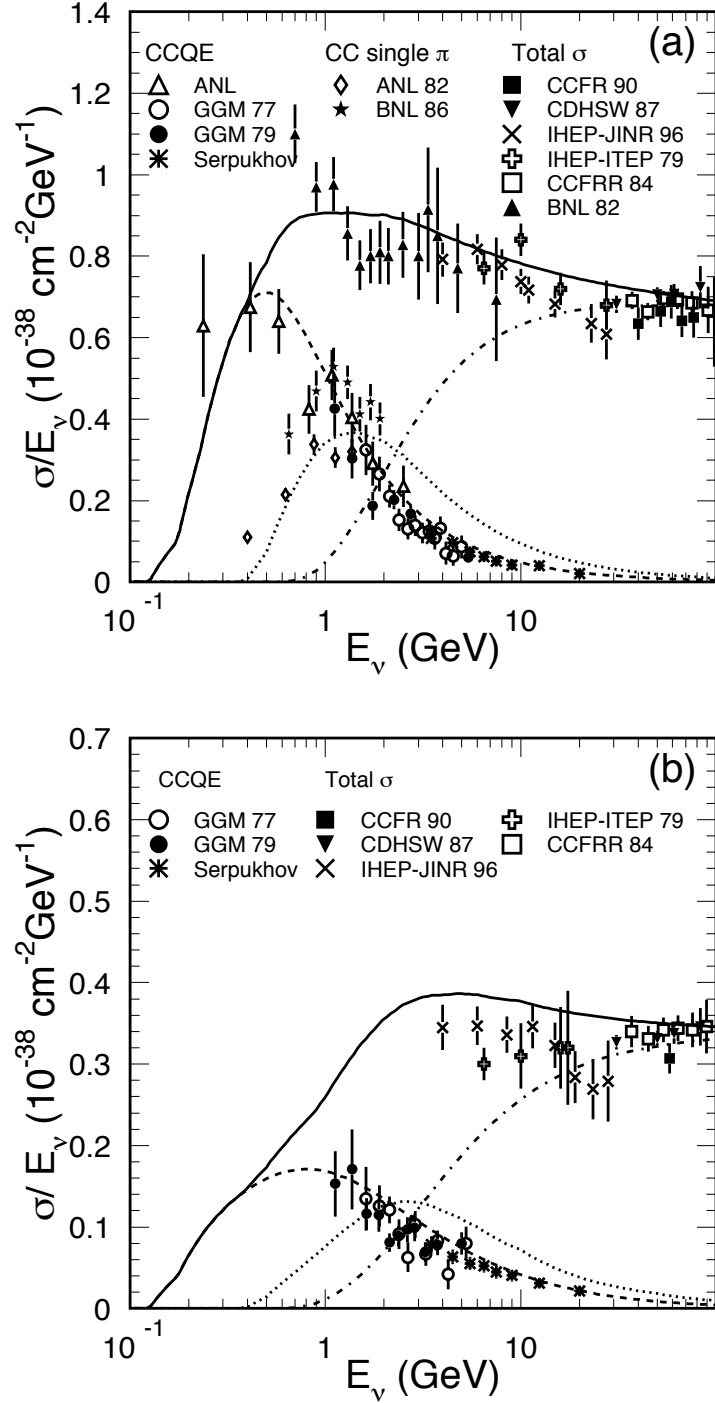


Figure 3.6: Charged current total cross section divided by E_ν for (a) neutrino and (b) anti-neutrino nucleon charged current interactions.

The interactions of pions are very important because the cross section for pion production is quite large for neutrino energies above 1 GeV and the interaction cross sections for pions in nuclear matter is also large.

In our simulation program, we consider the following pion interactions in ^{16}O : inelastic scattering, charge exchange and absorption. The initial position of the pion generated according to the Woods-Saxon nucleon density distribution [94]. The interaction mode is determined from the calculated mean free path of each interaction. To calculate the mean free path, we adopt the model described by Salcedo *et al.* [95]. The calculated mean free path depends not only on the momentum of the pion but also on the position of the pion in the nucleus. If inelastic scattering or charge exchange occurs, the direction and momentum of the pion are determined by using the results of a phase shift analysis obtained from $\pi-N$ scattering experiments [96]. When calculating the pion scattering amplitude, the Pauli blocking effect is taken into account by requiring the nucleon momentum after interaction to be larger than the Fermi surface momentum at the interaction point. The pion interaction simulation was checked using data for the following three interactions: $\pi^{12}\text{C}$ scattering, $\pi^{16}\text{O}$ scattering and pion photo-production ($\gamma + ^{12}\text{C} \rightarrow \pi^- + X$) [97].

3.5 The detector simulation

A Monte Carlo simulation on how the detector reacts to physical processes is needed to understand the systematics of the detector, to do data reduction and to compare our observation with the predictions of different theories or models.

The detector's responses to the final state particles are simulated with a Monte Carlo program based on the GEANT3 package [98], in which the propagation of particles, the generation and propagation of Cherenkov photons, and the response of the PMTs are considered. The CALOR package [99] was employed to simulate hadronic interactions in

Table 3.1: Super-K detector related systematic uncertainties

Systematic uncertainty	Value (SK-I)	Value (SK-II)	Index
Energy calibration	0.02	0.025	37
Up/down symmetry of energy calibration	0.006	0.006	39

water. This package can reproduce the pion interactions results very well down to low momentum regions of $\sim 1\text{GeV}/c$. For still lower momenta ($p_\pi \leq 500\text{MeV}/c$), a custom subroutine was made based on experimental data in Ref. [100] on $\pi - {}^{16}\text{O}$ scattering and in Ref. [101] on $\pi - p$ scattering.

For the propagation of Cherenkov photons in water, Rayleigh scattering, Mie scattering and absorption were considered in our simulation code. The attenuation coefficients in water were tuned to reproduce the measurements of the laser system described in Section 3.3.1. Light reflection and absorption on detector material, such as the surface of PMTs and black plastic sheets between the PMTs are simulated based on direct measurements, using probability functions that depend on the photon incident angle.

To give an example how we tune the detector simulation program, an OD simulation tuning process was presented in Appendix A.

3.6 Summary

Our understanding to the Super-K detector can be summarized into systematic uncertainties. SK-I and SK-II are practically different detectors with similar design so they have the same systematic uncertainties terms but with different values. Table 3.1 shows the values of SK-I and SK-II.

The uncertainties on neutrino reactions are summarized in Table 3.2. They are naturally the same for SK-I and SK-II.

Table 3.2: Neutrino interaction related systematic uncertainties

Systematic uncertainty	Value	Index
M_A in quasielastic and single- π	0.10	15
Quasielastic scattering model dependence	0.10	16
Quasielastic scattering cross section	0.10	17
Single-meson production cross section	0.10	18
DIS model dependence	0.10	19
DIS total cross section	0.05	20
Coherent pion cross section	0.30	21
NC/CC ratio	0.20	22
Nuclear effect in ^{16}O	0.30	23
Pion energy spectrum	0.10	24
CC ν_τ cross section	0.30	25
Hadron simulation	0.10	30

Chapter 4

Super-Kamiokande Atmospheric Data

Raw Super-K data consist mainly of downward-going cosmic ray muons and low energy radioactivity events. The the ID and OD double structure can remove cosmic ray muons easily with high efficiency. The atmospheric neutrino energy range, $E_{vis} > 30\text{MeV}$, essentially makes the analysis free of any low energy background. Visible energy is defined as the energy of an electromagnetic shower that gives a certain amount of Cherenkov light. For example, a muon of momentum $300\text{ MeV}/c$ yields a visible energy of about 110 MeV . After background rejection, Super-K observes ~ 20 atmospheric neutrino events per day. In this chapter, we will briefly review data reduction and event reconstruction processes.

4.1 Data reduction

Based on the topology of the SK detector, neutrino events are divided into three categories: fully-contained (FC) events, partially-contained (PC) events and upward-going muons ($\text{Up}\mu$). Both FC and PC events are neutrino events which interact inside the ID. FC events are the ones whose final state particles are completely contained inside the ID while PC means there are some final state particles entering the OD, typically the muon from a

CC ν_μ interaction.

FC and PC events share the same set of good run selection criteria so they have identical livetime. SK-I has a livetime of 1489.2 days and SK-II 803.919 days. Up_μ event's parent neutrinos interact within 5 km underneath the SK detector in the Earth and the final state particle, nearly 100% muons, enter the SK detector. Up_μ events mainly rely on fitting the long muon tracks in ID so they are less susceptible to detector effects thus have looser data quality cuts so longer livetimes are obtained. During the SK-I period, the Up_μ sample accumulated a livetime of 1645.91 days and for SK-II, 827.744 days. For both SK-I and SK-II running periods, same data reduction schemes and algorithms are used but the cut values are modified accordingly since SK-I and SK-II are, in principle, two different but very "similar" detectors. Three different data reduction paths are used to separate FC, PC and Up_μ events.

Starting from raw data, to separate FC and PC events, a fast spatial clustering algorithm is applied to the OD hits: if the number of hits in the largest OD cluster is less than 10, the event is defined as FC; otherwise, it is defined as PC. Figure 4.1 shows the comparison between MC and observation. Since the OD is essentially the same configuration, this cut value is same for SK-I and SK-II.

4.1.1 Reduction of fully-contained events

The major background events in FC sample come from cosmic ray muons, low energy events from radioisotopes and electronic noise. The FC event reduction process has five steps.

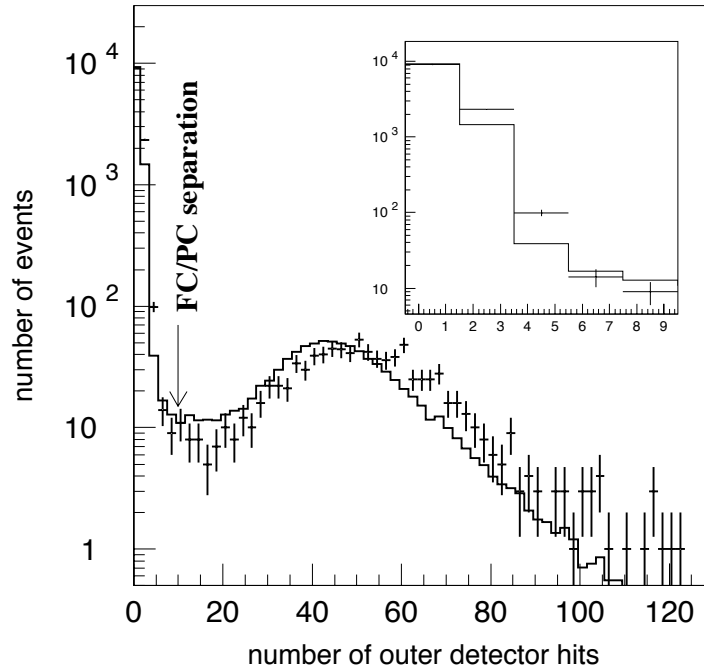


Figure 4.1: The number of hits in the largest outer detector cluster. Solid histogram is the MC prediction with neutrino oscillation considered.

FC first reduction

The first step of FC reduction uses simple and efficient criteria to reduce the amount of data to a manageable size. It has 3 cuts:

- $pe_{300} > 200$ p.e.: pe_{300} is the total charge collected in ID within a 300 nsec time window. By requiring more than 200 p.e.'s, low energy background events are rejected. This cut is reduced to $pe_{300} > 100$ p.e. for SK-II due to the fact that the ID PMTs are reduced by 50%.
- $n_{ODhit800} < 50$: $n_{ODhit800}$ is the total hits in OD within a 800 nsec time window. This cut removes big amount of cosmic muons.
- $t_{diff} > 100 \mu\text{sec}$: t_{diff} is the time interval between the current event and the previous

one. By requiring the time interval, decay electrons entering ID from cosmic muons are removed.

Those cuts reduce event rate from $\sim 10^6$ events/day down to ~ 3000 events/day.

FC second reduction

The second step of FC is to further remove cosmic muon events and low energy backgrounds. It has 2 cuts:

- $n_{ODhit800} \leq 25$ if $pe_{tot} < 100,000$ p.e.: pe_{tot} is the total number of p.e.'s in ID. This cut is similar to the second cut of step 1 but tighter to remove the relatively low energy cosmic muons.
- $pe_{max}/pe_{300} < 0.5$: pe_{max} is the maximum number of p.e.'s recorded by any single ID PMT. By requiring this ratio, low energy background events and flasher events with one single big hit are removed. A PMT sometimes flashes due to a discharge around the dynode structure. The noise event cause by such a problematic PMT is call a flasher event. Under this circumstance, one tube tends to record most of the photons so this cut can remove some flasher events. More elaborate cuts will be applied to remove the remaining flasher events in later steps.

After this reduction step, the event rate goes down to ~ 200 events/day.

FC third reduction

After background events are significantly reduced in step 1 and 2, more complex criteria (thus more computation time is needed) can be applied to further reject cosmic ray muons, flasher events and low energy events which escaped previous simple cuts. At this stage,

the goal is to remove several specific kinds of background events and event reconstruction tools are used to help the reduction.

- Remove through-going muon events which do not produce enough hits in OD. To identify these through-going muons, following criteria are required:

- $pe_{max} > 250$ p.e.

- $mugood > 0.75$: $mugood$ is the goodness being a through-going muon and is defined as follow:

$$mugood = \frac{\sum_i \exp\left(-\frac{(t_i - T_i)^2}{2(1.5\sigma_i)^2}\right) / \sigma_i^2}{\sum_i 1/\sigma_i^2}, \quad (4.1)$$

where t_i and σ_i are the hit time of the i -th PMT and its uncertainty, T_i is the expected hit time based on the time when the muon enters ID and its reconstructed track.

- $n_{ODhit,in} \geq 10$ or $n_{ODhit,out} \geq 10$: $n_{ODhit,in}(n_{ODhit,out})$ is the number of hit PMTs in OD within 8m around the entrance(exit) point in a 800 nsec time window. The entrance point is defined as the position of the earliest hit ID PMT with neighbor hits; the exit point is defined as the center of the saturated ID PMTs.

- Remove stopping muon events which escape cuts in steps 1 and 2. The following criteria are used to identify stopping muons:

- If $mugood > 0.5$, then $n_{ODhit,in} \geq 5$ or $n_{ODhit,in} \geq 10$: $mugood$ of stopping muons is also defined as Eq. 4.1. The entrance point of a stopping muon is reconstructed in the same way for the through-going muon described above.

- Remove cosmic ray muons entering from cable holes. As we described before in Sec. 3.1, cosmic ray muons passing through the cable bundles in OD can not be detected by OD and they will be mistaken as neutrino events. Topologically, the stopping ones will be considered as FC events. These events can be identified by the following cuts:
 - One veto counter (described in Sec. 3.1) hit.
 - $l_{veto} < 4\text{m}$: l_{veto} is the distance from the reconstructed vertex to the hit veto counter.
- Remove accidental events. Occasionally, a low energy event and the following cosmic ray muon happen in the same trigger gate. These events can not be rejected by the cuts in steps 1 and 2 because the absence of OD activities during the gate and the enough number of ID p.e.'s due to the muon. By combining the two following cuts, these accidental events can be removed:
 - $n_{ODhit,off500} > 20$: $n_{ODhit,off500}$ is the number of hit OD PMTs in the fixed time window between +400nsec and +900nsec after the trigger.
 - $pe_{off} > 5000\text{p.e.}$: pe_{off500} is the number p.e.'s in ID in a fixed time window from +400 nsec to +900 nsec after the trigger
- Remove flasher events. Most flasher events have wider time distribution compared to neutrino events. Flasher events can be identified by the following criteria:
 - $n_{min100} \geq 14$ or $n_{min100} \geq 10$ if $n_{IDhit} < 800$: n_{min100} is the minimum number of ID hits in a 100 nsec sliding time window; n_{IDhit} is the total number of ID hits.

- Remove low energy events. The main source of low energy events at this stage are electronic noise and decay of radioisotopes. They are distributive sources so these events can be identified by the following cut:
 - $n_{IDhit50} < 50$: $n_{IDhit50}$ is the number of ID hits within a 50 nsec sliding time window after subtracting the each hit time by the time of flight assuming all the photons come from the same vertex. The vertex is determined as the position at which the time residual distribution is peaked.

After those cuts, the number of events is around 45/day.

FC fourth reduction

The forth reduction is dedicated to the remaining flasher events. As described previously, flasher events are due to the discharges of PMT dynodes. Such “hot” PMT intend to discharge repeatedly before they are identified and shut off. Thus, the flasher events produced by such a tube have similar spatial hit patterns and can be identified by calculating the spatial correlations between events. The number of ID PMTs is of order 10^4 so the computation power needed is very high. In order to reduce the amount of computation, ID PMTs are divided into 1450 patches and each patch represents a spatial point in the calculation of the correlation coefficients. The correlation coefficient between events a and b is defined as,

$$r^{ab} = \frac{1}{N} \sum_{i=1}^N \frac{(Q_i^a - \langle Q^a \rangle)(Q_i^b - \langle Q^b \rangle)}{\sigma^a \sigma^b} ,$$

where N is the number of spatial points (number of patches in our case), $Q_i^a(Q_i^b)$ is the charge at each patch and $\sigma^a(\sigma^b)$ is its standard deviation of event $a(b)$, and $\langle Q^a \rangle(\langle Q^b \rangle)$ is the average charge of event $a(b)$.

If the distance between the PMTs with the highest number of p.e.'s of two events is small, which means the highest charge is produced around the same area, then they are more likely to be a pair of flasher events. Considering the fact of the radius of ID tube is around 50cm, an extra value of 0.15 is given to the correlation coefficient to account this extra information if the distance is less than 75cm. The threshold of tagging similarity is set at

$$r_{th}^{ab} = 0.168 \log_{10} \frac{pe_{tot}^a + pe_{tot}^b}{2} + 0.130 \quad ,$$

where $pe_{tot}^a(pe_{tot}^b)$ is the total number of p.e.'s in ID of event $a(b)$. Above this threshold, events are identified as similar events.

The calculation is made by pairing with the 10,000 events before and after the target one, and the number of matching up two similar events are counted. If the number of matches is beyond certain values which depend on the maximum correlation coefficient among the 20,000 pairs, the target event is identified as flasher.

After this reduction step, the event rate is 18 events/day.

FC fifth reduction

The last reduction step is to remove the remaining background events coming from different sources. This step is similar to the third reduction step but with more delicate reconstruction algorithms.

- Stopping muons. The cut to identify stopping muons is similar to the one in step 3, $n_{IDhit,in} \geq 5$, but the entrance point by extrapolating the fitted track of the event backward instead of using the position of the earliest hit PMT.

- Invisible muons. An invisible muon event is caused by the decay electron of a cosmic ray muon which is below Cherenkov threshold in ID due to the energy loss along the way entering ID. Such events have signals in OD before the triggers and can be identified by the following criteria:
 - $pe_{tot} < 1000$ p.e.: pe_{tot} is the total number of p.e.'s in ID
 - $n_{ODhit,early}^{max} > 4$: $n_{ODhit,early}^{max}$ is the maximum number hit PMTs in a 200 nsec sliding time window from -8,900 nsec to -100 nsec
 - $n_{ODhit,early}^{max} + n_{ODhit,500} > 9$ if $l_{clust} < 500$ cm or $n_{ODhit,early} > 9$ otherwise: $n_{ODhit,500}$ is the number of hit PMTs in OD in a fixed time window from -400 nsec to 100 nsec; l_{clust} is the distance between two OD clusters used during the calculation of $n_{ODhit,early}$ and $n_{ODhit,500}$ respectively.
- Accidental events. More detailed calculations are employed to remove the remaining accidental events:
 - $pe_{500} < 300$ p.e.: pe_{500} is the number of p.e.'s in a fixed time window between -100 nsec and 400 nsec
 - $n_{OD,late}^{max} > 20$: $n_{OD,late}^{max}$ is the maximum number of hit OD PMTs in a 200 nsec sliding time window from +400 nsec to 1,600 nsec
- Long tail flasher events. These events are identified by the following cut:
 - $n_{IDhit,100}^{min} > 5$ if the goodness of point fit < 0.4 : $n_{IDhit,100}^{min}$ is the minimum number of hit ID PMTs in a 100 nsec sliding window from +300 nsec to +800 nsec; point fit will be explained later in the event reconstruction section

After the fifth step, event rate is 16 events/day.

4.1.2 Reduction of partially-contained events

PC events require OD activities, which makes the reduction rather hard because it gives cosmic ray muons chances to get mixed in. PC reduction, like FC reduction, also has five steps which are arranged in the same strategic way — simple and efficient reduction cuts first then more delicate ones.

PC first reduction

Due to the high event rate, the strategy of the first PC reduction is to use fast and effective cuts to reject through-going cosmic ray muons and low energy backgrounds. PC events should meet the following criteria:

- $p_{e_{tot}} \geq 1000$ p.e. : $p_{e_{tot}}$ is the total number of p.e.'s observed in ID. This cut is to reject the low energy backgrounds. A signal strength of 1000 p.e.'s corresponds to a muon with momentum of 310 MeV/c, while a PC muon event should have traveled at least 2m thus its momentum is ~ 500 MeV/c, well beyond this cut.
- $T_{wid} < 260$ nsec: T_{wid} is the width of the hit timing distribution among OD PMTs. This cut is targeted at through-going cosmic ray muons — through-going muons enter OD twice thus have a wide T_{wid} distribution.
- $n_{ODcluster} < 2$: $n_{ODcluster}$ is the number of OD hit PMT clusters. A hit cluster is formed by grouping PMTs with more than 8 p.e.'s within 8m. This cut is also to reject through-going muons since they, in principle, leave two hit clusters in OD.

Obviously, the first step has no attempt to reject stopping cosmic ray muons. After the first step, the event rates goes down to 14,000 events/day.

PC second reduction

The second PC reduction is designed to further remove the remaining through-going cosmic ray muons. A different clustering algorithm is applied in this step to help identifying through-going muons. The OD (ID) walls are divided into 11×11 (21×21) patches and the total charge in each patch is counted. Clusters are formed by calculating the charge gradient. Following cuts are required for PC events:

- $n_{ODcluster2} < 2$: $n_{ODcluster2}$ is the number of clusters in OD using this new clustering algorithm and require a hit PMT must have at least 6 p.e.'s.
- $n_{ODhit}^{min} < 7$: n_{ODhit}^{min} is minimum number of PMTs in the hit clusters of the top, bottom, or barrel region. This cut is to remove corner clipping through-going muon events which leave hits in both top or bottom and barrel regions.
- $pe_{200cm} > 1000$ p.e.: pe_{200cm} is the number of p.e.'s in ID collected within 2m around the highest charged OD PMT in the OD cluster. This cut is to
- $n_{2nd-cluster}$: number of hits in the 2nd (ordered by number of hits in the cluster) OD cluster
- n_{min} : number of hits in the first cluster or the rest of OD hits depending on which one is smaller
- n_{outer} : number of hits in the most charged OD cluster

PC third reduction

This step is to remove flasher events and cosmic ray stopping muons. To remove flasher events which have wider time distribution compared to neutrino events, the same cut used in FC third step is used:

- $n_{min100} \geq 14$ or $n_{min100} \geq 10$ if $n_{IDhit} < 800$: n_{min100} is the minimum number of ID hits in a 100 nsec sliding time window; n_{IDhit} is the total number of ID hits.

To remove stopping muons, a simple fitter call “point fit” is used to determine the direction of the ring. Then through backward extrapolating, the “entrance point” of the track in OD is identified. For a true neutrino event, there should not be hit PMTs around this point except noise hits; while for a real cosmic ray muon, it is the true entrance point and we expect some OD hits in this region. So the stopping muons are identified by the following cut:

- $n_{ehit8m} > 10$: number of hits in OD within 8 meters of the back extrapolated entrance point on OD wall.

After this reduction step, the event rate is around 100 events/day.

PC fourth reduction

PC 4th reduction is targeted at the remaining cosmic ray muons. In this step, combined information of point fit and through-going muon fit is used. The vertex position and track direction are from point fit and mugood and mudistance are from through-going muon fitter. PC events must pass the following cuts:

- $\cos\theta_{fit-first} > -0.8$: $\theta_{fit-first}$ is the angle between the fitted direction and the line connecting the vertex and the first hit tube in the ID cluster. These two vectors should be back-to-back for cosmic ray muons.
- $mudistance > 30$ m if $mugood > 0.85$: mugood is the goodness value being a through-going muon which is defined in Eq. 4.1. Real cosmic ray muons have better goodness.

- $d_{corner} > 150$ cm : d_{corner} is the distance from the fit vertex to the nearest ID corner.

This cut is to remove corner clipping through-going muons.

The event rate after the fourth reduction drops to ~ 20 events/day.

PC fifth reduction

This last reduction step is to reject all the remaining background events. The cuts are designed specifically for each kind of distinctive background source.

- Remove low energy events. $pe_{tot} \geq 3000$: pe_{tot} is the total number of p.e.'s in ID.
- Remove through-going muons. There are several different cuts targeting at the different signatures of through-going muons and we will explain them one by one:
 - $d_{1st-2nd} > 20$ cm and $pe_{2nd} > 10$: $d_{1st-2nd}$ is the distance between the highest charged cluster and the 2nd highest charged cluster; pe_{2nd} is the number of p.e.'s in the second highest charged cluster. These clustering information is from the algorithm in PC second.
 - $n_{cluster5} > 1$: $n_{cluster5}$ is the number of clusters in OD using a modified version of the clustering algorithm in the 2nd PC reduction. Instead of using 11×11 patch dividing scheme for OD, a 6×6 one is used and the threshold of hit PMTs changed from 2.0 p.e.'s to 0.5 p.e.
 - $n_{ODhit,top} > 7$ and $pe_{OD,top} > 10$, $n_{ODhit,bottom} > 7$ and $pe_{OD,bottom} > 10$, and $0.75 \times \frac{40m}{c} < T_{diff} < 1.5 \times \frac{40m}{c}$: $n_{ODhit,top}$ ($n_{ODhit,bottom}$) is the number of hit on the top (bottom) of OD; $pe_{OD,top}$ ($pe_{OD,bottom}$) is the number of p.e.'s on the top (bottom) of OD; T_{diff} is the time difference between the average hit times of the top and the bottom hits. This cut is targeted at the through-going muons passing through the detector along the ID wall.

- $n_{ODhit,in} \geq 5$ and $n_{ODhit,out} \geq 5$ and $0.75 \times \frac{40m}{c} < T_{diff} < 1.5 \times \frac{40m}{c}$: this cut uses the information gained from a precise fitter, MS-fit, to remove the remaining through-going muons. $n_{ODhit,in}$ ($n_{ODhit,out}$) is the number of hits in OD within 8 m of entrance (exit) point using the precise fitter; T_{diff} is the average hit time difference between the entrance and the exit point hit PMTs.
- Remove stopping muons. There are three criteria in series to identify stopping muons with different features. A precise fitter, MS-fit, is used to provide the information removing stopping muons for the first two criteria. The third signature utilizes stopping muon fitter.
 - $n_{ODhit,in} \geq 10$: this is the number of hit PMTs in OD within 8 m of the entrance point.
 - $\theta_{TDC-fit} > 90^\circ$ or $\theta_{MS-fit} > 90^\circ$: $\theta_{TDC-fit}$ (θ_{MS-fit}) is the angle between the ring direction using TDC- (MS-) fitter and the direction of OD cluster.
 - $mugood > 0$ and $\frac{pe_{cone}}{pe_{tot}} \geq 0.6$ and $n_{ODhit,in} > 6$: $mugood$ is the goodness being a stopping muon; pe_{cone} is the number of p.e.'s inside the 42° cone and pe_{tot} is the total number of p.e.'s in ID.
- Remove cable hole events. Unlike FC events, the veto counters on top the cable bundles can not identify all the cosmic muons since there are PC events exiting the detector and hit the veto counters. Two signatures are used to identify cosmic ray muons for PC reduction:
 - one veto counter hit
 - $\vec{d}_{ring} \cdot \vec{d}_{vertex-veto} > -0.8$: \vec{d}_{ring} is the ring direction reconstructed by TDC-fitter and $\vec{d}_{vertex-veto}$ is the unit vector from the hit veto counter to the reconstructed vertex.

4.1.3 Reduction of upward-going muons

The goal of the upward-going muon (UP_{μ}) reduction is to save the muons produced through neutrino interactions in Earth. The main background are downward-going and horizontally-going cosmic ray muons. The reduction of UP_{μ} s consists of two steps, first, a automated reduction program is applied to reduce the background as much as possible; then, physicists will scan these events one by one using an event displayer to pick out the neutrino events. However careful, it is impossible to eliminate the cosmic ray muons around the horizontal direction. Thus, the cosmic ray muon contamination near the horizontal direction is estimated by extrapolating the cosmic ray muon zenith angle distributions above the horizon. Events with only high-E triggers are considered as candidates of UP_{μ} s.

Energy cut

We only use the events with pathlength greater than 7 meters in order to reduce the π^{\pm} background events produced by downward-going cosmic ray muons around the detector [74]. Thus, we can safely cut away the low energy events. On the other hand, it is difficult to reconstruct ultra high energy events which saturate the Super-K ID. So, the following cut on the ID charge is used,

- $8000 \leq pe_{tot} < 1,750,000$: pe_{tot} is the total number of p.e.'s in the ID

Background event rejection

Several different muon fitters specialized in different kind of UP_{μ} events are used to reconstruct the pathlengths and the directions of the muons. The zenith angle cuts have two stages:

1. In this stage, muon fitters stopmu1st and muboy are used and the following events are rejected:

- Corner clipper events: either of the following cut is met
 - muboy classifies the event as corner-clipper AND goodness value is greater than 0.35
 - muboy classifies the event as stopping or through-going AND the muon pathlength is less than 4 meters AND goodness value is greater than 0.35 AND downward
- Double muon events: both muboy and stopmu1st classify the event as multiple muon
- Downward-going cosmic ray muons: muboy classifies the event as downward-going and goodness-of-fit is greater than 0.45

The following events are classified as good $UP_{\mu S}$ and saved for the final eye scan:

- Muboy output direction is upward and $f_{cone} > 0.8$

According to the output information of muboy, the remaining events are separated into through-going muons, which will be passed onto thrumu1st in the 2nd stage, and stopping muons, which will be passed onto fitter stopmu2nd in the 2nd stage.

2. The second stage uses fitters stopmu2nd, thrumu1st, fstmu, thrumu2nd and NNfit to further reject the downward-going events. The logic in this stage is very simple — all the events from stage 1 will pass through all the fitters, if identified as upward-going events with goodness-of-fit above certain thresholds, they will be saved as UP_{μ} candidates for the final eye scan; if identified as downward-going events with goodness-of-fit above certain thresholds, they will be rejected as cosmic ray muons;

if identified neither as downward-going nor as upward-going but as horizontal by at least one of the fitters or upward by thru1st, they will be saved as $UP\mu$ candidates for the final eye scan. The rest are rejected.

Eye scan

The final eye scan over the $UP\mu$ candidate events are performed by experienced physicists using event displayers. The scanning is performed by two physicists independently first. Then they come together to make final decision.

Event classification

The following quantities are calculated for each event:

- $n_{OD,entry}$: number of OD hits between 800 ns and 1,300 ns and 8 m around the entry point of OD
- $n_{OD,exit}$: number of OD hits between 800 ns and 1,300 ns and 8 m around the projected exit point of OD

An event is considered as a stopping muon event if $n_{OD,entry} \geq 10$ and $n_{OD,exit} < 10$; otherwise, a through-going muon event.

Through-going muon events are further divided into non-showering events and showering events by comparing the observed p.e.s with the expected number of p.e.s assuming pure ionization energy loss. Detailed procedure is recorded in Chapter 7 of Dr. Desai's Ph.D. dissertation [74].

4.2 Event reconstruction

After the data reduction, event reconstruction algorithms are applied on all the neutrino events. This procedure is same for both Monte Carlo and data. As we mentioned in the previous section, some of the reconstruction algorithms are used during the data reduction also. For the Super-K water Cherenkov detector, we have the following reconstruction algorithms: vertex fitting, ring counting, particle identification, precise vertex fitting, and momentum determination.

4.2.1 Vertex reconstruction

Vertex fitting process has three parts, **point fitter**, ring edge search and **TDC fitter**.

Point fitter

Vertex position is first roughly estimated using the timing information of ID hits assuming all the photons are emitted at the same time from a point source at position (x, y, z) . A variable called “time residual” is defined in this step as follow,

$$t_i = t_i^0 - \sqrt{(x - x_i)^2 + (y - y_i)^2 + (z - z_i)^2} / v_{water} \quad ,$$

where t_i^0 is the hit time of the i^{th} PMT, whose position is (x_i, y_i, z_i) , in ID; v_{water} is speed of light in water. Finding the point (x, y, z) which maximizes the following goodness gives us the rough position of the vertex,

$$G_p = \frac{1}{N} \sum_{i=1}^N e^{-\left(\frac{t_i - t}{1.5\sigma}\right)^2 / 2} \quad ,$$

where, N is the number of hit PMTs, \bar{t} is the average of t_i 's, and σ is the PMT timing resolution (2.5 ns).

The particle direction is also roughly estimated by adding all vectors which are weighted by the corresponding PMT charges connecting the vertex and all the hit PMTs:

$$\vec{d} = \sum_{i=1}^N q_i \vec{d}_i \quad ,$$

where, \vec{d}_i is the unit vector connecting the vertex and the i^{th} PMT and q_i is the number of p.e.s deposited in the i^{th} PMT. Certainly, \vec{d}_i is not normalized here yet.

Ring edge search

In this step, the direction and the outer edge of the dominant ring is determined. First, an estimator is defined as follow,

$$Q(\theta_{edge}) = \frac{\int_0^{\theta_{edge}} d\theta pe(\theta)}{\sin \theta_{edge}} \left(\frac{dpe(\theta)}{d\theta} \right)^2 e^{-\left(\frac{\theta_{edge} - \theta_C}{\sigma_\theta}\right)^2} \quad ,$$

where $pe(\theta)$ is the angular distribution of the observed charge as the function of opening angle θ with respect to \vec{d} from the point fitter, the azimuthal direction is integrated out; θ_C and σ_θ are the Cherenkov radiation angle and its resolution.

θ_{edge} is found by requiring:

1. $\theta_{edge} > \theta_{peak}$, where θ_{peak} is the position where $pe(\theta)$ takes its maximum;
2. $d^2pe(\theta)/d\theta^2|_{\theta_{edge}} = 0$, where θ_{edge} is the first point away from θ_{peak} which satisfies this equation.

TDC fitter

After the ring edge is found, **TDC fitter** is called to determine the vertex more precisely. **TDC fitter** is based on the same principles used by **point fitter**: finding the point which reproduces the observed photon distributions the best. Using the information from previous two step, by considering the following factors:

1. Photons are emitted along the track of charged particles;
2. Photons observed outside the ring edge are treated as scattering light,

TDC fitter is able to provide more precise estimation for the vertex position.

4.2.2 Ring counting

After the vertex, direction and the Cherenkov opening angle of the most energetic ring is constructed using the vertex fitters, further attempts are tried to see whether the event is a single- or multi-ring one. The algorithm consists of two steps:

1. Search for ring candidates using Hough transformation,
2. Test whether the candidates are real Cherenkov rings.

Searching ring candidates

Hough transformation is used to search for ring candidates. In order to perform Hough transformation on our cylindrical surface, the ID PMTs are remapped onto a sphere whose center is the vertex found by the vertex fitter and the surface of the sphere is divided into 72×36 bins in the $\theta - \phi$ plane. To find the extra rings, expected Cherenkov charges are subtracted from the PMTs and the remaining charges are redistributed using Hough transformation with a Cherenkov opening angle of 42° . The charge peaks after the transformation are the directions of ring candidates.

Testing ring candidates

The candidates found by Hough transformation are tested using likelihood method. The basic idea is to compare the likelihood function values of the case of n rings and the case $n + 1$ rings, starting from $n = 1$ till the n -ring case is preferred over the assumption of $n + 1$ rings. The details are provided in Dr. Ishitsuka's dissertation [102] or Dr. Clark's dissertation [103].

4.2.3 Particle identification

Super-K detector can identify two types of Cherenkov rings: e -like and μ -like, according to the ring pattern and the opening angle. Tracks of electrons, particularly low-energy electrons, are not straight due to multiple scatterings thus electrons produce rather diffused Cherenkov rings. However, muons, as they are heavier, have more straight tracks thus intend to produce much sharper Cherenkov rings. This difference is the basis of the particle identification (PID).

The PID likelihood functions being e -like, L_e , or μ -like, L_μ , for a Cherenkov ring are constructed using the expected charges (assuming the charged particle producing this ring as electron or muon) and the observed charges of the PMTs inside the opening angle of $1.5\theta_C$. By comparing the values of those two likelihoods, the charged particle type is decided.

4.2.4 Precise vertex fitter

TDC fitter is not sensitive to the shift along the particle track due to the fact it uses the time residuals. To overcome this short-coming, **MS fitter** is made to improve the vertex resolution in the longitudinal direction.

In **MS fitter**, the likelihood function used in PID is employed with a fixed Cherenkov

angle θ_C which is calculated under the assumption of the decided particle type. The algorithm iterates in the following way:

1. Change the vertex position in the transverse direction with respect to the particle track direction to maximize the goodness defined in **TDC fitter**.
2. Move the vertex position along the track direction to find the position where the likelihood function, L_e or L_μ depending on the particle type, defined in PID algorithm is maximized.
3. Adjust the direction to maximize L_e or L_μ .
4. repeat till the shift on the vertex is less than 5 cm and the change on the direction is less than 0.5° .

4.2.5 Momentum reconstruction

The momentum of the charged particle producing a certain Cherenkov ring is reconstructed with the information of the vertex, the direction and the PID. For Cherenkov radiation, there is a very good correlation between the radiated photons and the particle momentum. In order to get the corrected number of photons radiated by the particle, the detected photoelectrons are corrected for by the effective photo-sensitive area of the PMT, the pathlength and the light attenuation and scattering in water. The total number of corrected photoelectrons, R_{tot} , is defined as the total number of photoelectrons in a 70° opening angle and between the time window of -50 ns and +250 ns around the time residual peak. The relation between R_{tot} and the particle momentum is obtained by Monte Carlo simulation.

4.2.6 Upward-going muon event reconstruction

The reconstruction of UP_μ events are different from the FC and PC events. There are three fitters used: **OD fitter**, **TDC fitter**, and **Upmu fitter**. According to the track length, total p.e.s in ID, the number OD clusters and the direction differences of these three fitters, the reconstruction process choose different fitters as the results. Details are recorded in Ref. [74].

Due to fact that the primary neutrino interactions of Up_μ events are in Earth, the correlation between the muon momentum and parent neutrino energy is relatively weaker. In addition, the momenta of upward through-going muons can not be reconstructed since they penetrate the Super-K detector. So the most valuable information from the UP_μ reconstruction is the direction, which has better correlation with the parent neutrino directions than FC and PC events.

4.3 Summary

Super-K events are categorized into following categories according to the locations of neutrino interactions and the topology of the events:

- Contained events: primary neutrino interactions are in ID
 - Fully contained events (FC): final state particles are completely contained within ID
 - * Single-ring e -like events
 - * Single-ring μ -like events
 - * Multi-ring e -like events: the most energetic ring is e -like
 - * Multi-ring μ -like events: the most energetic ring is μ -like

Each of these FC event samples are further divided into sub-GeV and multi-GeV samples according to their visible energy,

- * Sub-GeV: $E_{vis} \leq 1.33$ GeV
- * Multi-GeV: $E_{vis} > 1.33$ GeV

– Partially-contained events (PC): final state particles enter OD

- * PC stopping: the muon penetrate ID but stop in OD
- * PC through-going: the muon penetrate both ID and OD

• Upward-going muons (UP_{μ}): primary neutrino interactions are in Earth and the muons enter Super-K detector

– Stopping muons: muons that stop in ID

– Non-showering muons: muons penetrate the detector and energy loss is mainly through ionization

– Showering muons: muons penetrate the detector and losing energy mainly through radiation

Figure 4.2 shows the parent neutrino energy spectra for different data samples based on the Monte Carlo simulation. We will talk how we get those neutral current enhanced samples in Chapter 6. As we see from the spectra, Super-K atmospheric neutrino covers a wide energy range from ~ 100 MeV to ~ 1 TeV. This is a big advantage for testing new physics at high energies.

4.3.1 Systematic uncertainties of data reduction

The data reduction algorithms for SK-I and SK-II are same except the cuts related to number of ID PMTs. So, the same kinds of systematic uncertainties are introduced in. However,

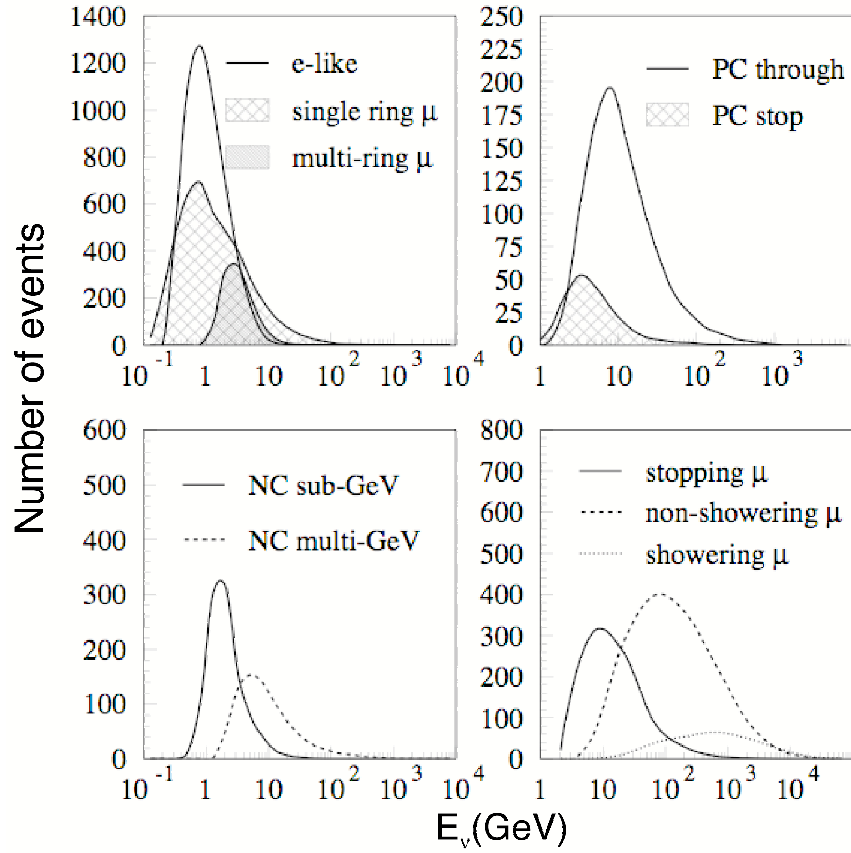


Figure 4.2: Parent neutrino energy spectra

the values are different between SK-I and SK-II. Since SK-II is not as good as SK-I due to less ID PMTs, systematic uncertainties which depend on the ID PMT coverage become larger.

Table 4.1 shows the values for SK-I and SK-II. Appendix B gives an example on how to evaluate the systematic uncertainty in PC reduction.

4.3.2 Systematic uncertainties of event reconstruction

The reconstruction algorithms are same for SK-I and SK-II except some parameters. So, the same set of systematic uncertainties are evaluated for SK-I and SK-II which are shown in Table 4.2.

Table 4.1: Super-K data reduction uncertainties

Systematic Uncertainty	Value (SK-I)	Value (SK-II)	Index
FC reduction	0.002	0.002	26
PC reduction	0.026	0.040	27
UP μ reduction	0.01	0.01	28
FC/PC separation	0.009	0.005	29
Non- ν background (e -like)	0.01	0.01	31
Non- ν background (μ -like)	0.01	0.01	32
Stopping/through-going μ separation	0.004	0.003	33
Non-showering μ background	0.015	0.030	40
Stopping μ background	0.17	0.24	41
Non- ν background (Multi-GeV single-ring e -like)	0.14	0.326	42
Non- ν background (Multi-GeV multi-ring e -like)	0.20	0.554	43
Non-showering/showering separation	0.0118	0.017	45
Showering μ background	0.13	0.24	46
PC stopping/through-going separation	0.12	0.166	47

Table 4.2: Systematic uncertainties in event reconstruction

Systematic uncertainty	Value (SK-I)	Value (SK-II)	Index
Ring separation	0.10	0.10	34
PID of single-ring events	0.01	0.01	35
PID of multi-ring events	0.10	0.10	36
Energy cut of stopping μ	0.011	0.011	38

Chapter 5

Mass-Induced $\nu_\mu - \nu_\tau$ Oscillation

In the framework of the Standard Model, there are three types of neutrinos, ν_e , ν_μ and ν_τ . That there are no more active neutrino flavors beyond these three is strongly supported by the experimental evidence from LEP experiments [13]. However, the LSND experiment measured a mass squared splitting which is different from both the solar and the atmospheric scales [104]. If the LSND result is confirmed, it could suggest there is a fourth flavor. Due to the constraints from LEP experiments, the fourth flavor must be sterile neutrino. We will discuss issues related to sterile neutrinos in the next chapter.

As we described in the first chapter, previous analysis [105] and results from experiments Chooz [38] and Palo Verde [39] indicate that the mixing between muon neutrinos and electron neutrinos are extremely small. Thus, a two-flavor analysis of $\nu_\mu - \nu_\tau$ oscillation for atmospheric neutrino is quite sufficient at the current experimental precision to extract mixing parameters between the second and third generations.

In this chapter, we will carry out the oscillation analysis assuming that muon neutrinos mix with tau neutrinos using both SK-I and SK-II atmospheric neutrino data. In order to provide more precise information on the mixing parameters, a finer binning of the reconstructed event energy is applied in the data analysis.

5.1 Data preparation

Mixing between muon neutrinos and tau neutrinos implies that the missing atmospheric muon neutrinos are turning into the tau type. For a water Cherenkov detector, it is not so easy to identify tau events [106] because tau lepton decays almost instantaneously and the final state particles consist of electrons, muons, or one or more pions which produce multi-ring signals without an easily identified leading charged lepton. In addition, due to the energy threshold of tau lepton production which is ~ 3.5 GeV, only a small portion of tau neutrinos interact in SK detector produce tau leptons. Thus, there is no much statistics available either. For the whole SK-I period, we only expect 78 tau events [106] assuming $\Delta m^2 = 2.4 \times 10^{-3} \text{eV}^2$. Super-K collaboration studied the tau appearance study using both likelihood method and neural network approach, and the results are consistent with $\nu_\mu - \nu_\tau$ oscillation assumption [106].

Due to the difficulties of identifying tau events and their low statistics, SK is basically a atmospheric neutrino disappearance experiment for the $\nu_\mu - \nu_\tau$ oscillation. These small amount of tau events (78 for SK-I and 43 for SK-II normalizing the livetimes) are categorized into e -like events and they have very little effects on the oscillation analysis compared to the total number of events. The survival probability of muon neutrinos is as follow:

$$P_{\nu_\mu \rightarrow \nu_\mu} = 1 - \sin^2 2\theta \sin^2 \frac{\Delta m^2 L}{4E} = 1 - \sin^2 2\theta \sin^2 1.27 \frac{\Delta m^2 (\text{eV}^2) L (\text{km})}{E (\text{GeV})}. \quad (5.1)$$

As we will show later, the zenith angle oscillation analysis is based on the comparison between the observed number of events and the expected ones. In order to know the expected number of neutrino events, we need to know the neutrino flux. As we mentioned

in Chapter 2, the systematic uncertainty on the absolute flux intensity of atmospheric neutrinos is as large as $\sim 20\%$. However, we do have better understanding on the flavor ratio. Thus, though electron neutrinos do not participate oscillations in the two generation framework for the atmospheric neutrino sector, e -like events can help to cancel the systematic uncertainty of the absolute neutrino flux. In order to increase the statistics of e -like events, we also extract charge current enhanced samples from FC multi-ring e -like events. The algorithm is based on a likelihood analysis using PID likelihood, momentum fraction of the most energetic ring, number of muon decay electrons, and distance between muon decay electron and primary neutrino interaction position [105].

The following data samples are used in our oscillation analysis:

- Fully-contained single ring e -like events
- Fully-contained multi-ring CC e -like events
- Fully-contained single ring μ -like events
- Fully-contained multi-ring μ -like events
- Partially contained events
- Upward-going muons

Neutral current events are not included since they do not provide any information for a $\nu_\mu - \nu_\tau$ oscillation analysis. But we will see that neutral current enhanced samples are helpful in the sterile neutrino analysis which we will discuss in next chapter.

5.1.1 Data binning

Examining the survival probability formula Eq. ??, the constraint on the mixing angle term $\sin^2 2\theta$ is mainly decided by available statistics. The mass-squared difference is coupled

with L/E , which means the better resolution on L/E , the better constraint we gain on Δm^2 . Zenith angle oscillation analysis has the advantage that it can utilize all the neutrino events to provide the best constraints on the mixing angle. In this analysis, pathlengths and energies of parent neutrinos are not reconstructed because the reconstruction can not be applied to some of the data samples, like $Up\mu$, or the reconstructed L and E are not correlated to the true values, like low energy multi-ring FC events.

Pathlength of a neutrino is determined by the production height and the zenith angle. The experimental variable which is the most closely correlated to the pathlength of the parent neutrino is the reconstructed zenith angle (θ_{rec}) of the event. The reconstructed direction of an event is decided based on the event type and reconstruction information: For FC single ring events, the reconstructed ring direction is the event direction; For FC multi-ring events, the total reconstructed momentum defines the event direction; For PC and $Up\mu$ events, directions of the leading muons define the event directions. We bin all neutrino events into 10 zenith angle bins based on $\cos\theta_{rec}$ value.

For contained neutrino events, *i.e.* FC and PC events, the experimental variables which are the most closely correlated to the parent neutrino energy are the visible energy or the total reconstructed momentum depending on the event types. Binning is carried out based on the logarithm of the reconstructed momentum or the visible energy. For PC events, in order to further improve the energy resolution, we separate the PC stopping events and the PC through-going events by comparing the expected OD hits and the observed OD hits [102]. The PC stopping and PC through-going events separation was made possible after the OD Monte Carlo was improved by tuning some of the simulation parameters. The tuning process is recorded in Appendix A.

For $Up\mu$ events, because the neutrino interactions happen in the Earth, there is no good correlation between the parent neutrino energy and the energy deposited in Super-K detector. However, the three categories of $Up\mu$ samples do statistically correspond to

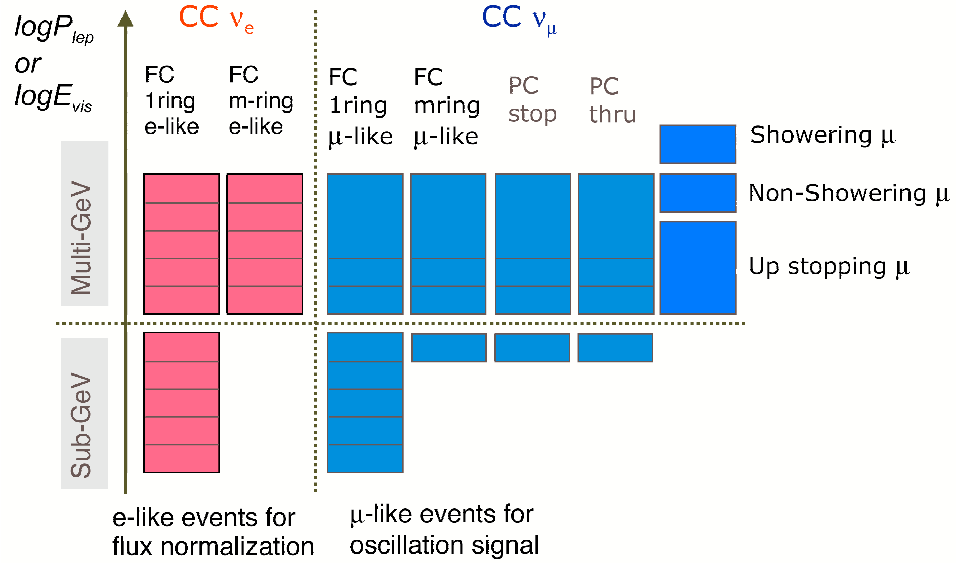


Figure 5.1: Binning strategy for the oscillation analysis

neutrinos with different typical energies. No further binning is done for $\text{Up}\mu$ events in terms of energies.

SK-I and SK-II data are binned in the same fashion. Figure 5.1 shows the energy binning for different SK samples. In total, we have 760 bins combining SK-I and SK-II data samples.

5.2 Oscillation Analysis

A least chi-square method called “pull method” [107] is used to extract the mixing parameters out of the data. The chi-square is defined as follows:

$$\chi^2 = \sum_{i=1}^n 2(N_i^{exp} - N_i^{obs} + N_i^{obs} \ln \frac{N_i^{obs}}{N_i^{exp}}) + \sum_{j=1}^m \left(\frac{\epsilon_j}{\sigma_j^{sys}}\right)^2. \quad (5.2)$$

Here, N_i^{obs} is the number of observed events in the i^{th} bin, σ_j^{sys} is the j^{th} systematic uncertainty, ϵ_j is the pull value on the j^{th} systematic uncertainty, N_i^{exp} is the expected

number of events in the i^{th} bin, and n and m are number of data bins and number of systematic uncertainties respectively. In total, for $\nu_\mu - \nu_\tau$ oscillation analysis, there are 760 data bins as shown in the previous section and 70 systematic terms recorded in previous chapters.

Among the systematic uncertainties, as we shown in previous chapters, there are 14 neutrino flux uncertainties recorded in Table 2.1; there are 12 neutrino interaction related ones which are the same for SK-I and SK-II recorded in Table 3.2; there are 12 detector related systematic uncertainties which are different between SK-I and SK-II recorded in Table 3.1, Table 4.1 and Table 4.2; and there is one solar activity term recored in Table 2.1 which has the same uncertainty value but different pulls for SK-I and SK-II. The effects of the systematic uncertainties on the expected number of events in each bin are taken into account in the following way:

$$N_i^{exp} = (1 + \sum_{j=1}^m f_j^i \epsilon_j) N_i^{exp0}$$

Here, N_i^{exp0} is the predicted of number of events in the i^{th} bin without considering the systematic uncertainties and f_j^i is the response coefficient of the number of the events in the i^{th} bin with respect to the j^{th} systematic uncertainty. N_i^{exp0} is calculated in the following way:

$$N_i^{exp0} = N_i^{nosc} P_{survival}, \quad (5.3)$$

where N_i^{nosc} is the predicted number of events without considering oscillation and $P_{survival}$ is the neutrino survival probability. And f_j^i is evaluated using MC method.

To find the parameters minimizing the χ^2 , the solutions to the pull terms can be ob-

tained by taking $\partial\chi^2/\partial\epsilon_k = 0$:

$$\frac{\sum_{i=1}^n N_i^{obs} f_k^i}{\sum_{j=1}^m (\epsilon_j f_j^i + 1)} - \frac{\epsilon_k}{\sigma_k^{sys}} = \sum_{i=1}^n f_k^i N_i^{exp0}. \quad (5.4)$$

Keeping only the linear terms of $1/\sum_{j=1}^m (\epsilon_j f_j^i + 1)$, since we expect ϵ_i 's are small, this non-linear equation is transferred into a linear equation and can be solved by inverting a $m \times m$ matrix. However, such a procedure does not apply to the mixing parameters. So, we prepare a grid in the mixing parameter space and solve the linear equation set at each grid point for the pulls ϵ_i . The grid point with the minimum chi-square values gives the best-fit values for the mixing parameters.

5.3 Results and Discussion

Based on the previous experimental results of Super-K, the parameter space we choose for the $\nu_\mu - \nu_\tau$ oscillation analysis is $\sin^2 2\theta \in [0.7, 1.2]$ and $\log \Delta m^2 \in [-3, -2]$ with the unit of Δm^2 as eV^2 . The parameter space is divided into 201×201 points uniformly. The best-fit values are $\sin^2 2\theta = 1$ and $\Delta m^2 = 2.5 \times 10^{-3} eV^2$.

Figure 5.2 shows the best-fit zenith angle distributions. We see that the $\nu_\mu - \nu_\tau$ oscillation accounts well for the missing muon neutrinos. Figure 5.3 shows the chi-square contours corresponding to 68%, 90% and 99% confidence levels respectively and Fig. 5.4 shows the χ^2 behaviors around the best-fit values of $\sin^2 2\theta$ and Δm^2 .

At 68% confidence level, the allowed parameter space is $\sin^2 2\theta > 0.95$ and $2.2 \times 10^{-3} eV^2 < \Delta m^2 < 2.7 \times 10^{-3} eV^2$. The chi-square value at the best-fit point is 848 with the number of degrees-of-freedom (*dof*) 755. Due to the fine binning we adopted, many of the bins have very small number of entries. Thus, the *p-value* corresponding to this

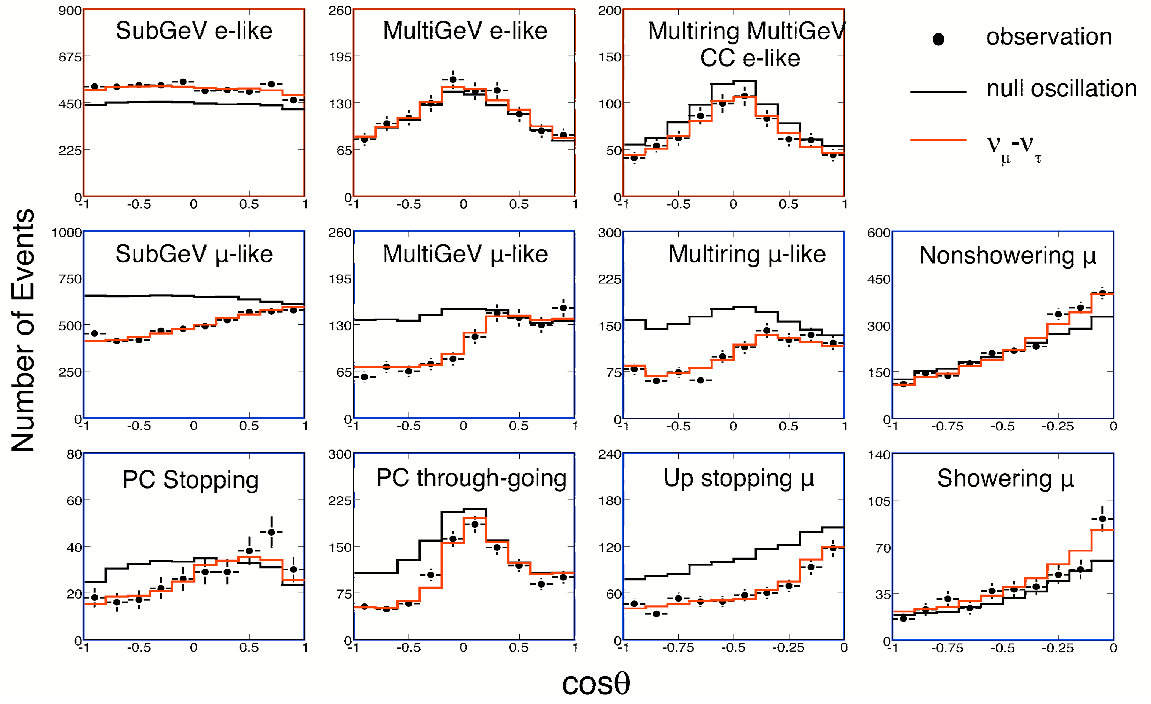


Figure 5.2: Chi-square contours on the $\Delta m^2 - \sin^2 2\theta$ parameter plane for $\nu_\mu - \nu_\tau$ mixing

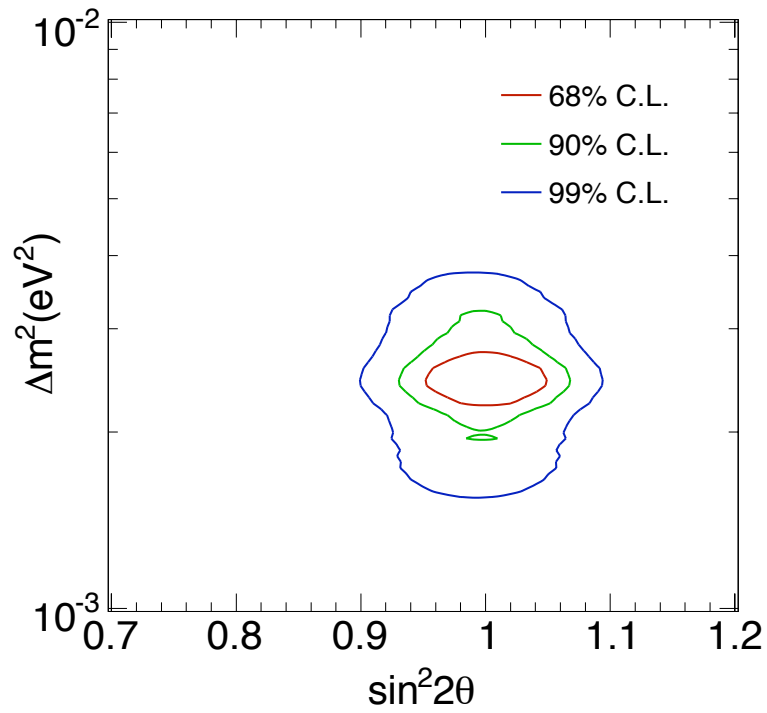


Figure 5.3: Chi-square contours on the $\Delta m^2 - \sin^2 2\theta$ parameter plane for $\nu_\mu - \nu_\tau$ mixing

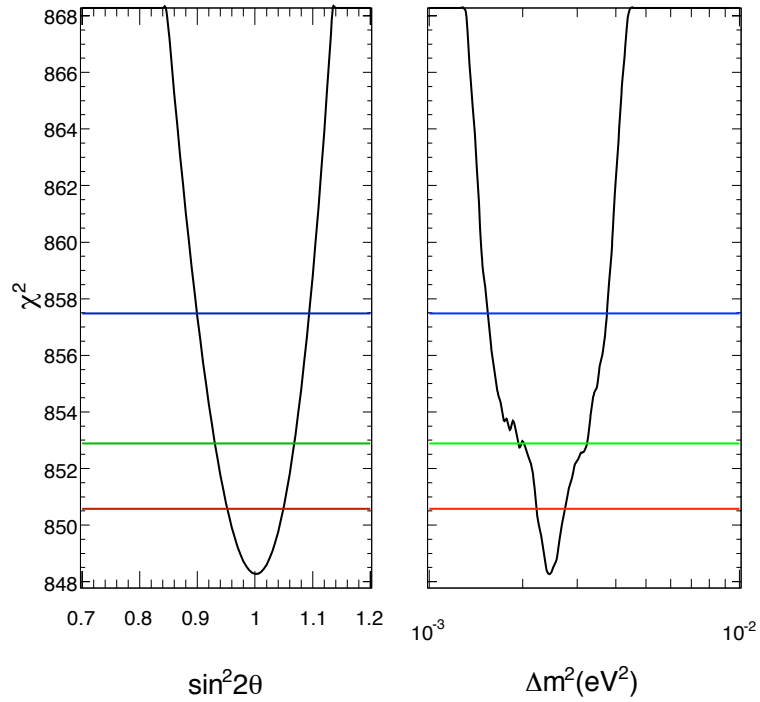


Figure 5.4: 1D chi-square projections

chi-square value should be calculated via Monte Carlo instead of assuming a chi-square distribution with $dof = 755$. A custom toy MC program is designed by assuming each bin follows a Poisson distribution with the Poisson parameter λ equals to the expected number of entries. Our simulation shows that the p - $value$ is 18% for the least χ^2 value we obtained.

Figure 5.5 shows the pull term distributions. It follows a Gaussian distribution, which is expected [107]. A Gaussian fit gives the mean $\mu = 0.04$ and the standard deviation $\sigma = 0.4$. In Ref. [107], a Gaussian distribution with a standard deviation of 1 is expected in principle. However, due to the fact that we are generally conservative on some systematic uncertainties, the Gaussian distribution for the pulls we obtained here has a smaller standard deviation.

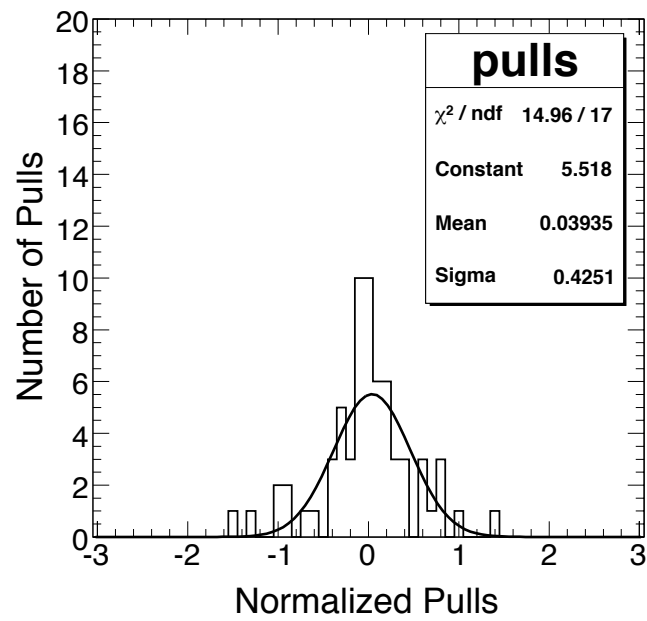


Figure 5.5: The distribution of normalized pulls with its Gaussian fit results

Chapter 6

Constraints on Sterile Neutrinos

Mass induced neutrino oscillations have been widely accepted in recent years as experimental evidence accumulates [15, 35, 108, 36, 6]. The analysis we did in the last chapter is based on this theory, and indeed, the model fits the observation very well. However, whether there are sterile neutrinos (ν_s) involved in neutrino oscillations is of both experimental and theoretical interests. There are observations which are in favor of the existence of sterile neutrinos, for example: if there are sterile neutrinos, the LSND anomaly could be explained assuming the existence of sterile neutrinos [104, 109]; supernova rapid neutron capture process (r -process) problem can be solved [110, 111]. Theoretically, a simple way to give neutrino mass is to have Dirac right-handed neutrinos which are $SU(2)$ singlet thus must be sterile [21, 22].

Previous studies using 1100 live days of SK-I data rejected the $\nu_\mu - \nu_s$ oscillation at 99% confidence level [112]. In this chapter, using the pull method described in the previous chapter and the complete SK-I and SK-II data sets, we design a systematic way to do model comparison to test which model explains SK data better. We will also study how much admixture of sterile neutrinos is allowed in the atmospheric neutrino oscillation.

6.1 Comparison of $\nu_\mu - \nu_\tau$ and $\nu_\mu - \nu_s$ oscillations

6.1.1 Signatures of $\nu_\mu - \nu_s$ oscillation

For the two competing models, $\nu_\mu - \nu_\tau$ and $\nu_\mu - \nu_s$, though the 2nd neutrino is not identified, there are some signatures for us to tell two oscillations apart. Firstly, sterile neutrinos do not interact with matter at all so they do not even make any neutral current signals in SK detector; secondly, because the potentials experienced by ν_μ and ν_s in matter are different, matter effect modifies the survival probabilities of muon neutrinos, as we described in Chapter 1.

To utilize the first signature, we need to identify the neutral current events. For a water Cherenkov detector, by identifying the π^0 particles which are produced in neutral current single-pion neutrino reactions, neutral current events can be enriched quite well [113]. However, in order to keep as many events as we can, we do not adopt the tight cuts in Ref. [113]. As we will see later, even without the tight cuts in Ref. [113], the neutral current enhanced events based on the less restricted cuts defined below can differentiate two models quite well already. For sub-GeV events, the cuts we use to enhance neutral current events are:

- Multi-ring events: π^0 particles produced in neutral current reactions produce two e -like rings.
- The most energetic ring is e -like: this cut is chosen to get rid of CC ν_μ events.
- $400 \text{ MeV} < E_{vis} < 1330 \text{ MeV}$: this cut is chosen to guarantee certain directional information of the parent neutrinos.

As for the multi-GeV samples, we simply use the left-over events after enhancing the charged current enhanced events using the likelihood method developed in the previous

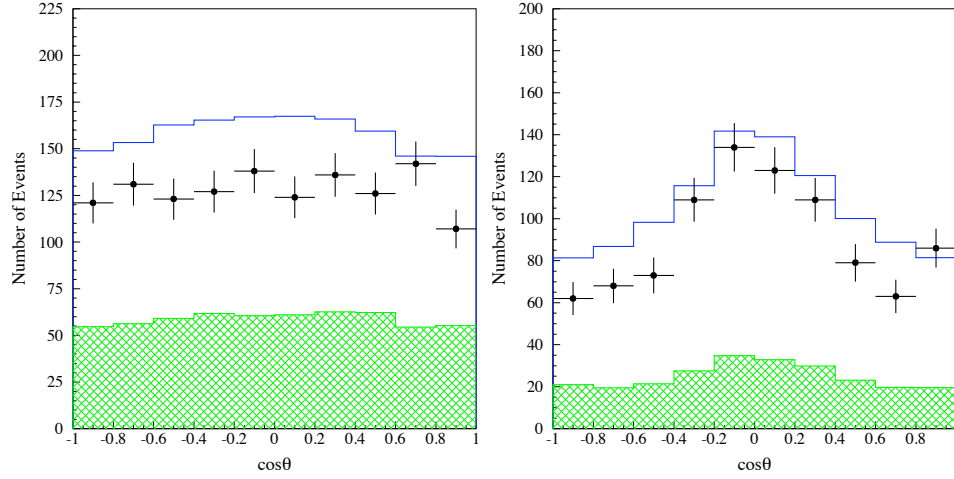


Figure 6.1: Zenith angle distributions of neutral current enhanced samples. Left: sub-GeV; right: multi-GeV

Table 6.1: Portions of NC and CC events in the NC enhanced data samples

	NC events	CC ν_μ	CC ν_e
Sub-GeV sample	37%	22%	41%
Multi-GeV sample	24%	35%	41%

chapter.

After applying these cuts, we have the zenith distributions of neutral current enhanced samples shown in Fig. 6.1. The hatched areas are neutral current events based on the Monte Carlo simulation. The percentages of neutral current events and charge current ν_μ contaminations are shown in Table 6.1.

The second signature of $\nu_\mu - \nu_s$ oscillation is the matter effect. To have a quantitative idea about the matter effect experienced by $\nu_\mu - \nu_s$ oscillations for atmospheric neutrinos, we calculate the survival probability of muon neutrinos crossing the Earth using the method described in Chapter 1 and the Earth density profile provided by PREM model [114]. As we can see from Fig. 6.2, for atmospheric neutrinos, the oscillation probability is indeed suppressed by the matter effect around and above 10 GeV.

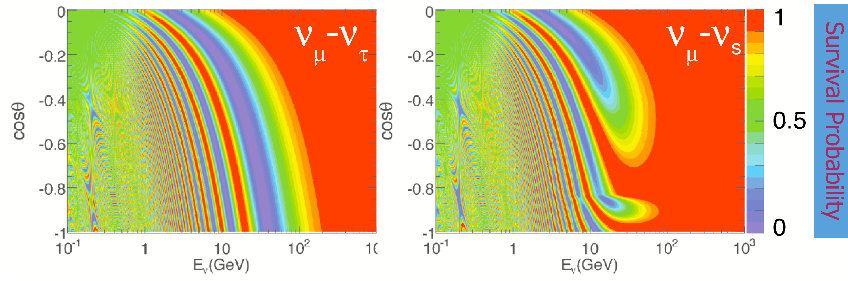


Figure 6.2: Survival probabilities of muon neutrinos crossing the Earth

6.1.2 Best-fits of two models

We now have both charged current and neutral current enhanced data samples to do the oscillation analysis. Considering that the uncertainty on total number of multi-ring e -like events is relatively big, we give neutral current enhanced an independent flux normalization, just like we did for the charged current enhanced e -like events. As for the binning of these neutral current enhanced samples, the sub-GeV neutral current events are treated as one energy bin. The multi-GeV sample is divided into 4 energy bins based on $\log E_{vis}$ values since the parent neutrinos have wider energy spread. Both samples are divided into 10 zenith angle bins based on the reconstructed event direction.

Using the same least chi-square method, we perform a $\nu_\mu - \nu_\tau$ oscillation using both CC and NC data samples. The same best-fit values for the mixing parameters are obtained. However, the goodness-of-fit is worse compared to the results based on CC samples only. The minimum chi-square is 971.2 with a number of degree-of-freedom 853. Using the same toy Monte Carlo procedure, we found the p -value is 7.3%. Figure 6.3 shows the chi-square confidence contours. As for the $\nu_\mu - \nu_s$ oscillation, we simply replace the $P_{survival}$ for muon neutrinos in Eq. 5.3 with a routine which has the matter effect implemented. Maximal mixing is still preferred by $\nu_\mu - \nu_s$ oscillation as shown in Fig. 6.4. However, the Δm^2 value is driven up a bit, $3.5 \times 10^{-3} \text{eV}^2$. This is because, as we argued in the previous sub-section, the survival probabilities of $\nu_\mu - \nu_s$ oscillations are suppressed, thus,

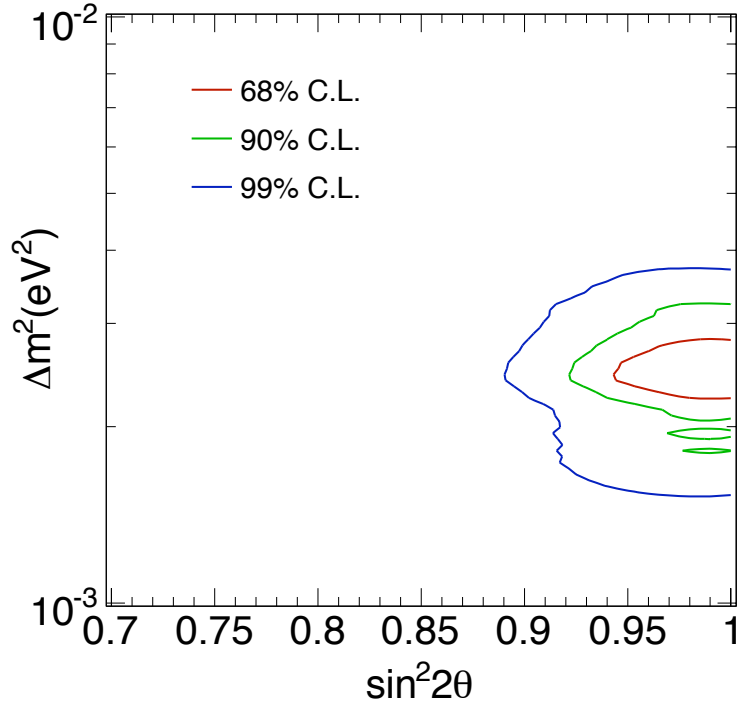


Figure 6.3: χ^2 contours of $\nu_\mu - \nu_\tau$ oscillation (with NC enhanced samples)

in order to fit the Super-K data, the best-fit value of Δm^2 is increased to compensate for this suppression, which is also why the constraint on mixing angle is tighter than the $\nu_\mu - \nu_\tau$ case. The chi-square value at the best-fit point is 1023.6 with the same number of degree-of-freedom, which is much worse than $\nu_\mu - \nu_\tau$ model. The difference 52.4 corresponds to a 7.2σ exclusion level for the pure $\nu_\mu - \nu_s$ model.

Figure 6.5 shows the comparison of best-fit zenith angle distributions. For many bins of the data sample, the $\nu_\mu - \nu_s$ model reproduces SK observation as well as the $\nu_\mu - \nu_s$ model. However, for sub-GeV neutral current enhanced events, PC through-going events, up μ stopping events and non-showering μ events, the $\nu_\mu - \nu_\tau$ model fits the data better than the $\nu_\mu - \nu_s$ model. Table 6.2 shows the detailed chi-square differences for different categories of events. The $\Delta\chi^2$ from data bins is 38.3. And Fig. 6.6 shows the comparison of the distributions of the pull terms. The pull term distribution of the $\nu_\mu - \nu_s$ oscillation is

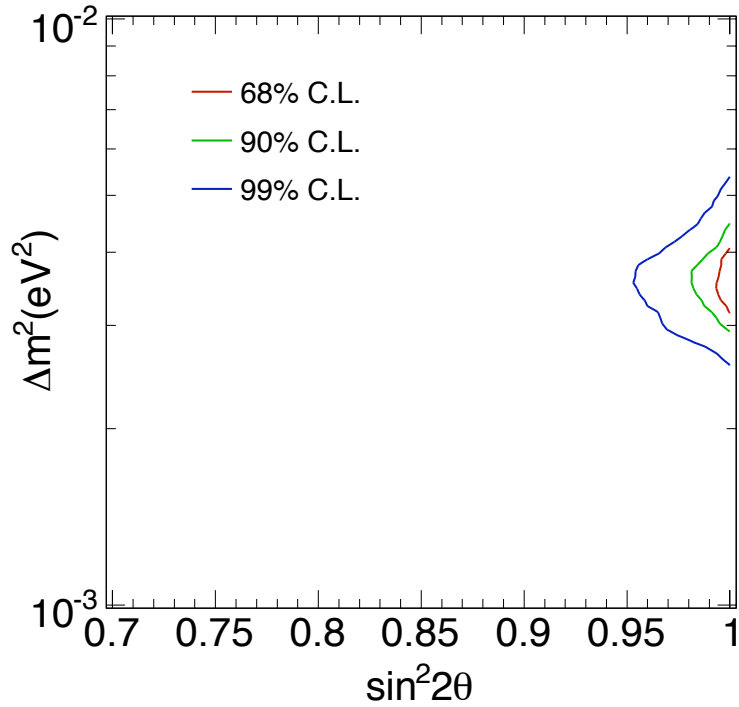


Figure 6.4: χ^2 contours of the $\nu_\mu - \nu_s$ oscillation (with NC enhanced samples)

wider than the $\nu_\mu - \nu_\tau$ one, which is another sign that $\nu_\mu - \nu_\tau$ oscillation is a better model accounting for the atmospheric neutrino data. Pull terms contribute 14.1 to the chi-square difference out of the total difference 52.4.

The $\nu_\mu - \nu_s$ model can not reproduce sub-GeV neutral current enhanced events as well as the $\nu_\mu - \nu_\tau$ model. The $\nu_\mu - \nu_\tau$ model expects the data fairly flat which is what we observe. However, for the $\nu_\mu - \nu_s$ model, the loss of neutral current events makes the expected distribution tilted toward upward going bins where muon neutrinos oscillate into sterile ones.

As we showed in Fig. 6.2, around the atmospheric Δm^2 scale, the strongest matter effect happen around 10 GeV. The typical energy of PC through-going events, $Up\mu$ stopping events and non-showering μ events is around this scale, which is why these events can differentiate the two models better than other types of neutrino events. We also see

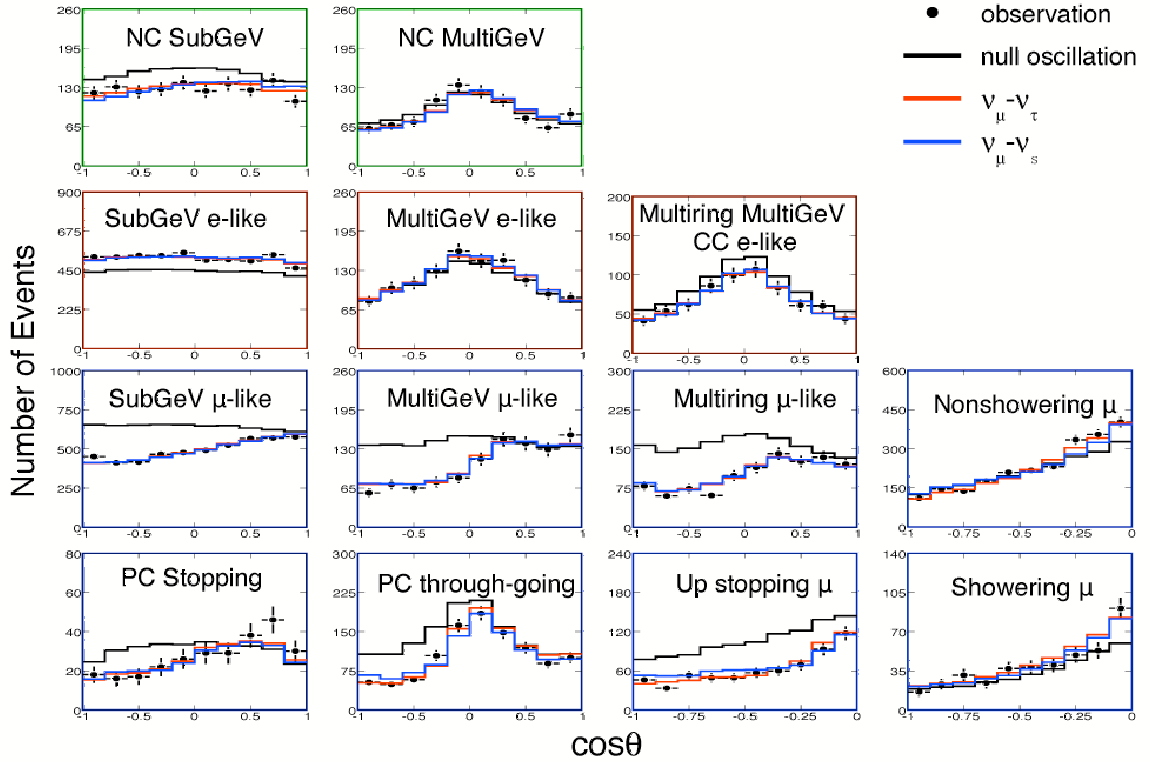


Figure 6.5: Comparison of the best-fit zenith angle distributions of $\nu_\mu - \nu_\tau$ and $\nu_\mu - \nu_s$ oscillations

Table 6.2: Chi-square difference breakdown ($\Delta\chi^2 = \chi^2_{\nu_\mu - \nu_s} - \chi^2_{\nu_\mu - \nu_\tau}$)

Data Samples	Bins (SK-I+SK-II)	$\chi^2_{\nu_\mu - \nu_s}$	$\chi^2_{\nu_\mu - \nu_\tau}$	$\Delta\chi^2$
Single ring sub-GeV e -like	50+50	104.8	104.0	0.8
Single ring multi-GeV e -like	50+50	108.6	110.7	-2.1
Multi-ring multi-GeV CC e -like	50+50	86.6	85.8	0.8
Single ring sub-GeV μ -like	50+50	104.9	106.1	-1.2
Single ring multi-GeV μ -like	30+30	64.8	66.8	-2.0
Multi-ring μ -like	40+40	79.3	75.5	3.8
NC-enhanced sub-GeV events	10+10	19.5	14.5	5.0
NC-enhanced multi-GeV events	40+40	105.7	104.5	1.2
PC stopping μ	40+40	128.7	125.8	2.9
PC through-going μ	40+40	114.4	102.1	12.3
Upward stopping μ	10+10	21.1	14.1	7.0
Upward non-showering μ	10+10	28.1	16.9	11.2
Upward showering μ	10+10	24.5	25.0	-1.5
TOTAL	430+430	991.1	952.8	38.3

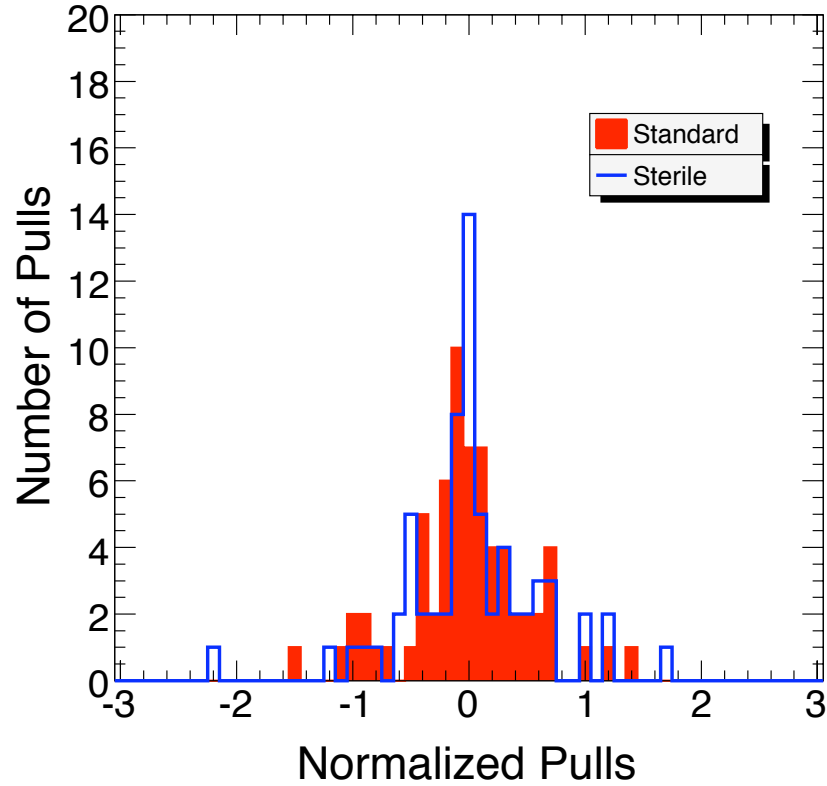


Figure 6.6: Distributions of the normalized pull terms of $\nu_\mu - \nu_\tau$ and $\nu_\mu - \nu_s$ oscillations that though neutral current enhanced events help to tell two models apart, it is mainly the matter effect that distinguish two models due to the advantages such as long baselines, high energies and high matter densities that atmospheric neutrinos possess compared to long baseline experiments.

6.2 An admixture model

Compared to $\nu_\mu - \nu_\tau$ oscillation, the fact that the $\nu_\mu - \nu_s$ oscillation is excluded at 7.2σ level does not mean that there is no involvement of sterile neutrinos in Super-K atmospheric neutrino oscillations. It is still possible that a certain portion of muon neutrinos are oscillating into sterile neutrinos besides the dominating $\nu_\mu - \nu_\tau$ oscillation. In this section,

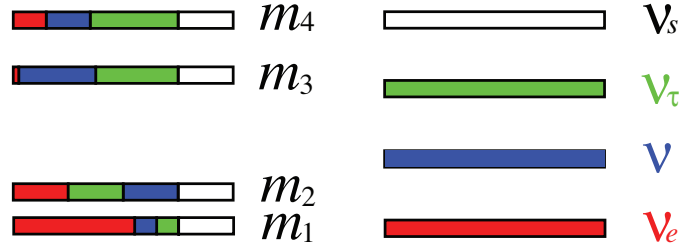


Figure 6.7: A case of 2+2 mass hierarchy and four-flavor mixing

we will study a case of the admixture of sterile neutrinos.

In the case of 2+2 mass hierarchy shown as the diagram in Fig. 6.7, according to G. L. Fogli *et. al.* [115], based on the current experimental results, the four flavor mixing can be transformed into two 2-flavor mixings by constructing two superposition states of ν_τ and ν_s in the following way:

$$\begin{pmatrix} \nu_+ \\ \nu_- \end{pmatrix} = \begin{pmatrix} \cos \xi & \sin \xi \\ -\sin \xi & \cos \xi \end{pmatrix} \begin{pmatrix} \nu_\tau \\ \nu_s \end{pmatrix}.$$

For the atmospheric sector, the oscillation now is between ν_μ and ν_+ which is a superposition state: $\cos \xi |\nu_\tau\rangle + \sin \xi |\nu_s\rangle$. Thus, the portion of sterile neutrinos is $\sin^2 \xi$. Accordingly, the matter effect strength is weakened by a factor of $\sin^2 \xi$. Now, we have 3 parameters in our oscillation: the mixing angle between $|\nu_{m_3}\rangle$ and $|\nu_{m_4}\rangle$, $\Delta m^2 = m_4^2 - m_3^2$ and the portion of sterile neutrinos $\sin^2 \xi$. Since the maximal mixing is a very strong constraint, we are going to assume maximal mixing in our analysis, *i.e.* $\sin^2 2\theta = 1$.

Using the same least chi-square framework, the best-fit is $\sin^2 \xi = 0$ which means Super-K data prefer zero amount of sterile neutrino involvement, see Fig. 6.8. However, at 90% C.L., we do allow 23% of sterile neutrino admixture. Compared to the limit of 67% at 90% C.L. set by Fogli *et al* in Ref. [115] using the published Super-K data, our limit using the complete SK-I and SK-II data sets is much more stringent.

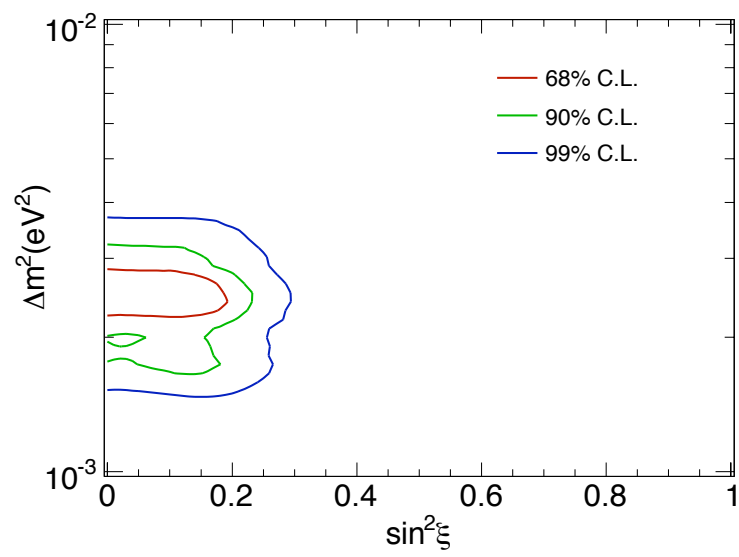


Figure 6.8: The ν_s admixture allowance

Chapter 7

Violations of Lorentz Invariance and CPT

The mixing of mass eigenstates is not the only physical origin of neutrino oscillation as pointed out in by Coleman and Glashow [44] and Kostelecky *et. al.* [45], Lorentz Invariance Violation (LIV) and CPT symmetry violation (CPTV) can also cause neutrinos to oscillate even they are massless.

In addition to the possibility of explaining current observations, it is also of theoretical importance to test the limits of those two fundamental symmetries [44, 116]. Lorentz Invariance and CPT symmetry have been long considered as fundamental laws of nature [117, 118, 119, 120] and serve as the corner stones of the quantum field theory. It is not completely clear that those symmetries will remain perfectly unbroken at all energies. Some quantum gravity theories predict that LIV and CPTV might happen at Planck scale, $M_P \sim 10^{19}\text{GeV}$. Thus testing the limits of their validity is a way to explore new physics beyond the Standard Model [44, 121, 116, 122, 123]. Neutrino oscillation, as a natural interferometer, is a promising method to test the low energy effects of LIV and CPTV.

7.1 An overview LIV and CPTV

LIV and CPTV are expected in some Planck scale theories through spontaneous symmetry breaking mechanism [44, 124, 125] or topological defects [126]. A. V. Kostelecky *et. al.* set up a general framework of LIV and CPTV called the Standard Model Extension (SME) [124] to study the possible observational effects at low energies. By treating the SM as a low energy effective theory of underlining fundamental physics, all the possible Lorentz symmetry breaking terms are added into the SM Lagrangian using the SM fields and gravitational fields.

Lorentz invariance is intimately related to CPT symmetry as stated in the CPT theorem [117, 118, 119, 120]: for a local field theory, Lorentz invariance leads to CPT symmetry. While breaking CPT symmetry naturally causes Lorentz invariance violation, which is proven in [127]. To generate neutrino oscillation effects, it turns out that the minimal renormalizable version of SME [44, 123] is sufficient. The “minimal” SME (mSME) only has a CPT-violating term and a CPT-conserving but LIV term in addition to the original Standard Model terms:

$$\mathcal{L}_{mSME} = -(a_L)_{\mu AB} \bar{L}_A \gamma^\mu L_B + \frac{1}{2} i (c_L)_{\mu\nu AB} \bar{L}_A \gamma^\mu \overleftrightarrow{D}^\nu L_B, \quad (7.1)$$

where the first term is CPT-odd and the second term is CPT-even. $L_{A/B}$, A and B run over the three generations e , μ , and τ , are the left-handed $SU(2)$ doublet fields, D is the covariant derivative, and the CPTV coefficients a_L and the LIV-only coefficients c_L arise from spontaneous symmetry breaking of more fundamental theories.

From the perspective of experimental observation, the LIV phenomena can be categorized into rotationally symmetric and rotationally asymmetric cases. We will study the rotational symmetric cases by keeping only the temporal components of those two inter-

action terms. Also, in this study, we always confine ourselves within two generations, ν_μ and ν_τ .

Under these considerations, the effective Hamiltonian in the flavor basis is:

$$(H_{eff})_{AB} = |\vec{p}| \delta_{AB} + \frac{1}{|\vec{p}|} \left((a_L)_{0AB} p^0 - (c_L)_{00AB} p^0 p^0 \right).$$

Two 2×2 matrices $(a_L)_{0AB}$ and $(c_L)_{00AB}$, where A and B are generation indices, are not necessarily diagonal in the flavor basis. First, let us consider the matrix $(c_L)_{00AB}$. Diagonalizing it by rotating the neutrino fields by θ_c gives two eigenvalues, c_a and c_b , and two eigenstates, $|\nu_a\rangle$ and $|\nu_b\rangle$. In this new basis, if neutrinos are massless, the Hamiltonian then becomes:

$$(H_{eff})_{ab} = pc + \begin{pmatrix} c_a & 0 \\ 0 & c_b \end{pmatrix} p.$$

The energies of the two eigenstates are

$$E_i = pc + pc_i = p(c + c_i), \quad i = a, b.$$

This can be interpreted as that two eigenstates have different speeds of light “ c ”, *i.e.* neutrinos travel at slightly different speeds in vacua. Those two eigenstates are defined as Maximal Attainable Velocities (MAV) [128, 44] eigenstates, which can be viewed as the energy eigenstates at infinite momentum for massive particles. Flavor eigenstates are superpositions of MAV eigenstates and vice versa:

$$\begin{cases} |\nu_\mu\rangle = \cos\theta_c|\nu_a\rangle + \sin\theta_c|\nu_b\rangle \\ |\nu_\tau\rangle = \cos\theta_c|\nu_a\rangle - \sin\theta_c|\nu_b\rangle \end{cases},$$

where θ_c is the mixing angle between two different MAV eigenstates, $|\nu_a\rangle$ and $|\nu_b\rangle$. We define $c^{TT} = c_a - c_b$; without loss of generality, we can always assume $c^{TT} > 0$. The survival probability of muon neutrinos after traveling a distance L is:

$$P_{\nu_\mu \rightarrow \nu_\mu} = 1 - \sin^2 2\theta_c \sin^2(c^{TT} LE/2) \quad . \quad (7.2)$$

A more general formula of this form is discussed in Ref. [129], which considers the energy dependence of the LIV effect. Ignoring neutrino mass, the survival probabilities of muon neutrinos are as follow:

$$P_{\nu_\mu \rightarrow \nu_\mu} = 1 - \sin^2 2\theta_c \sin^2(\kappa LE^{-\alpha}) \quad . \quad (7.3)$$

Where real number α is from the energy dependence effect of LIV, and the Planck scale, M_P , is already absorbed into κ which has dimension of energy to the power of $\alpha - 1$. This formula will also address the case of CPTV-induced oscillation when $\alpha = 0$, as we will discussion later.

With the analysis framework established in the previous chapter, we can easily test how well this model fits our observation using the Super-K atmospheric neutrino data. The parameter space here is spanned by $\sin^2 2\theta_c$, κ and α . Using the charged current data samples, the best-fit parameters are: $\sin^2 2\theta_c = 1$, $\kappa = 4.8 \times 10^{-3} \text{ eV}^{0.16}$, and $\alpha = 1.16$.

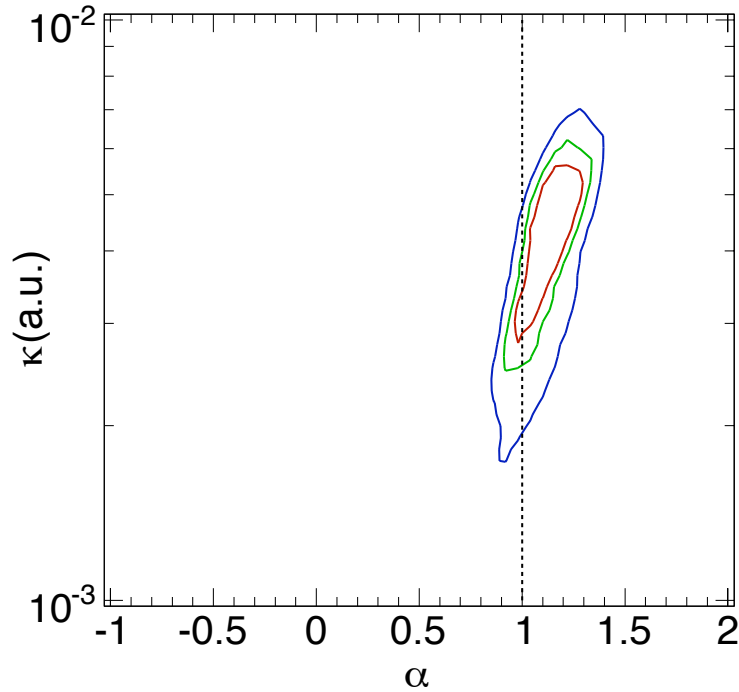


Figure 7.1: Allowed regions for parameters κ and α

Projecting the chi-square onto $\kappa - \alpha$ plane, Figure 7.1 shows the allowed regions of the parameters at confidence levels of 68%, 90% and 99%. To better examine the effect of energy dependence, the chi-square vs. α plot is shown in Fig. 7.2.

For the oscillation of the format $L \times E$, the chi-square value is 1060. Compared to standard L/E oscillation, $L \times E$ type oscillation is strongly disfavored. At 68% C.L., $0.95 < \alpha < 1.30$. Clearly, Super-K observation favors the standard L/E oscillation.

Now let us examine the effect of matrix $(a_L)_{0AB}$. The effective Hamiltonian in the basis of diagonalizing $(a_L)_{0AB}$ is:

$$(H_{eff})_{ab} = pc \pm \begin{pmatrix} a_a & 0 \\ 0 & a_b \end{pmatrix}.$$

Thus, the CPTV-breaking term will produce neutrino oscillation of the form ΔaL , where

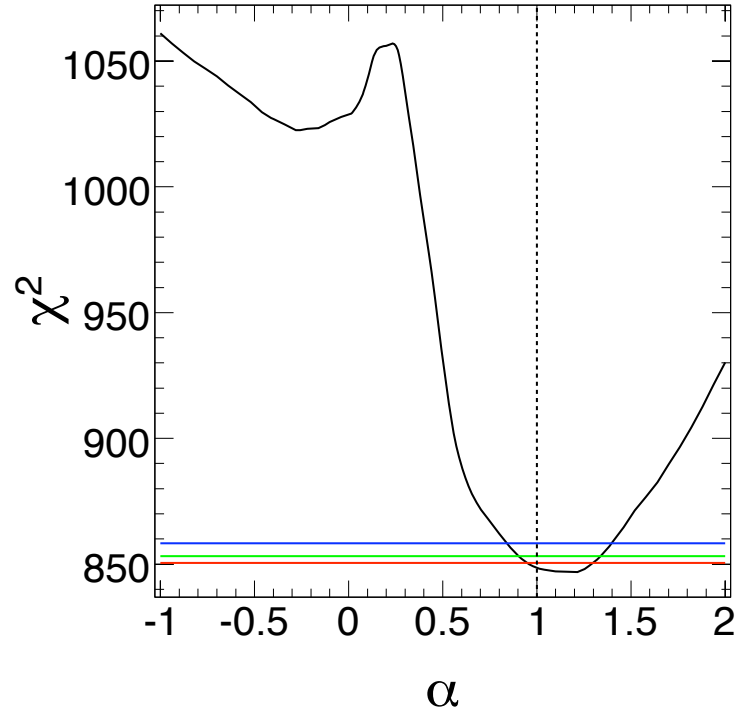


Figure 7.2: χ^2 versus α for a general oscillation formula

$\Delta a = a_a - a_b$ and a_a and a_b are the two eigenvalues of $(a_L)_{0AB}$. This oscillation is energy independent. Obviously, this is not the case we observe at Super-K. As shown in Fig. 5.2, the difference between the null oscillation prediction and the observation has a clear energy dependence. Also shown in Fig. 7.2, the $\alpha = 0$ case, which is the ΔaL oscillation, is strongly disfavored.

We then can ask the question: how much LIV and CPTV could be allowed in the Super-K atmospheric observation? We will address this issue in the following sections.

7.2 Allowed limits on LIV parameter

From the analysis in the last section, we see that it's unlikely for LIV alone to explain the atmospheric neutrino observation. However, if we consider the LIV-induced oscillation as

a sub-dominant effect in addition to the mass-induced oscillation, the survival probability becomes:

$$P_{\nu_\mu \rightarrow \nu_\mu} = 1 - \sin^2 2\Theta \sin^2(\Omega L/4),$$

where,

$$\begin{cases} \Omega \sin 2\Theta = |\Delta m^2 \sin 2\theta/E + 2c^{TT} e^{i\eta} E \sin 2\theta_c| \\ \Omega \cos 2\Theta = \Delta m^2 \cos 2\theta/E + 2c^{TT} E \cos 2\theta_c \end{cases}.$$

In this expression, Δm^2 and θ are the mass eigenstate mixing parameters as usual and η is the phase difference between two mixing matrices of the mass eigenstates and the MAV eigenstates.

Considering the two cases, $\eta = 0$ and $\eta = \pi$, assuming the best-fit mass eigenstate mixing parameter values based on Super-K atmospheric neutrino data, $\Delta m^2 = 2.5 \times 10^{-3} \text{eV}^2$ and $\sin^2 2\theta = 1$, we can test the limits allowed by Super-K atmospheric neutrino observation on the Lorentz invariance violating parameter c^{TT} . Using the chi-square analysis framework set up in Chapter 5, we can find the best-fit values in the parameter space spanned by $\sin 2\theta_c$ and c^{TT} .

In the $\eta = 0$ case, the best-fit values are $\sin^2 \theta_c = -0.12$ and $c^{TT} = 5 \times 10^{-25}$. Chi-square contours corresponding confidence levels 68%, 90% and 99% are shown in Fig. 7.3. We note that we obtain non-zero values for LIV parameters, $\sin 2\theta_c = -0.12$ and $c^{TT} = 0.5 \times 10^{-24}$. However, the zero value is within the first sigma level. At 90% C.L., the allowed LIV limit is: $c^{TT} < 1.2 \times 10^{-24}$. In the $\eta = \pi$ case, chi-square contours are shown in the right panel of Fig. 7.3. The best fit point is at $\sin 2\theta_c = -0.02$ and

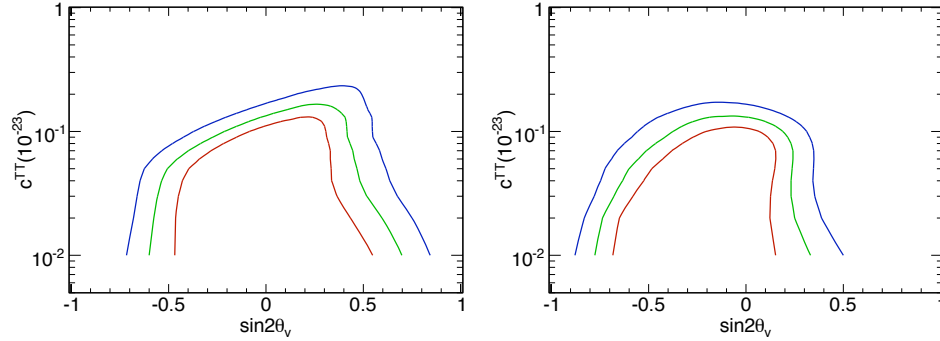


Figure 7.3: Chi-square contours of LIV. Left: $\eta = 0$; Right: $\eta = \pi$

$c^{TT} = 0.6 \times 10^{-24}$. At 90% C.L., the allowed LIV limit is: $c^{TT} < 1.3 \times 10^{-24}$.

7.3 The violation of CPT symmetry

7.3.1 Testing the LSND mass squared splitting scale

One *ad hoc* way to reconcile the anomalous LSND result [104] with other experiments is to allow neutrinos and anti-neutrinos have different mass squared splittings [130], which will violate CPT symmetry. As the conversed of the CPT theorem [117, 118, 119, 120], CPTV naturally leads to LIV and Ref. [127] provides a detailed proof.

Super-K atmospheric neutrinos, as we described in Chapter 2, have both neutrino and anti-neutrino components. It is not possible for the Super-K detector to identify the incident neutrino is neutrino or anti-neutrino event by event. However, due to the facts that neutrinos and anti-neutrinos have different fluxes, different interactions, and different final state particles, Super-K is able to see a statistical effect if neutrinos and anti-neutrinos have different mass squared splittings. Early work done by M. Messier on this topic can be found in Ref. [131].

Assuming maximal mixing for both neutrinos and anti-neutrinos, MC simulated zenith angle distributions are generated for different mass squared splittings for neutrinos and

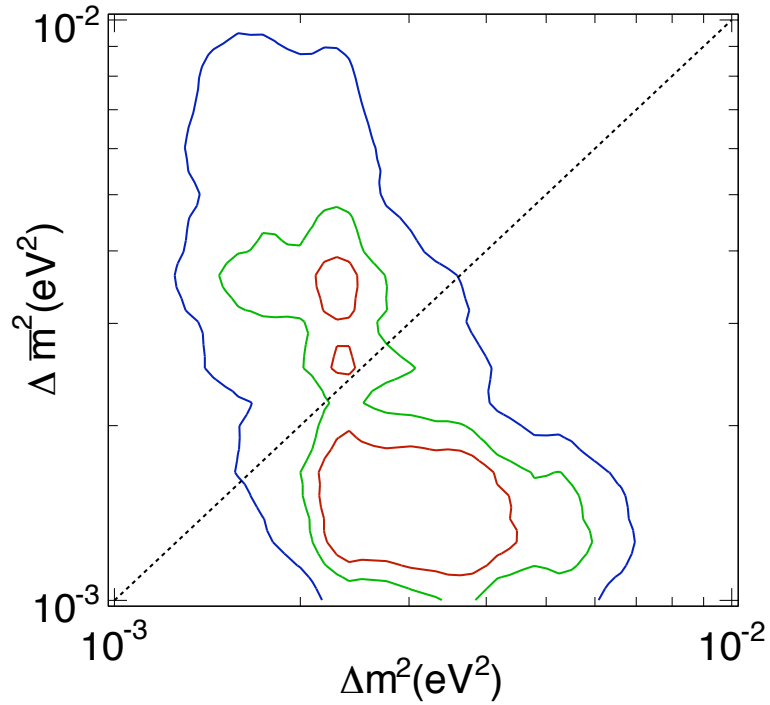


Figure 7.4: Contour plot of the *ad hoc* CPTV model chi-square. Dash line is defined by $\Delta m^2 = \Delta \bar{m}^2$.

anti-neutrinos and compared with the observation using the least chi-square method described in the last chapter. Figure 7.4 shows the contour plot of the least chi-square on the plane of $\Delta m^2 - \Delta \bar{m}^2$.

The best-fit values of the minimum chi-square point is $\Delta m^2 = 3.7 \times 10^{-3} eV^2$ and $\Delta \bar{m}^2 = 1.5 \times 10^{-3} eV^2$. Shown in Fig. 7.4, the 90% confidence level contour covers part of the equal line of neutrino and anti-neutrino mass squared splittings. It is clear that Super-K atmospheric observation has no indication of the LSND scale for anti-neutrino mass squared splitting.

7.3.2 Allowed limits of CPTV

As we see in Sec. 7.1, it is unlikely that Super-K atmospheric observation can be explained by the massless neutrino oscillation induced by the temporal component of the CPTV term in the minimal Standard Model. The scale of the LSND mass squared difference is excluded by Super-K observation. Seeing these facts, even if CPT had been violated, it would have been a sub-dominant effect.

Considering the eigenstates defined by the CPT-odd interaction $(a_L)_{0AB}\bar{L}_A\gamma^0L_B$ same as the mass eigenstates [132], the dispersion relation including this CPTV interaction is as follows:

$$E_i = p + \frac{m_i^2}{2p} \pm a_i, \quad (7.4)$$

here a_i , $i = 1, 2$, is the eigenvalue of the matrix $(a_L)_{0AB}$ and “ \pm ” signs corresponds to neutrinos and anti-neutrinos. Without losing generality, we can define $\Delta a \equiv a_1 - a_2$, assuming $a_1 > a_2$. The survival probability of muon neutrinos (anti-neutrinos) becomes:

$$P_{\nu_\mu/\bar{\nu}_\mu \rightarrow \nu_\mu/\bar{\nu}_\mu} = 1 - \sin^2 2\theta \sin^2 \left(\frac{\Delta m^2 L}{4E} \pm \frac{\Delta a L}{2} \right). \quad (7.5)$$

Where “+” and “-” correspond to neutrino and anti-neutrino oscillations respectively. This CPTV model allows neutrinos and anti-neutrinos to have different mass squared splittings (by absorbing $\pm\Delta a$ into $\frac{\Delta m^2}{4E}$), which is the *ad hoc* model we studied in Sec. 7.3.1 by requiring that the deviations of the mass squared splitting of neutrinos and anti-neutrinos from the best-fit value are same. Equation 7.4 enables us to study the allowed limit of CPTV by treating it as a sub-dominant effect in addition to the dominant mass-

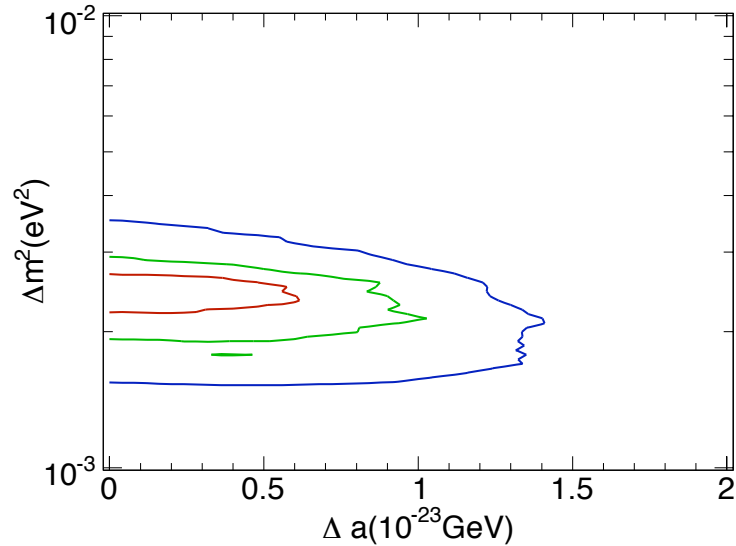


Figure 7.5: Chi-square contours considering CPTV as a sub-dominant effect

induced oscillations. We can assume the mixing is still maximal for this model and the parameter space is spanned by Δm^2 and Δa . Using Eq. 7.5 to produce MC zenith angle distributions and to compare with Super-K atmospheric data, the chi-square contour plot on the $\Delta m^2 - \Delta a$ plane is shown in Fig. 7.5.

The best-fit value of Δa is 0, which means the standard $\nu_\mu - \nu_\tau$ is recovered. At 90% C.L., the limit on the temporal component of the CPTV violating interaction is $\Delta a < 1.05 \times 10^{-23} \text{ GeV}$.

7.4 Discussion

The Standard Model Extension has all the possible terms breaking Lorentz invariance and CPT symmetry, which provides an ideal model to test the low energy effects of LIV and CPTV. Different types of experiments are sensitive to different types of effects. For example, due to the fact that atmospheric neutrinos come from all directions, they are not so advantageous on testing directional LIV effects. Baseline experiments with neutrino

beams with well-defined directions are suitable for testing such effects [133]. However, the wide energy coverage of atmospheric neutrinos gives Super-K advantages for testing effects sensitive to high energies.

As comparisons, the LSND experiments limit on a_L -type SME coefficients is of order 10^{-19} GeV and the limit on c_L -type is of order 10^{-17} [133]. By using the complete data sets of SK-I and SK-II and treating LIV as sub-dominant effect of mass-induced neutrino oscillations, we are able to provide a better limit on c^{TT} than the one set in Ref. [134], which uses published Super-K oscillation analysis results and sets a limit $c^{TT} < 6 \times 10^{-24}$ at 90% C.L. The limit on c^{TT} set by Gonzalez-Garcia and Maltoni in Ref. [135] using both Super-K and K2K data is 0.81×10^{-24} , which is slightly better than our limit. However, our limit on Δa is better than the one set by Gonzalez-Garcia and Maltoni, which is $\Delta a < 3.2 \times 10^{-23}$ GeV at 90% C.L. Besides the different data sets, the main difference between the analysis in Ref. [135] and ours is that our analysis has more systematic uncertainty terms and their effects on the data bins are simulated using Monte Carlo method, while the study by Gonzalez-Garcia and Maltoni is based on a smaller set of systematic uncertainties and the “coupling” factors, *i.e.* the response factors we defined in Chapter 5, are calculated with a more coarse binning. The Super-K limit on c^{TT} is of the same order of the limit set by the MACRO experiment, which is 6×10^{-24} at 90% C.L.

Compared to other types of experiments, limits on LIV and CPTV from neutrino experiments are quite comparable and sometimes even better. Based on the cosmic ray spectrum, limits on the deviation of MAV from the speed of light, *i.e.* $|1 - c|$, can be set. $< \sim 10^{-24} - 10^{-15}$ depending on the particles species and details of the analysis [44, 136]; based on nuclear magnetic resonance frequencies, authors of Ref. [44] interpret the results from Ref. [137] as a limit of 3×10^{-22} on this deviation. As for the limit on CPTV, the $K^0 - \bar{K}^0$ system gives a limit of $m_{K^0} - m_{\bar{K}^0} < 0.44 \times 10^{-18}$ GeV [138]. According to Barger *et al* [132], data from $g - 2$ experiment can be analyzed to probe a_L^0 to the orders

of $\sim 10^{-22} - 10^{-25}$ GeV.

Chapter 8

Neutrino Decay and Neutrino Decoherence

Due to the limited energy and angular resolutions of the Super-K experiment, models predicting “vanishing neutrinos” caused either by neutrino decoherence or by neutrino decay can produce effects which are similar to neutrino oscillations. Testing whether such models could explain what we observe at Super-K is obviously important. On the other hand, both neutrino decoherence and neutrino decay require new physics beyond the Standard Model. With the wide energy and pathlength coverage, Super-K atmospheric neutrino data samples are in an advantageous position to test the effects of these new physics.

The neutrino decoherence phenomenon is due to the dissipative interaction of a neutrino system with an environment [139, 50, 48, 49, 46]. While the neutrino decay models we consider here are based on the assumption that the neutrino mass eigenstates could be unstable [140, 141, 51]. Although the physics behind the two theories are quite different, at the experimental level for Super-K, the expected observations and the techniques to test their validity and limits are very similar — they both cause the disappearance of neutrinos instead of oscillation.

8.1 Neutrino decoherence

Neutrino decoherence may arise when we consider a neutrino system couples to an environment. It could be due to the small violations of quantum mechanics caused by quantum gravity effect [139, 50, 46, 142], a very large neutrino background [48, 49], or flavor dependent interactions into extra dimensions [48]. If the coherence lengths of muon neutrinos are less than the diameter of the Earth due to the presence of those possible dissipative interactions, similar effects to neutrino oscillation would be observed at Super-K — the amount of observed muon type neutrinos is less than predicted. In this section, we test whether neutrino decoherence could be accounted for the Super-K atmospheric neutrino zenith angle distributions.

The coupling to the environment produces mixed quantum states so a Schrödinger equation description for the system is not possible any more, and we are forced to use the Liouville equation instead. Let $\rho(t)$ be the density matrix which is Hermitian and $tr[\rho] = 1$, then the Liouville equation is:

$$\frac{d\rho}{dt} = -i[H_m, \rho]. \quad (8.1)$$

In the case of a two neutrino flavor system, *i.e.*, a two-level system, the Hamiltonian of the system is $H_m = \frac{1}{2E}diag\{m_2^2, m_3^2\}$. Solving the evolution equation 8.1 and computing $tr(|\nu_\mu\rangle\langle\nu_\mu|\rho(t))$ gives the survival probability of the muon neutrinos.

The decoherence effect can be put into the evolution equation in the following fashion [46]:

$$\frac{d\rho}{dt} = -i[H_m, \rho] - \mathcal{D}[\rho]. \quad (8.2)$$

The dissipative interaction term $\mathcal{D}[\rho]$ leads the transitions of the system from pure to mixed states. Operator \mathcal{D} has the dimension of an energy, and its inverse defines the typical coherence length of the quantum system.

Although the physics behind the term $\mathcal{D}[\rho]$ could have different origins, there are certain phenomenological requirements it has to meet in order to make the model physical. The first general one is the so-called *complete positivity* — the mapping from $\rho(0)$ to $\rho(t)$ must be linear, Markovian, and trace-preserving. With this requirement, $\mathcal{D}[\rho]$ must be of Lindblad form [46]:

$$\mathcal{D}[\rho] = \sum_{a=1}^n (\{\rho, D_a^\dagger D_a\} - 2D_a \rho D_a^\dagger). \quad (8.3)$$

Where D_a 's are Lindblad operators arising from averaging away environment dynamic. It is also natural to require that the von Neumann entropy $S = -tr(\rho \log \rho)$ increases with time monotonically and the conservation of the statistical average of the energy of the system, *i.e.*, $\frac{d}{dt}tr(H_m \rho) = 0$, which requires D_a 's are Hermitian and $[H_m, D_a] = 0$ respectively. For a two-level system, D_a can be expanded in terms of Pauli matrices, $D_a = \vec{d}_a \cdot \vec{\sigma}$, where d_a 's are real and the dimension is the square root of an energy. With those three requirements, after some algebra, [46, 47], the survival probability of muon neutrinos with energy E after traveling a distance L can written as:

$$P_{\nu_\mu \rightarrow \nu_\mu} = 1 - \frac{1}{2} \sin^2 2\theta (1 - e^{-\gamma L} \cos \frac{\Delta m^2 L}{2E}). \quad (8.4)$$

Where $\gamma = \sum_{a=1}^n d_a^2$ has the dimension of energy and it's the coherence length of the system under the influence of the environment dynamics. When the coherence length $1/\gamma$ goes to infinity, the survival probability reduces to the pure mass-induced expression

Eq. 1.4.

However, the exact functional form of the parameter γ is not known but considering the fact that Super-K atmospheric neutrino energy spectrum covers several magnitudes, it's certain that our data would be very sensitive to its dependence on the neutrino energy [46]. So, we will try three cases, $n = -1, 0$ and 2 for its power-law dependence on E , $\gamma = \gamma_0(E/GeV)^n$ suggested in [46].

8.1.1 A pure neutrino decoherence model

As pointed out in Ref. [46], in the case of $\gamma \propto 1/E$, even without the contribution from neutrino oscillation, neutrino decoherence can explain atmospheric neutrino data very well. We will first test this pure neutrino decoherence model using SK-I and SK-II atmospheric neutrino data.

The survival probability in this pure decoherence case is:

$$P_{\nu_\mu \rightarrow \nu_\mu} = 1 - \frac{1}{2} \sin^2 2\theta (1 - e^{-\gamma_0 L/E}). \quad (8.5)$$

This situation may happen when two masses are very close to each other or degenerate. Beside the different energy and pathlength dependence, it is obvious that neutrino decoherence will have less neutral current events also due to the fact that neutrinos are just simply “disappearing”. Thus, we will include the NC-enhanced data samples in our analysis also.

Using the same chi-square analysis formalism, replacing the survival probability formula with Eq. 8.5, we are able to find the best values for parameters γ_0 and $\sin^2 2\theta$ for this pure decoherence model to reproduce the SK atmospheric neutrino zenith distributions. Chi-square contours of 68%, 90% and 99% on the $\sin^2 2\theta - \gamma_0$ are shown in Fig. 8.1. The best fit value for this model is: $\gamma_0 = 1.3 \times 10^{-21} GeV$, $\sin^2 2\theta = 1$, and the minimum chi-square at the best-fit point is 987 with the number of degree-of-freedom 853.

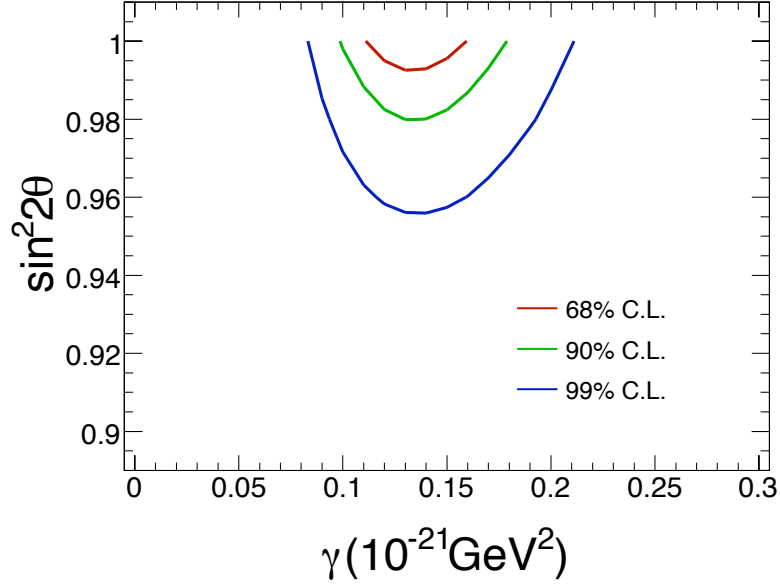


Figure 8.1: Chi-square contours on the $\sin^2 2\theta - \gamma_0$ plane

Compared to the minimum chi-square of the $\nu_\mu - \nu_\tau$ oscillation model, which is 971 with the same number of degree-of-freedom, this pure neutrino decoherence model is excluded at confidence level of 4σ .

Let us check which data samples are contributing to the chi-square difference. Table 8.1 shows the breakdown of the chi-square difference, $\chi_{decoherence}^2 - \chi_{\nu_\mu - \nu_\tau}^2$. The difference of the two models comes from the decoherence model being non-oscillatory. Precisely speaking, we can not simply isolate the contributions from individual data samples since they are being analyzed together and thus correlated with one another. But still, the samples that have the strongest oscillation behavior should prefer the $\nu_\mu - \nu_\tau$ model, while it would be harder for other samples to tell the difference. And, this is what we see in the table. Multi-ring μ -like events, PC events, upward stopping muons and upward non-showering muons provide the strongest preference to oscillation. Because of the bad energy and angular resolutions of NC-enhanced multi-GeV events, the standard oscillation does not account for their zenith angle distribution as well as the decoherence. Overall, the

Table 8.1: Chi-square difference breakdown between the standard oscillation and the decoherence model ($\Delta\chi^2 = \chi_{decoherence}^2 - \chi_{\nu_\mu - \nu_\tau}^2$)

Data Samples	Bins (SK-I+SK-II)	$\chi_{decoherence}^2$	$\chi_{\nu_\mu - \nu_\tau}^2$	$\Delta\chi^2$
Single ring sub-GeV e -like	50+50	104.50	104.06	0.44
Single ring multi-GeV e -like	50+50	110.15	110.75	-0.61
Multi-ring multi-GeV CC e -like	50+50	85.25	85.76	-0.51
Single ring sub-GeV μ -like	50+50	103.66	106.11	-2.44
Single ring multi-GeV μ -like	30+30	67.51	66.79	0.72
Multi-ring μ -like	40+40	81.34	75.49	5.85
NC-enhanced sub-GeV events	10+10	15.22	14.47	0.75
NC-enhanced multi-GeV events	40+40	101.44	104.51	-3.07
PC stopping μ	40+40	127.15	125.77	1.38
PC through-going μ	40+40	104.09	102.14	1.94
Upward stopping μ	10+10	17.79	14.08	3.71
Upward non-showering μ	10+10	18.37	16.86	1.51
Upward showering μ	10+10	25.90	25.97	-0.07
TOTAL	430+430	962.37	952.77	9.6

standard oscillation model explains the SK data better than the decoherence model. The total chi-square difference from the data bins is 9.6.

The chi-square difference from pull terms is 7.4. Figure 8.2 shows the term by term comparison of the pull values between the standard oscillation and the decoherence case. For most of the systematic uncertainty terms, the decoherence model needs to pull them more to fit the data. To see the overall effect, Fig. 8.3 shows their statistical comparison. The decoherence pull terms follow a wider distribution than the standard $\nu_\mu - \nu_\tau$ oscillation model. This is another sign that the decoherence model is disfavored by our data. From Fig. 8.2, we see the largest pull for the decoherence model is the 14th one, which is the PC+Up μ sample-by-sample normalization factor. The decoherence model needs to “pull” the PC+Up μ normalization factor down more than the standard oscillation model to fit the data, which is because the exponential dependence of the survival probability on the L/E value.

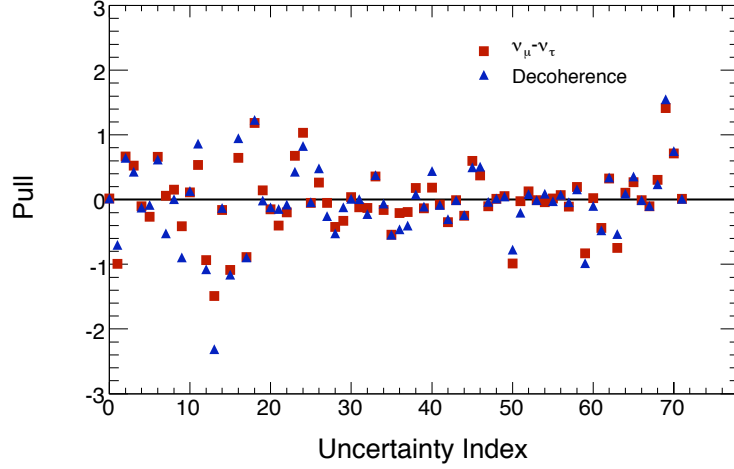


Figure 8.2: Comparison of pull terms of $\nu_\mu - \nu_\tau$ and decoherence

8.1.2 Allowed limits of neutrino decoherence

It is unlikely for neutrino decoherence alone to explain the SK atmospheric neutrino data based on the model comparison study in Sec. 8.1.1. However, we can not eliminate the possibility that neutrino decoherence indeed happens in atmospheric neutrino oscillations as a sub-dominant effect. Then, survival probabilities of neutrinos will depend on both neutrino oscillation and neutrino decoherence, shown in Eq. 8.4. By fitting Eq. 8.4 against SK atmospheric neutrino data, the contribution of neutrino decoherence, assuming its existence, can be separated from neutrino oscillation. We will test three different kinds of energy dependence, $n = 0, 1, 2$, of the decoherence factor $\gamma = \gamma_0(E/\text{GeV})^n$ as suggested in Ref. [46].

The most trivial case, $n = 0$, assumes that decoherence is independent of neutrino energy. The best-fit recovers the standard neutrino oscillation, i.e. $\gamma = \gamma_0 = 0 \text{ GeV}^2$, $\sin^2 2\theta = 1$ and $\Delta m^2 = 2.4 \times 10^{-3} eV^2$. Projecting the chi-square onto $\Delta m^2 - \gamma_0$ plane, confidence contours of 68%, 90% and 99% are shown in Fig. 8.4. At 90% C.L., γ_0 can be as large as $0.76 \times 10^{-23} \text{ GeV}$. Compared to the limit set by Lisi *et al* is $\gamma_0 < 3.5 \times 10^{-23} \text{ GeV}$ [46] based on the published SK-I zenith angle distributions, our

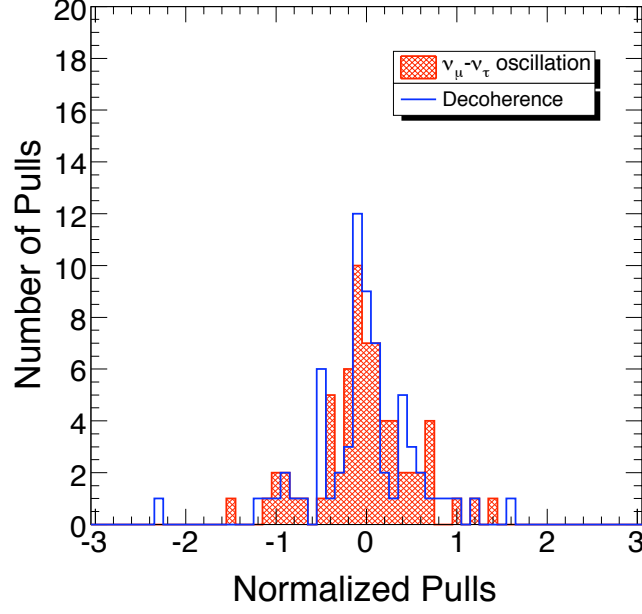


Figure 8.3: Comparison of pull terms of $\nu_\mu - \nu_\tau$ and decoherence

limit is approximately 5 times better due to the fine detail allowed by our analysis and the complete data sets of SK-I and SK-II.

The inverse energy dependence of γ , *i.e.* $\gamma = \gamma_0/(E/GeV)$ is because we do not expect to see different decoherence effects in different frames and L/E is Lorentz invariant [46].

In this case, the best-fit gives a non-zero decoherence: $\gamma_0 = 8 \times 10^{-23} GeV$. As shown in Fig. 8.5, this non-zero value of γ_0 is consistent with zero. The best-fit values for the mixing parameters are $\sin^2 2\theta = 1$ and $\Delta m^2 = 2.4 \times 10^{-3} eV^2$ which are consistent with the $\nu_\mu - \nu_\tau$ best-fit values. At 90% C.L., $\gamma_0 < 0.61 \times 10^{-21} GeV$. The limit set by Lisi *et al* in Ref. [46] is $\gamma_0 < 2 \times 10^{-21} GeV$. Again, our analysis based on the finely binned experimental data gives a much better limit.

The third assumption for energy dependence of γ is inspired by the Planck scale M_P [46]. We generally believe that the low energy effects of Planck scale physics are suppressed by M_P . Considering that γ should have the dimension of an energy, the Planck

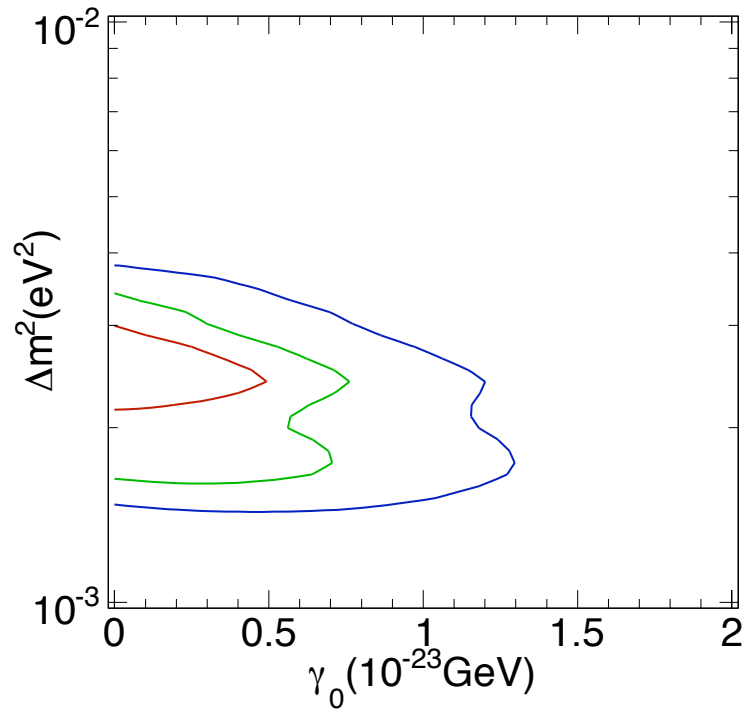


Figure 8.4: Allowed decoherence limits for $\gamma = \gamma_0$ case

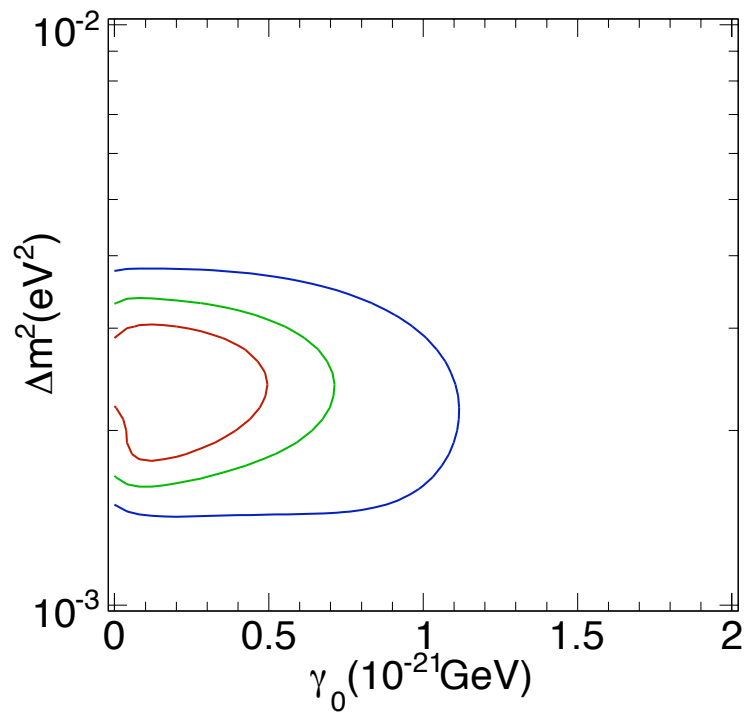


Figure 8.5: Allowed decoherence limits for $\gamma = \gamma_0/E$ case

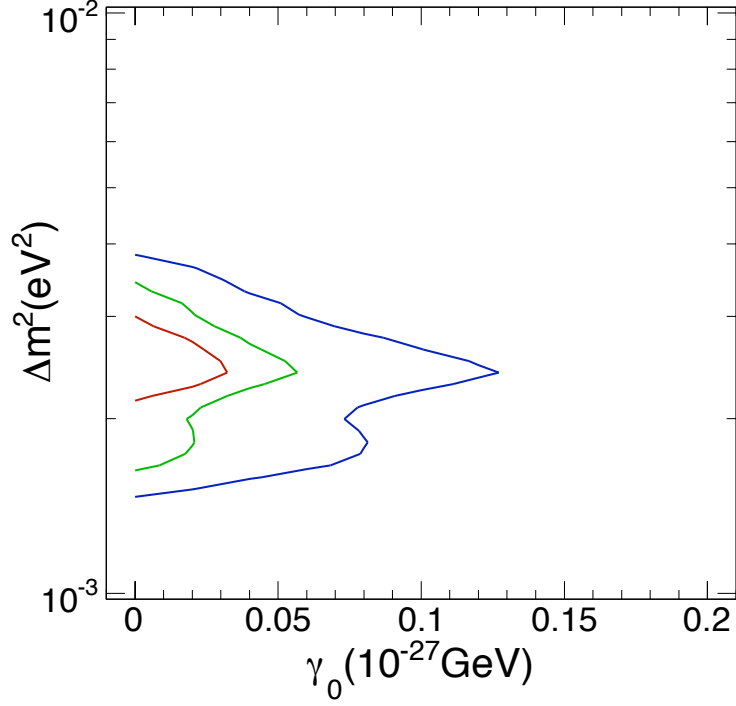


Figure 8.6: Allowed decoherence limits for $\gamma = \gamma_0(E/GeV)^2$ case

scale physics should be suppressed in the form of $\gamma = \gamma_0 E^2/M_P$. By absorbing M_P into γ_0 , we have $\gamma = \gamma_0(E/GeV)^2$ and we still keep $[\gamma_0] = 1$ for convenience.

In this case, the best-fit also gives a non-zero decoherence effect: $\gamma_0 = 4 \times 10^{-29} GeV$. As shown in Fig. 8.5, this non-zero value of γ_0 is consistent with zero. The best-fit values for the mixing parameters are $\sin^2 2\theta = 1$ and $\Delta m^2 = 2.4 \times 10^{-3} eV^2$ which are consistent with the $\nu_\mu - \nu_\tau$ best-fit values. At 90% C.L., γ_0 can be as large as $4.8 \times 10^{-28} GeV$, which is twice better than the limit of $9 \times 10^{-28} GeV$ set by Lisi et al in Ref. [46].

In conclusion, we do not observe any significant non-zero decoherence effects. However, Super-K data can provide very stringent limits which can restrict possible new physics predicting neutrino decoherence effects. One thing we need to point out is that the decoherence models here are purely phenomenological results without the details of fundamental theories involved. They are very general, but it also means that these decoherence param-

eters can only be interpreted given specific theories.

8.2 Neutrino decay

According to the mass-induced neutrino oscillation theory, flavor eigenstates are superpositions of mass eigenstates. However, there is no particular reason to consider the mass eigenstates are stable [51, 141] and the decay of the mass eigenstates can be realized through different theories described in Ref. [140, 141] and references therein.

In the atmospheric neutrino sector, the muon neutrino is a superposition of two mass eigenstates: $|\nu_\mu\rangle = \cos\theta|\nu_2\rangle + \sin\theta|\nu_3\rangle$, where $|\nu_2\rangle$ and $|\nu_3\rangle$ are mass eigenstates. Without losing generality, we can always assume $m_2 > m_3$. If the $|\nu_2\rangle$ state is not stable and its lifetime is τ , the survival probability of ν_μ is:

$$P_{\nu_\mu \rightarrow \nu_\mu} = \sin^4\theta + \cos^4\theta e^{-\alpha L/E} + 2\sin^2\theta\cos^2\theta e^{-\alpha L/2E} \cos\frac{\Delta m^2 L}{2E}, \quad (8.6)$$

where $\alpha = m_2/\tau$ is the experimental parameter we can test since we do not know the value of either m_2 or τ . This survival probability formula can have two simplified cases based on two particular models:

1. If we assume $\nu_2 \rightarrow \bar{\nu}_3 + J$ and J is a massless scalar, then it can be shown that Δm^2 must be greater than 0.73 eV^2 in order to satisfy the constraints from $K \rightarrow \mu + \text{neutral particles}$ decay [140]. Then, the term $\cos\frac{\Delta m^2 L}{2E}$ averages to zero and Eq. 8.6 is simplified into:

$$P_{\nu_\mu \rightarrow \nu_\mu} = \sin^4\theta + \cos^4\theta e^{-\alpha L/E}. \quad (8.7)$$

2. If there exists a sterile neutrino and it does not mix with other neutrinos (or mix very

little),

$$\begin{pmatrix} |\nu_\mu\rangle \\ |\nu_\tau\rangle \\ |\nu_s\rangle \end{pmatrix} = \begin{pmatrix} \cos\theta & \sin\theta & 0 \\ -\sin\theta & \cos\theta & 0 \\ 0 & 0 & 1 \end{pmatrix} \begin{pmatrix} |\nu_2\rangle \\ |\nu_3\rangle \\ |\nu_4\rangle \end{pmatrix},$$

and $\nu_2 \rightarrow \bar{\nu}_4 + J$, then the Δm^2 in Eq. 8.6 is not constrained any more and can be very small. The survival probability becomes:

$$P_{\nu_\mu \rightarrow \nu_\mu} = (\sin^2\theta + \cos^2\theta e^{-\alpha L/2E})^2. \quad (8.8)$$

We will first test how the two simplified cases explain the Super-K zenith angle distributions.

8.2.1 Comparisons between neutrino decay and neutrino oscillation

Using the same least chi-square framework described in Chapter 5, replacing the survival probability $P_{survival}$ with Eq. 8.7 and Eq. 8.8, we can find the best decay parameters reproducing Super-K data. The decay parameters we use are $\sin^2\theta$ and α , here $[\alpha] = 2$.

For pure decay case 1, $P_{\nu_\mu \rightarrow \nu_\mu} = \sin^4\theta + \cos^4\theta e^{-\alpha L/E}$, the best-fit values are $\sin^2\theta = 0.04$ and $\alpha = 1.5 \times 10^{-21} \text{GeV}^2$. The minimum chi-square is 1256.5 with $dof = 853$. Figure 8.7 shows the chi-square contours on $\sin^2\theta - \alpha$ plane. Compared to $\nu_\mu - \nu_\tau$ oscillation, the minimum chi-square is larger by 285.3, which corresponds to an exclusion level 16.9σ . This type of decay is very unlikely to happen.

For pure decay case 2, $P_{\nu_\mu \rightarrow \nu_\mu} = (\sin^2\theta + \cos^2\theta e^{-\alpha L/2E})^2$, the best-fit values are $\sin^2\theta = 0.68$ and $\alpha = 2.2 \times 10^{-22} \text{GeV}^2$. The minimum chi-square is 983 with $dof = 853$. Figure 8.7 shows the chi-square contours on $\alpha - \sin^2\theta$ plane. Compared to $\nu_\mu - \nu_\tau$

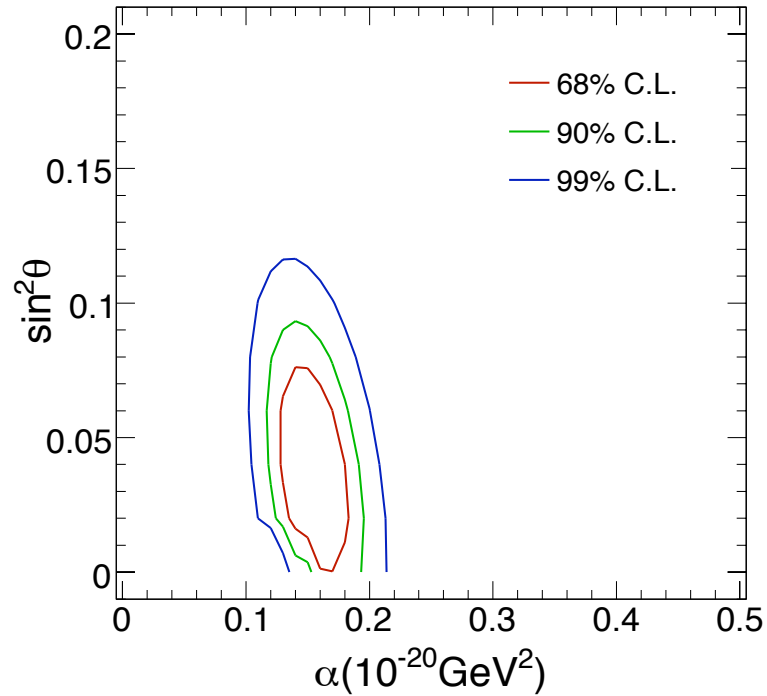


Figure 8.7: Chi-square contours of neutrino decay case I

oscillation, the minimum chi-square is larger by 12, which corresponds to an exclusion level 3.5σ . This type of decay fits Super-K zenith angle distributions much better than case I, however, compared to the standard oscillation, it is still unlikely to happen.

Table 8.2 summarizes the contributions to the chi-square differences from different categories of events. They more or less contribute to the chi-square difference in the same way as the decoherence case. This is because both model produce similar observation effect although the physics behind them is very different. However, the case 2 of neutrino decay fits SK data much better than the neutrino decoherence case. The chi-square difference from data bins is 7.2. The rest of the chi-square difference comes from the pull terms, which is 4.8. Shown in Fig. 8.9, the decay model (case 2) has a wider pull term distribution. Figure 8.10 shows the term-by-term comparisons between the pulls of the standard neutrino oscillation and the neutrino decay case 2. Again, the largest pull in the decay case

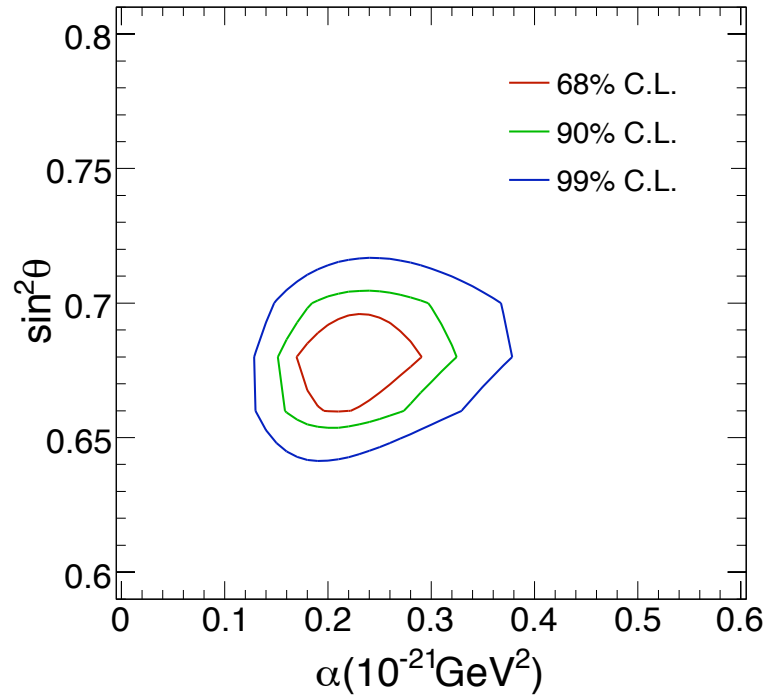


Figure 8.8: Chi-square contours of neutrino decay case II

is the 14th one, which is the sample-by-sample normalization for PC+Up μ events.

8.2.2 Decay as a sub-dominant effect

As we see from the comparisons between neutrino decay and neutrino oscillation, it is unlikely that neutrino decay can account for the Super-K zenith angle distributions. However, this does not mean that neutrino decay is not happening at all — it may coexist with neutrino oscillation. Treating neutrino decay as a sub-dominant effect, we can study the allowed limit on neutrino decay which can provide quantitative guidance to models that predict neutrino decay.

Equation 8.6 has both neutrino oscillation and neutrino decay effects included. Fitting this formula against the Super-K zenith angle distributions, we can find the best parameters for both neutrino oscillation and neutrino decay parameters. In the 3-dimensional

Table 8.2: Chi-square difference breakdown between the standard oscillation and the decay case II model ($\Delta\chi^2 = \chi_{decayII}^2 - \chi_{\nu_\mu - \nu_\tau}^2$)

Data Samples	Bins (SK-I+SK-II)	$\chi_{decayII}^2$	$\chi_{\nu_\mu - \nu_\tau}^2$	$\Delta\chi^2$
Single ring sub-GeV e -like	50+50	104.11	104.06	0.05
Single ring multi-GeV e -like	50+50	110.27	110.75	-0.49
Multi-ring multi-GeV CC e -like	50+50	85.28	85.76	-0.47
Single ring sub-GeV μ -like	50+50	105.28	106.11	-0.83
Single ring multi-GeV μ -like	30+30	65.40	66.79	-1.39
Multi-ring μ -like	40+40	79.06	75.49	3.57
NC-enhanced sub-GeV events	10+10	15.44	14.47	0.97
NC-enhanced multi-GeV events	40+40	102.00	104.51	-2.51
PC stopping μ	40+40	126.75	125.77	0.98
PC through-going μ	40+40	104.97	102.14	2.82
Upward stopping μ	10+10	16.92	14.08	2.84
Upward non-showering μ	10+10	18.30	16.86	1.44
Upward showering μ	10+10	26.18	25.97	0.20
TOTAL	430+430	959.96	952.77	7.19

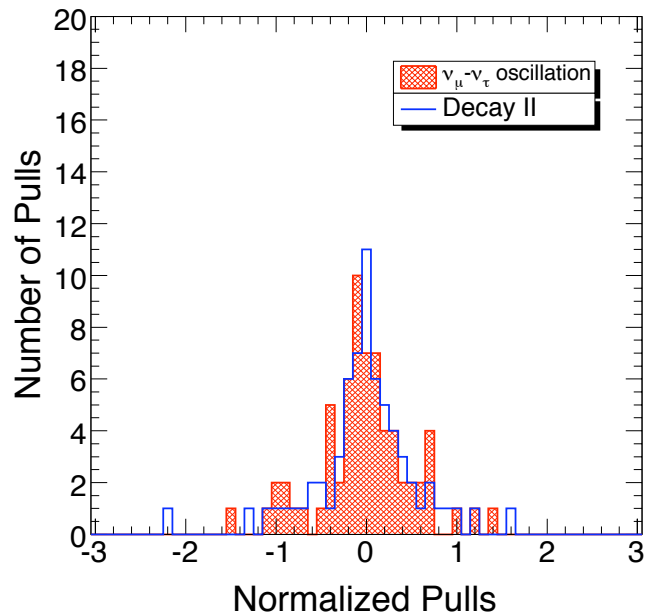


Figure 8.9: Comparison of pull terms of the $\nu_\mu - \nu_\tau$ oscillation and the neutrino decay case

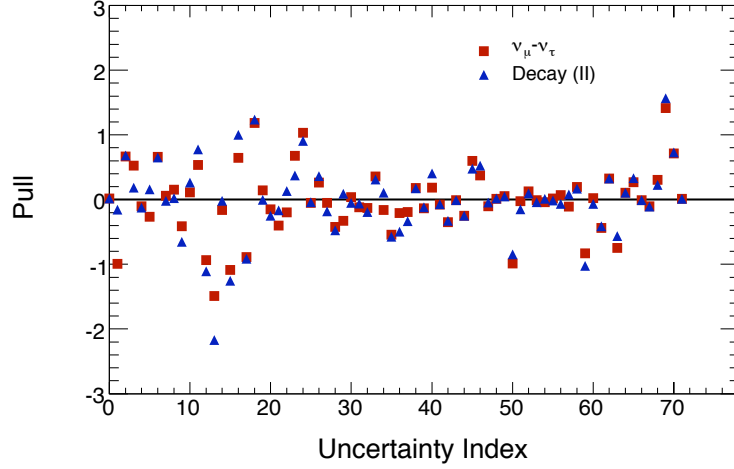


Figure 8.10: Comparison of pull terms of the $\nu_\mu - \nu_\tau$ oscillation and the neutrino decay case 2

parameter space spanned by α ($0 < \alpha < 3 \times 10^{-23} \text{GeV}^2$), $\sin^2 \theta$ and Δm^2 , we find the best-fit values are: $\alpha = 0$, $\sin^2 \theta = 0.45$ and $\Delta m^2 = 2.4 \times 10^{-3} \text{eV}^2$. Super-K obviously prefers zero amount of neutrino decay. Figure 8.11 shows the 2-dimension projection of the 3-dimension chi-square function.

However, the 99% C.L. contour is not completely covered by the parameter space we explored. Since we already know that $\alpha = 0$ is the global minimum in the explored parameter space using linear scale, we can now switch to logarithmic scale to explore larger parameter space. After trying several rounds, we find the proper parameter space to cover the complete 99% C.L. contour. Figure 8.12 shows the complete chi-square contours in a much larger parameter space.

As we can see from the plot, there is actually a local minimum corresponding non-zero neutrino decay. The local minimum is shown more clearly in the one dimension projection of the chi-square function in Fig. 8.13. The parameter values at the local minimum are: $\alpha = 4.5 \times 10^{-22} \text{GeV}^2$, $\sin^2 \theta = 0.7$ and $\Delta m^2 = 2.5 \times 10^{-3} \text{eV}^2$. We see that $\alpha = 0$ is indeed the global minimum and the Δm^2 at the local minimum is of the Super-K atmospheric mass squared splitting scale. The existence of the non-zero local minimum is due to

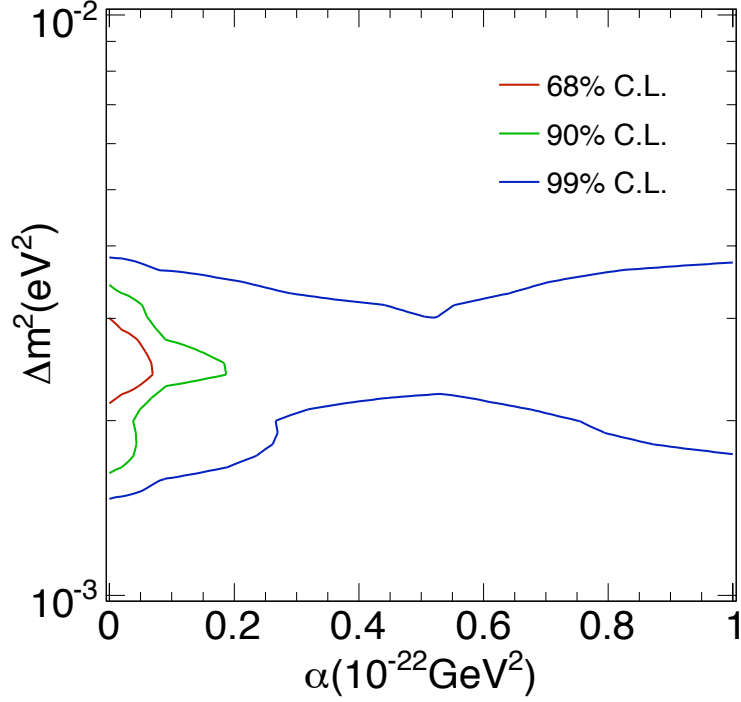


Figure 8.11: Chi-square contours of neutrino oscillation + neutrino decay in linear scale

the fact that Super-K has limited resolutions on neutrino energy and direction and limited statistics around the first oscillation maximum. For models whose oscillation probabilities have L/E dependence, the Super-K L/E analysis has more power to tell the details of these L/E dependence, thus differentiate various models apart more clearly [143]. In the framework of L/E analysis, this local minimum only appears at 99% C.L.

Despite the existence of the local minimum, we can set a limit on α at 99% C.L.: $\alpha < 2.1 \times 10^{-21} \text{GeV}^2$.

8.3 Discussion

Although neutrino decoherence and neutrino decay have completely different physical origins, they produce similar effects — neutrinos vanishing instead of oscillating. In the case

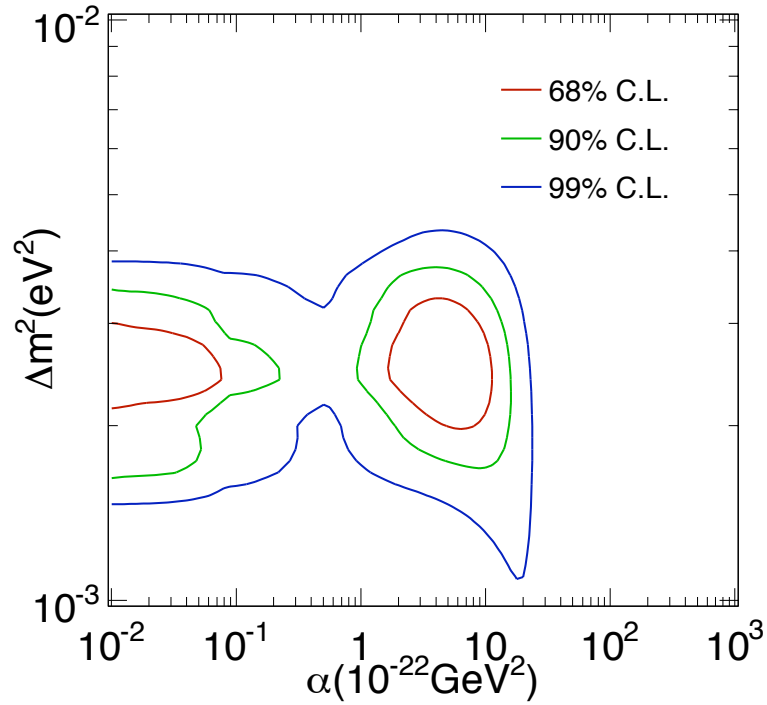


Figure 8.12: Chi-square contours of neutrino oscillation + neutrino decay in logarithm scale

of neutrino decoherence, neutrinos indeed disappear due to the dissipative term $\mathcal{D}[\rho]$ in Eq. 8.2. However, in the case of neutrino decay, neutrinos are not “disappearing”. They decay into either particles which are detectable in our detector or another mass eigenstate which is dominantly a sterile state and does not mix. The power to distinguish neutrino decoherence and neutrino decay from neutrino oscillation mainly comes from the high energy and the long baseline events, which is understandable since both exotic effects have dependences such as $e^{-\gamma L}$ and $e^{-\alpha L/E}$.

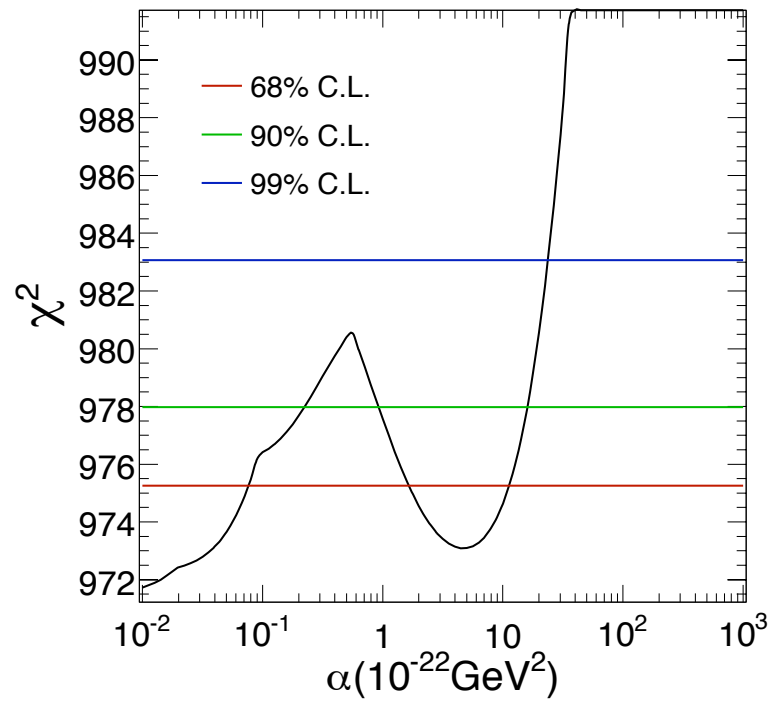


Figure 8.13: The non-zero local minimum of neutrino decay

Chapter 9

Conclusion

Using Super-K atmospheric neutrino data, we compare the standard $\nu_\mu - \nu_\tau$ oscillation model with three types of non-standard ones: the $\nu_\mu - \nu_s$ oscillation which is due to the mass eigenstate mixing, neutrino oscillations induced by LIV and CPTV, and neutrino vanishing caused by neutrino decoherence and neutrino decay. We find that the $\nu_\mu - \nu_\tau$ oscillation induced by mass eigenstate mixing is the best model accounting for the Super-K atmospheric zenith angle distributions.

Furthermore, by treating these non-standard phenomena as sub-dominant effects in addition to the standard $\nu_\mu - \nu_\tau$ oscillation, we are able to constrain the limits of new physics thus provide quantitative guidance to future studies in these fields. Owing to the wide coverage of neutrino energy, neutrino pathlength and the matter density of Super-K atmospheric neutrino events, most of the limits obtained in this dissertation are the best currently available. Our study shows that neutrino oscillation, as a natural interferometer, is a powerful tool to probe new physics beyond the Standard Model.

Appendix A

Outer Detector MC Tuning

Neutrino oscillation analysis of Super-K heavily depends on the comparison between observation and Monte Carlo (MC) simulation. It is essential for us to have a reliable MC which simulates the detector response well. As we mentioned in Chapter 3, the OD functions mainly as a veto detector for cosmic ray muons so we can identify the events happening inside or outside the detector and incoming cosmic ray muons. The accurate performance of the OD simulation has not been an issue until we had the need to further separate PC events into samples with different energies, driven mainly by the requirements of L/E analysis [144, 102]. Statistically speaking, parent neutrinos of PC events which penetrate the OD (through-going) intend to have higher energy than ones that stop in the OD (stopping). This separation means better energy resolution for PC events.

In order to have a comparable MC simulation for the stopping and through-going events, the OD MC performance needed to be improved. It is under this situation that the work described in this chapter was carried out. The separation of PC through-going and stopping events also helps the zenith angle analysis give tighter constraints on mass-squared difference comparing with the binning adopted in the previous atmospheric neutrino analysis of Super-K [63].

A.1 An overview of OD Monte Carlo simulation

As we described in Chapter 3, Super-K MC simulation consists of two parts: first neutrino interactions are generated by NEUT then the final state particles are passed onto the detector simulation `apdetSim` which simulates the detector responses. The signals are recorded as time and charge information for every single PMT in the detector. Ideally, the simulated signals should reproduce the observed signal. But before the tuning, shown in Fig. A.1, it is clear that the OD charge distribution of actual data spreads much wider than MC and follows a different shape. The total number of hits of MC in OD are significantly lower than observation. Data and MC used here are cosmic ray muons stop in ID. The criteria selecting those events will be presented in the next section.

One of the reasons that MC doesn't agree with observation we find is due to the Gaussian single photoelectron (SPE) distribution originally assumed for the OD PMTs. In principle, the SPE distribution of a PMT with good signal-to-noise (S/N) level follows a Poisson distribution and the Poisson distribution can be approximated by a Gaussian if the mean value is large enough. The PMT used in the SK-I OD is Hamamatsu 8 inch R1408. Figure A.2 shows the SPE pulse height distribution provided by Hamamatsu company. Its peak-to-valley (P/V) ratio is not very good (note: the temperature of Super-K water is around 12°C). Another factor worth pointing out is that the OD tubes are also very much aged — they are recycled from IMB experiment. The actual SPE spectrum is even worse, see Fig. A.3. It shows the charge distribution of OD PMT #1101 from dark noise, which is a good approximation of the SPE pulse distribution. Obviously, a Gaussian distribution is not a good model for our OD tubes any more.

Realizing this problematic modeling of the SPE distribution used in the MC simulation, we decide to replace it with an exponential distribution:

Comparison between Data and MC

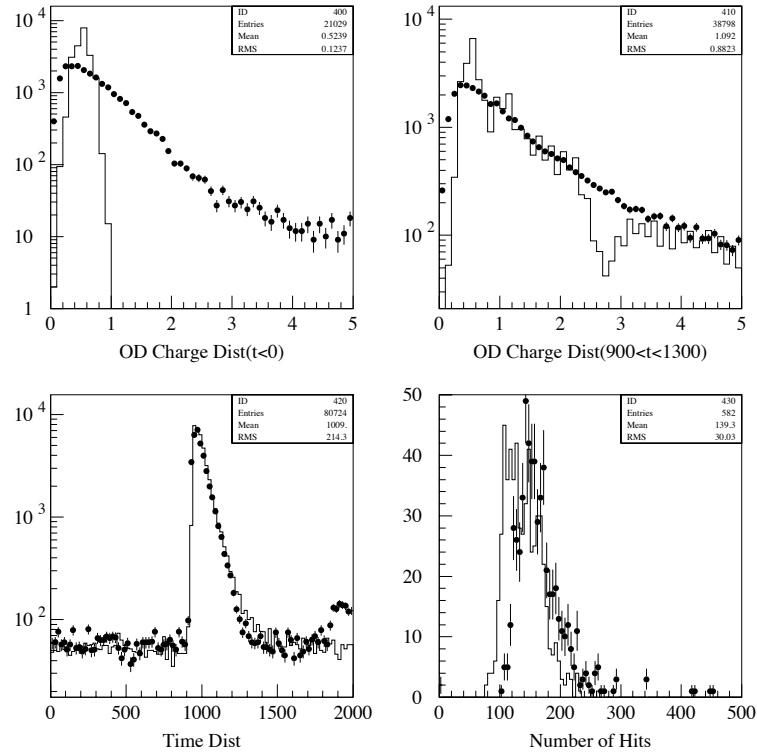


Figure A.1: OD MC performance before this tuning. Upper two: charge distributions inside/outside of the time window and; lower two: hit time and number of hits distributions (dots are observation and solid histograms are MC)

$$p(x) = e^{-x/g}/g, \quad x > 0 \quad .$$

Where x is the pulse height and g is the centroid of the distribution. The value of the centroid is proportional to the gain of the PMT. Figure A.4 shows the distribution of OD PMT centroids obtained by fitting all their charge distributions outside the signal window. It follows a nice Gaussian distribution with mean (g_0) of 0.5 and variance (σ_g) of 0.135, which means the gains of the OD PMTs are well tuned to be close to one another. The g_0

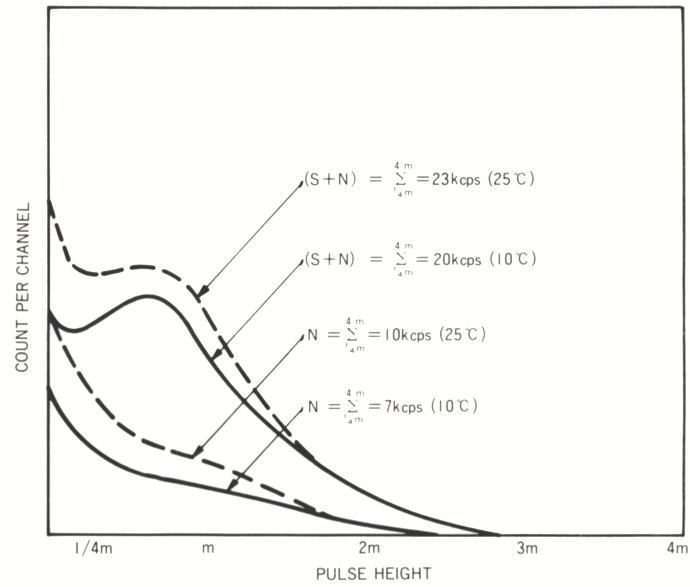


Figure A.2: SPE pulse height distribution of Hamamatsu R1408

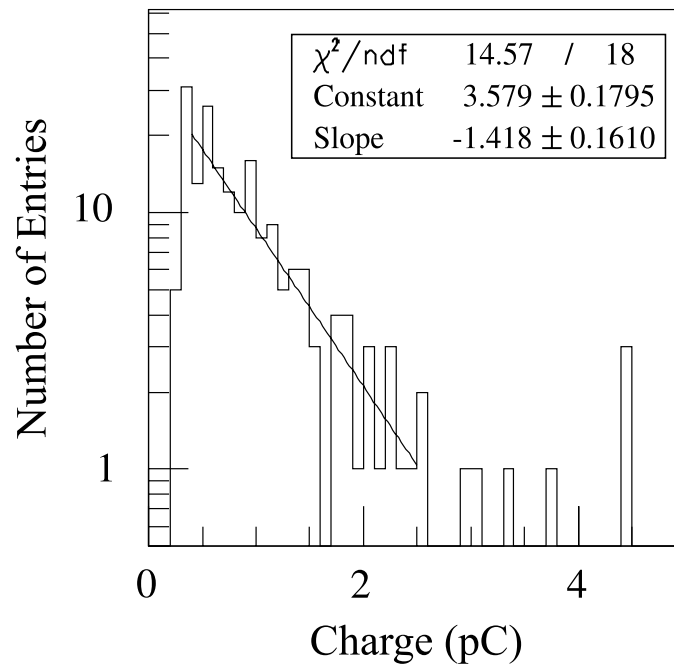


Figure A.3: Measured charge distribution of Hamamatsu R1408

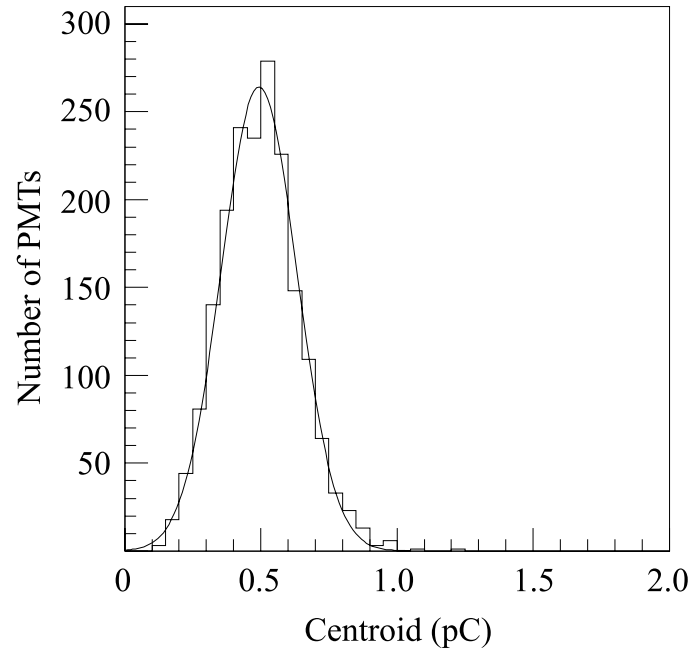


Figure A.4: Distribution of centroids using exponential SPE distribution model (the conversion factor to number of photoelectrons is around 2 in `apdet sim`)

value for OD tubes is fixed at 0.5 but its variance σ_g is a parameter in our simulation.

An exponential distribution are generated by:

$$x = -g \ln(1 - r).$$

Where r is a random number between 0 and 1. Due to plateau near 0 in Fig., we will make a small modification: the SPE spectrum is designed as a joint distribution of an uniform distribution and an exponential. The joint point position is related to the threshold and it will be an parameter in the MC simulation and we call it `plateau`.

A.2 Tuning MC parameters

In order to tune the MC, we need some standard events which we can rely on. Cosmic ray muons stopping in ID are “standard rulers” because we can measure their energies very well using their pathlengths. Following criteria are used to select stopping muons events:

1. Using `muboy` [74] muon fitter to identify stopping muons and further require tight cuts on goodness-of-fits:
 - $G.O.F. > 0.8$: $G.O.F.$ is the goodness-of-fit value which describes how well the expected muon signal reproduce the observed one. Its detailed definition can be found in Ref [74]
 - $f_{cone} > 0.8$: f_{cone} is the fraction of charges inside the reconstructed muon Cherenkov cone in ID. Its definition can be found in Ref. [74]
2. Pathlength in ID greater than $7m$
3. Q_{tot} (total photoelectron in ID) > 8000
4. $d_{wall} > 2m$: stopping point from the nearest wall greater than $2m$.

After reconstructing the stopping muon events, we simulate identical events with the same entry points, directions, and stopping distances.

Now, we have a set of “standard rulers”. The next step is to choose the parameters which need to be tuned. There are many OD MC parameters and most of them are correlated. We decide to tune the following parameters:

1. `plateau`: the joint point of the flat distribution and the exponential distribution for OD PMTs SPE spectrum, confined on $[0, 0.5]$

2. σ_g : it describes the width of the OD PMT gain distribution scaled to an unit Gaussian distribution. We start with 0.27 which is the current value¹
3. $\sigma_{pedestal}$: the variance on the OD discriminator `pedestal` value. We assume `pedestal` follows a Gaussian distribution. Setting the central value at zero for MC is convenient but the width of the Gaussian depends on how well the discriminators are set to the same values.
4. `threshold`: the threshold value of OD discriminators, initially set at 0.3 p.e.
5. σ_{smear} : noise smearing factor which is to simulate the noise between neighboring channels. We assume it follow a Gaussian distribution of $(1, \sigma_{smear})$.

After some trials of comparing MC and observation, we find the following set of parameters with which MC simulation agrees with actual data to the best:

1. `plateau=0.3`
2. $\sigma_g = 0.27$
3. $\sigma_{pedestal} = 0.12$
4. `threshold=0.55`
5. $\sigma_{smear} = 0.5$

With this set of parameters, together with the ones we keep the original values, the new `apdetsim` simulation is shown in Fig. A.5 and Fig. A.6. The MC reproduces actual observation much better. The agreement on OD hits could be tuned better but that will make the charge distribution agreement bad.

¹For the purpose of convenience, we use a unit Gaussian distribution with a scale factor 0.5 to model the centroid distribution of OD PMTs.

Comparison between Data and MC(sim26)

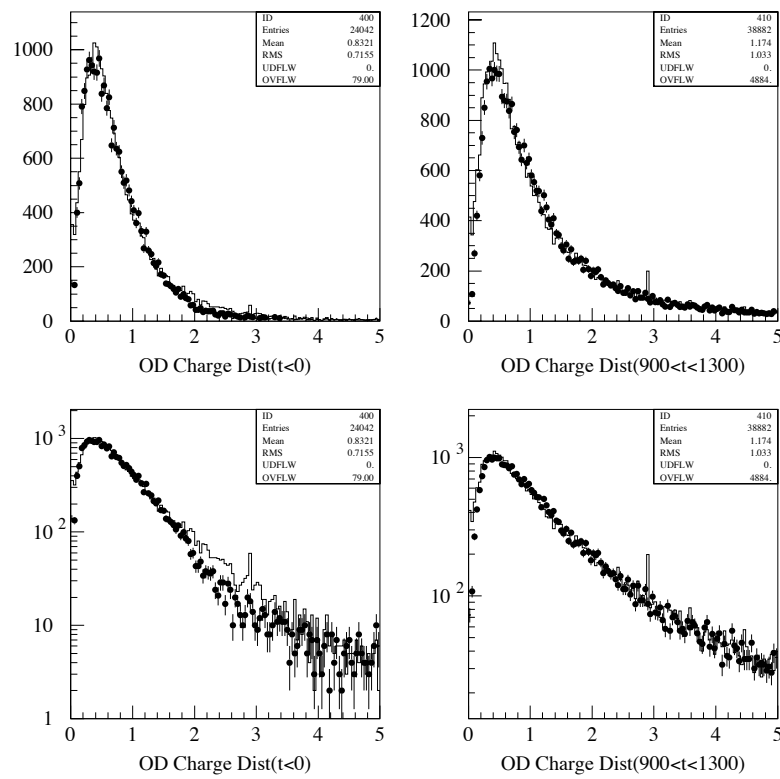


Figure A.5: OD charge distribution inside/outside of time window with the tuned MC simulation compared with observation

Comparison between Data and MC(sim26)

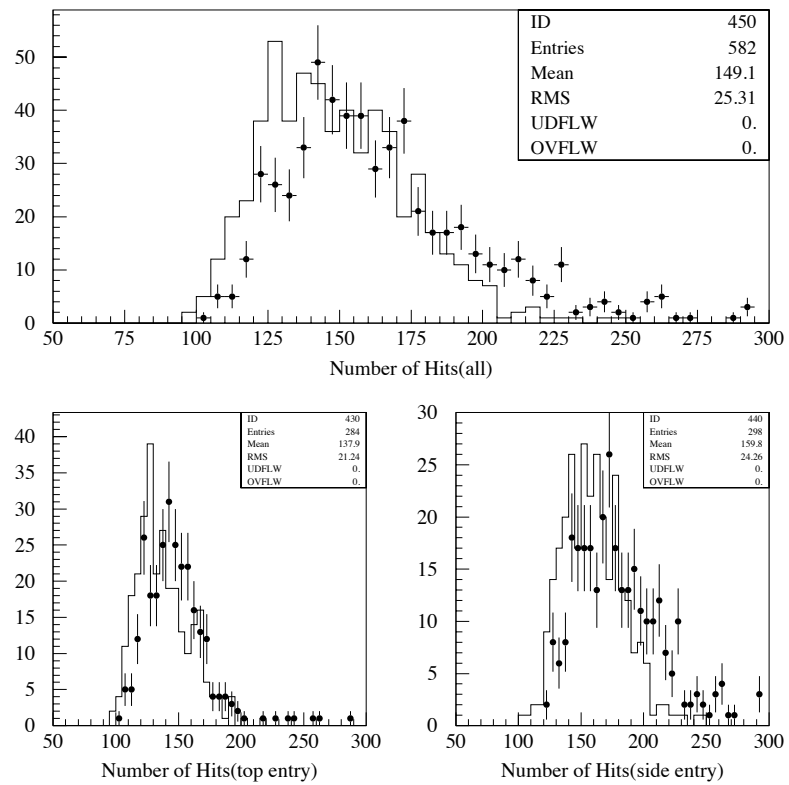


Figure A.6: OD hit distribution with the tuned MC simulation compared with observation

Appendix B

PC Reduction Systematic Uncertainty

Systematic uncertainties of experiments are important in two respects: first, they are the quantitative evaluations of the quality of the experiment; second, they play essential roles in the accuracy of the measured quantities. As an example, I will describe and summarize how we evaluate the systematic uncertainty on the PC reduction efficiency (ϵ_{PC}).

PC reduction is a set of cuts in a computer program used to separate the partially contained neutrino events from the rest. Conceptually, PC reduction efficiency is defined as follows:

$$\epsilon_{PC} = \frac{N_{\text{kept}}}{N_{\text{total}}} .$$

Where N_{kept} is the number of PC events after PC reduction and N_{total} is the total number of PC events in a Monte Carlo sample that should survive the reduction, namely, neutrino interactions with particles that exit into the OD.

In this chapter, I will describe part of the work I did for Super-K I in detail: how we evaluate the systematic uncertainty on reduction steps 1 (PC1) through 4 (PC4), *i.e.*

$\delta_{\epsilon_{\text{PC1-4}}}$. The total systematic uncertainty ($\delta_{\epsilon_{\text{PC}}}$) on the PC efficiency is the quadratic sum of the uncertainties on all the reduction steps, PC1-5:

$$\delta_{\epsilon_{\text{PC}}} = \sqrt{\delta_{\epsilon_{\text{PC1-4}}}^2 + \delta_{\epsilon_{\text{PC5}}}^2} . \quad (\text{B.1})$$

B.1 Overview

PC reduction consists of 5 steps for Super-K I. The time and space information of hits in ID and OD decide whether an event is PC or not. We record the cuts for the first 4 steps, PC1-4, briefly here:

PC1:

- t_{width} : the distribution the time between two consequential hits
- $n_{\text{OD-cluster}}$: number of OD hit clusters

PC2:

- $n_{\text{2nd-cluster}}$: number of hits in the 2nd (ordered by number of hits in the cluster) OD cluster
- n_{min} : number of hits in the first cluster or the rest of OD hits depending on which one is smaller
- n_{outer} : number of hits in the most charged OD cluster
- n_{pe200} : number of photo-electrons within 2 meters in the corresponding ID area of the most charged OD cluster

PC3:

- n_{hit8m} : number of hits in OD within 8 meters of the back extrapolated entrance point on OD wall

PC4:

- $\cos\theta_{fit-first}$: $\theta_{fit-first}$ is the angle between the fitted direction and the line connecting the vertex and the first hit tube in the ID cluster
- $mugood$: the goodness value being a through-going muon
- $mudistance$: the distance it should travel in ID assuming as through-going muon
- d_{corner} : the distance from the fit vertex to the nearest ID corner

These cuts can be grouped into two categories: ID cuts and OD cuts. For ID cuts, we evaluate the uncertainties one by one. The method for each cut is different and details will be described later. Generally speaking, the common part is to check the cut value distribution to see how much uncertainty could have been introduced due to non-perfect agreement between MC and data. Data used are the PC events after the complete PC reduction. There are totally 882 PC events in the sample we use here. For OD cuts, we choose to shift the MC parameters to certain extremes and then exam the effect on the PC reduction. The change on the number of kept PC events is considered as the uncertainty due to OD-related cuts. Then, we have:

$$\delta_{\epsilon_{PC1-4}} = \sqrt{\sum_{i=1}^n \delta_{cut,i}^2 + \delta_{OD}^2} \quad . \quad (B.2)$$

Where $\delta_{cut,i}$ is the uncertainty on each ID cut and δ_{OD} is the uncertainty on all the OD cuts.

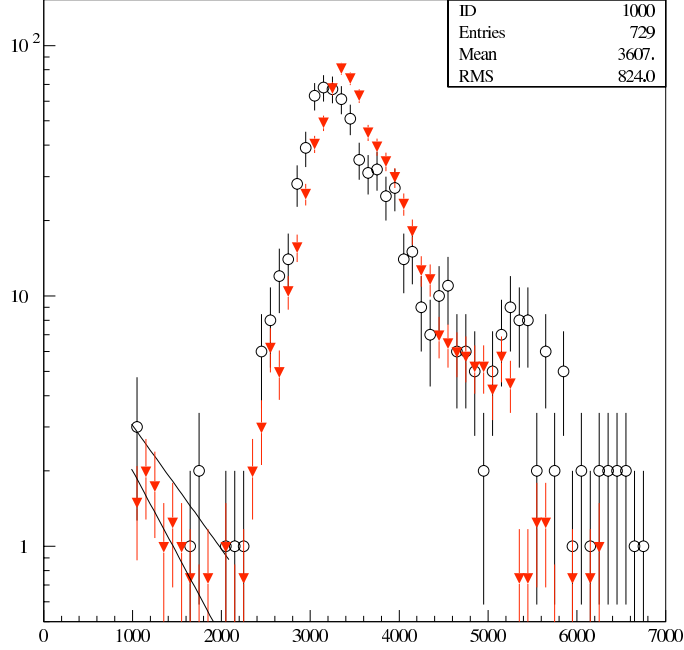


Figure B.1: Distributions of n_{pe200} of the final PC sample. The circles are the final PC sample; triangle are MC

B.2 Evaluation of ID cut uncertainties

There are 5 ID cuts: n_{pe200} , $\cos \theta_{fit-first}$, $mugood$, $mudistance$, and d_{corner} .

Cut n_{pe200} is coupled with the OD cut n_{outer} in the following way: if $n_{pe200} \geq 1000$ or $n_{outer} \leq 6$, then the event is considered as PC. Figure B.1 shows the distributions of final PC samples of both data and MC.

Observing the distribution, we assume that below 2000 hits, n_{pe200} follows an exponential distribution. So fitting both MC and observed data below 2000 using an exponential function and checking the difference of those two integrals on $[0, 1000]$, we conclude that the systematic uncertainty of cut $n_{pe200} \geq 1000$ is 1%.

Figure B.2 shows the distributions of cut $\cos \theta_{fit-first} \geq -0.8$. Assuming flat distributions below -0.5 for both MC and observed data, the difference between them in the rejected region, *i.e.* $[-1, -0.8]$, is 5, thus the systematic uncertainty is $5/(5+882)$ is 0.6%.

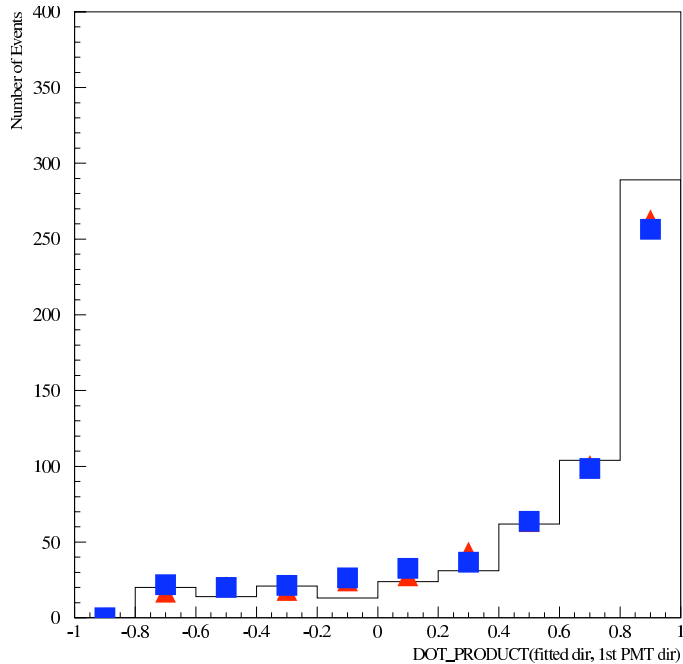


Figure B.2: $\cos \theta_{\text{fit}-\text{first}}$ distributions of MC and observed data

Cuts *mugood* and *mudistance* are coupled together: if $mugood < 0.85$ or $mudistance < 3000$, events are kept as PC events. To evaluate the uncertainty, we examine the change of number of events in the region defined by $mugood \geq 0.85$ and $mudistance \geq 3000$ when we adjust the cut values to compensate for the difference between MC and observed data. Figure B.3 shows the distribution of *mugood* with cut $mudistance \geq 3000$ of the final PC data samples.

The average values of the cut *mugood* are 0.63 and 0.65 for observed data and MC respectively. The difference is 3%. If we adjust the cut according to this difference, the cut value will shift from 0.85 to 0.82. The shift on the cut value will change the number of events in the final observed PC sample by 7. We thus assign the systematic uncertainty of this combined cut of *mugood* and *mudistance* $7/882 = 0.8\%$.

Now, let us examine the cut d_{corner} . Figure B.4 shows the distributions of the final PC samples of both MC and observation. The cut is $d_{\text{corner}} > 150\text{cm}$. We assume the

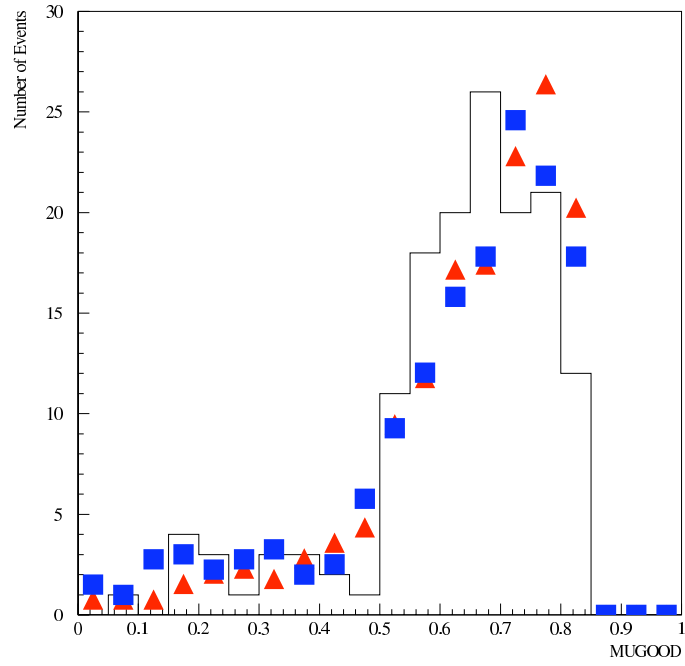


Figure B.3: Distribution of *mugood* with *mudistance* ≥ 3000

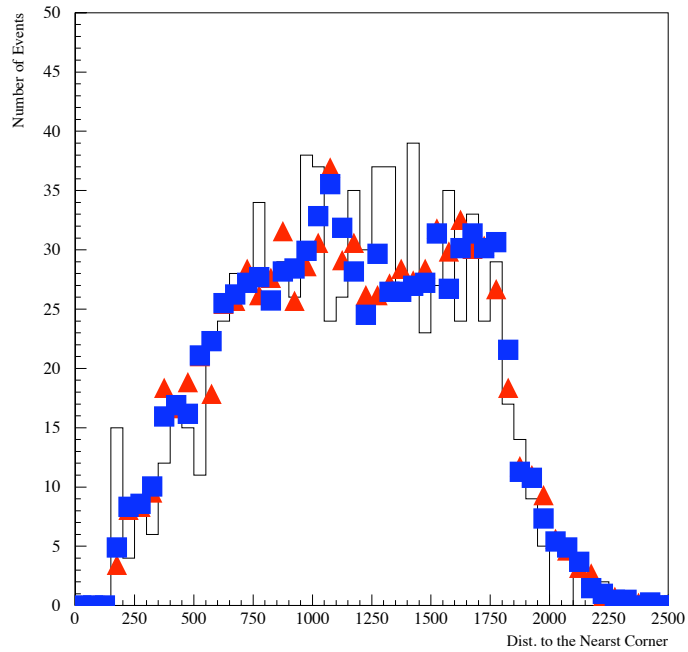


Figure B.4: Distribution of *d_{corner}*

distribution is linear over the range $[0, 500]$ for both MC and observation. Fitting the distributions from 150cm to 500 cm using and extrapolating to rejected region, the difference of MC and observation over the range $[0, 150]$ is 5. Thus, the systematic uncertainty is $5/(882 + 5) = 0.6\%$.

B.3 The Uncertainty of OD cuts

We adopt a different approach for the evaluation of the OD cut uncertainty. The argument is as follow: cut values are decided mainly based on MC simulations, so the uncertainties are introduced in due to the imperfectness of the MC. If we explore the imperfectness of the MC and the change produced by such imperfectness, we can evaluate the uncertainty due to the MC. This uncertainty is the systematic uncertainty of the OD cuts.

Recall the chapter on OD MC simulation, see Fig. , we were aware of the fact that the charge and the hit distributions are not simulated well simultaneously. We decided to pay more attention to the reproduction of the charge distribution chose the parameters corresponding to the better agreement on charge distributions. However, choosing to reproduce the hit distribution better is an equally good set of MC parameters. This uncertainty can be considered as the OD cut uncertainty.

The parameters we choose to tune are:

- Collection efficiency of OD PMTs: 0.22(0.005)
- Threshold of OD discriminator: 0.55(0.01)
- Reflectivity of OD Tyvek: 0.80(0.01)

The values in parentheses are the steps each time we choose a new set of parameters.

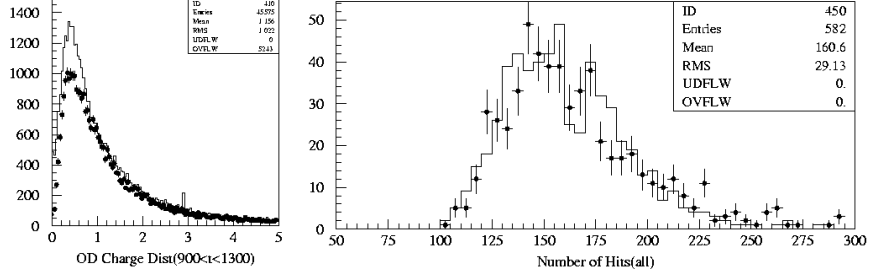


Figure B.5: Distributions produced by another set of MC parameters

After trying several trials, we achieved the distributions shown in Fig. B.5. This set of MC parameters reproduces the OD hit distribution better comparing with the official set of parameters which reproduces the OD charge distribution better.

Using this set of parameters, we regenerate 10 years of MC events and let them go through PC reduction steps 1 through 4. The PC efficiency based on this new set of parameters is 85.9%. Comparing with the efficiency using the official parameter in the OD tuning chapter, 87.3%, we assign 1.4% as the systematic uncertainty produced by all the OD cuts from reduction steps from 1 to 4.

B.4 Summary

Systematic uncertainties are important knowledge of experiment systems. Though its concept is simple, there is no standard ways evaluating them. Using different approaches, we evaluated the systematic uncertainties of different PC reduction cuts for PC1 through 4. According to Eq. B.2, the uncertainty introduced into the PC reduction efficiency $\epsilon_{\text{PC1-4}}$ during steps PC1 through 4 is:

$$\delta_{\epsilon_{\text{PC1-4}}} = \sqrt{\sum_{i=1}^n \delta_{\text{cut},i}^2 + \delta_{\text{OD}}^2} = 1.5\% .$$

The cuts in PC5 are all ID-related and following similar methods described in Sec. B.2, the uncertainty is found to be 2.4%.

In summary, according to Eq. B.1, the systematic uncertainty of PC reduction efficiency is,

$$\delta_{\epsilon_{\text{PC}}} = \sqrt{\delta_{\epsilon_{\text{PC1-4}}}^2 + \delta_{\epsilon_{\text{PC5}}}^2} = 3.2\% \quad .$$

Bibliography

- [1] T. K. Gaisser and M. Honda. Flux of atmospheric neutrinos. *Annual Review of Nuclear and Particle Science*, 52:153–199, 2002.
- [2] Moscow Neutron Monitor. <http://helios.izmiran.troitsk.ru/cosray/main.htm>.
- [3] M. Honda, T. Kajita, K. Kasahara, and S. Midorikawa. A new calculation of the atmospheric neutrino flux in a 3-dimensional scheme. *Physical Review D*, 70:043008, 2004.
- [4] G. D. Barr, T. K. Gaisser, P. Lipari, S. Robbins, and T. Stanev. A three-dimensional calculation of atmospheric neutrinos. *Physical Review D*, 70:023006, 2004. (Also, private communication with the authors. A slightly different flux from the one discussed in the paper is used in the present analysis.).
- [5] G. Battistoni et al. High energy extension of the FLUKA atmospheric neutrino flux. 2003. (The discontinuity seen in Fig. 2.4 has been addressed by later calculations. See: <http://www.mi.infn.it/battist/neutrino.html>.).
- [6] M. H. Ahn et al. Indications of neutrino oscillation in a 250-km long- baseline experiment. *Physical Review Letters*, 90:041801, 2003.
- [7] K. Winter, editor. *Neutrino Physics*. Cambridge University Press, 1991.

- [8] F. Reines and C. Cowan. The neutrino. *Nature*, 178:446, 1956.
- [9] M. Goldhaber, L. Grodzins, and A. W. Sunyar. Helicity of neutrinos. *Physical Review*, 109:1015, 1958.
- [10] G. Danby et al. Observation of high-energy neutrino reactions and the existence of two kinds of neutrinos. *Physical Review Letters*, page 36, 1962.
- [11] M. L. Perl et al. Evidence for anomalous lepton production in e^+e^- annihilation. *Physical Review Letters*, page 1489, 1975.
- [12] K. Kodama et al. Observation of tau neutrino interactions. *Physics Letters B*, page 218, 2001.
- [13] The LEP Collaborations ALEPH DELPHI L3 OPAL the LEP Electroweak Working Group the SLD Heavy Flavour and Electroweak Groups. A combination of preliminary electroweak measurements and constraints on the standard model. *CERN-EP/99-15*, 1999.
- [14] C. Weinheimer. The neutrino mass direct measurements, 2003. The 10th International Workshop on Neutrino Telescopes, Venice, Italy.
- [15] Y. Fukuda et al. Evidence for oscillation of atmospheric neutrinos. *Physical Review Letters*, 81:1562–1567, 1998.
- [16] KATRIN collaboration. KATRIN: A next generation tritium beta decay experiment with sub-eV sensitivity for the electron neutrino mass, 2001.
- [17] S. Wang et al. Weighing neutrinos with galaxy cluster surveys. *Physical Review Letters*, 95:011302, 2005.
- [18] A. D. Dolgov. Neutrinos in cosmology. *Physics Reports*, 370:333, 2002.

- [19] M. Tegmark et al. Cosmological parameters from sdss and wmap. *Physical Review D*, 69:103501, 2004.
- [20] U. Seljak et al. Cosmological parameter analysis including sdss ly-alpha forest and galaxy bias: constraints on the primordial spectrum of fluctuations, neutrino mass, and dark energy. *Physical Review D*, 71:103515, 2005.
- [21] H. Murayama. The origin of neutrino mass. *Physics World*, May, 2002.
- [22] R. N. Mohapatra and A. Y. Smirnov. Neutrino mass and new physics. *Annual Review of Nuclear and Particle Science*, 56:569, 2006.
- [23] S. L. Glashow. *Quarks and Leptons, Cargèse 1979*, page 707, 1980.
- [24] Y. Yanagida. *Proceeding of the Workshop on Unified Theories, Tsukuba*, 1979.
- [25] T. Yanagida. Horizontal symmetry and masses of neutrinos. *Progress of Theoretical Physics*, 64:1103, 1980.
- [26] R. N. Mohapatra and G. Senjanović. Neutrino mass and spontaneous parity non-conservation. *Physical Review Letters*, 44(14):912–915, Apr 1980.
- [27] M. Gell-Mann, P. Ramond, and R. Slansky. *Supergravity edited by D. Freedman et al.* North Holland, Amsterdam, 1979.
- [28] R. D. Peccei. Neutrino physics. *American Institute of Physics Conference Proceeding*, 490:80, 1999.
- [29] B. Pontecorvo. *Soviet JETP*, 7:172, 1958.
- [30] Z. Maki, M. Nakagawa, and S. Sakata. Remarks on the unified model of elementary particles. *Progress of Theoretical Physics*, page 870, 1962.

- [31] V. N. Gribov and B. Pontecorvo. Neutrino astronomy and lepton charge. *Physical Letters B*, 28:493, 1969.
- [32] J. C. Evans, R. Davis, and J. N. Bahcall. Brookhaven solar neutrino detector and collapsing stars. *Nature*, 251:486–488, 1974.
- [33] R. Davis. Nobel lecture: A half-century with solar neutrinos. *Reviews of Modern Physics*, 75:985–994, 2003.
- [34] D. G. Michael et al. Observation of muon neutrino disappearance with the minos detectors and the numi neutrino beam. *Physical Review Letters*, 97:191801, 2006.
- [35] Q. R. Ahmad et al. Direct evidence for neutrino flavor transformation from neutral-current interactions in the Sudbury neutrino observatory. *Physical Review Letters*, 89:011301, 2002.
- [36] K. Eguchi et al. First results from KamLAND: Evidence for reactor anti- neutrino disappearance. *Physical Review Letters*, 90:021802, 2003.
- [37] M. Apollonio et al. Limits on neutrino oscillations from the CHOOZ experiment. *Physics Letters B*, 466:415–430, 1999.
- [38] M. Apollonio et al. Search for neutrino oscillations on a long base-line at the CHOOZ nuclear power station. *European Physics Journal C*, 27:331–374, 2003.
- [39] A. Piepke et al. Final results from the Palo Verde neutrino oscillation experiment. *Progress in Partical and Nuclear Physics*, 48:113–121, 2002.
- [40] L. Wolfenstein. Neutrino oscillations in matter. *Physical Review D*, 17(9):2369–2374, May 1978.

- [41] L. Wolfenstein. Neutrino oscillations and stellar collapse. *Physical Review D*, 20:2634–2635, 1979.
- [42] V. D. Barger, K. Whisnant, S. Pakvasa, and R. J. N. Phillips. Matter effects on three-neutrino oscillations. *Physical Review D*, 22:2718, 1980.
- [43] F. R. Klinkhamer. Neutrino oscillations from the splitting of Fermi points. *JETP Letters*, 79:451–456, 2004.
- [44] S. Coleman and S. L. Glashow. Cosmic ray and neutrino tests of special relativity. *Physics Letters B*, 405:249, 1997.
- [45] V. A. Kostelecky. Neutrino oscillations and Lorentz violation. 2004. Invited talk at the Third International Symposium on Quantum Theory and Symmetries.
- [46] E. Lisi, A. Marrone, and D. Montanino. Probing possible decoherence effects in atmospheric neutrino oscillations. *Physical Review Letters*, 85:1166, 2000.
- [47] T. Ohlsson. Equivalence between neutrino oscillations and neutrino decoherence. *Physics Letters B*, 502:159–166, 2001.
- [48] Y. Grossman and M. P. Worah. Atmospheric ν_μ deficit from decoherence. 1998.
- [49] C. P. Sun and D. L. Zhou. Quantum decoherence effect and neutrino oscillation. 1998.
- [50] Y. Liu, L.Z. Hu, and M.L. Ge. Effect of violation of quantum mechanics on neutrino oscillation. *Physical Review D*, 56(10):6648–6652, Nov 1997.
- [51] V. D. Barger et al. Neutrino decay and atmospheric neutrinos. *Physics Letters B*, 462:109–114, 1999.

- [52] T. K. Gaisser. *Cosmic rays and particle physics*. Cambridge University Press, 1990.
- [53] Y. Shikaze et al. Solar modulation effect on the cosmic-ray proton spectra measured by BESS. 2003. Proceeding of the 28th International Cosmic Ray Conferences (ICRC 2003), Tsukuba, Japan, 31 Jul - 7 Aug 2003, Vol.7, p.4027.
- [54] Climax and Haleakala neutron monitor. <http://ulysses.sr.unh.edu/NeutronMonitor/>.
- [55] J. Alcaraz et al. Cosmic protons. *Physics Letters*, B490:27–35, 2000.
- [56] T. Sanuki et al. Precise measurement of cosmic-ray proton and helium spectra with the BESS spectrometer. *Astrophysical Journal*, 545:1135, 2000.
- [57] G. Battistoni, A. Ferrari, T. Montaruli, and P. R. Sala. The FLUKA atmospheric neutrino flux calculation. *Astroparticle Physics*, 19:269–290, 2003.
- [58] V. Agrawal, T. K. Gaisser, P. Lipari, and T. Stanev. Atmospheric neutrino flux above 1 GeV. *Physical Review D*, 53:1314–1323, 1996.
- [59] M. Fukugita and A. Suzuki. *Physics and Astrophysics of Neutrinos*. Springer-Verlag, 1994.
- [60] M. Fukugita and A. Suzuki. *Physics and Astrophysics of Neutrinos*. Springer-Verlag, 1994.
- [61] K. Kobayashi et al. Search for nucleon decay via modes favored by supersymmetric grand unification models in super- kamiokande-i. *Physical Review D*, 72:052007, 2005.
- [62] J. Hosaka et al. Solar neutrino measurements in super-kamiokande-i. *Physical Review D*, 73:112001, 2006.

- [63] Y. Ashie et al. A measurement of atmospheric neutrino oscillation parameters by super-kamiokande i. *Physical Review*, D71:112005, 2005.
- [64] D. W. Liu et al. Limit on the neutrino magnetic moment using 1496 days of Super-Kamiokande-I solar neutrino data. *Physical Review Letters*, 93:021802, 2004.
- [65] Y. Takenaga et al. Search for neutral Q-balls in Super-Kamiokande II. 2006. to be published on Physical Letters B.
- [66] T. Futagami et al. Observation of the east-west anisotropy of the atmospheric neutrino flux. *Physical Review Letters*, 82:5194–5197, 1999.
- [67] S. Fukuda et al. Search for neutrinos from gamma-ray bursts using Super-Kamiokande. *Astrophysical Journal*, 578:317–324, 2002.
- [68] K. Abe et al. High energy neutrino astronomy using upward-going muons in Super-Kamiokande-I. *The Astrophysical Journal*, 652:198, 2006.
- [69] M. E. C. Swanson et al. Search for diffuse astrophysical neutrino flux using ultra-high energy upward-going muons in Super-Kamiokande I. *The Astrophysical Journal*, 652:206, 2006.
- [70] M. Malek et al. Search for supernova relic neutrinos at Super-Kamiokande. *Physical Review Letters*, 90:061101, 2003.
- [71] S. Desai et al. Search for dark matter WIMPs using upward through-going muons in Super-Kamiokande. *Physical Review D*, 70:083523, 2004.
- [72] M. H. Ahn et al. Measurement of neutrino oscillation by the K2K experiment. *Physical Review D*, 74:072003, 2006.
- [73] Y. Itow et al. The JHF-Kamioka neutrino project. 2001. hep-ex/0106019.

- [74] Shantanu Desai. High energy neutrino astrophysics with Super-Kamiokande, 2004. Boston University doctoral thesis.
- [75] Y. Fukuda et al. The super-kamiokande detector. *Nuclear Instruments and Methods A*, 501:418–462, 2003.
- [76] A. Suzuki et al. Improvement of 20-inch diameter photomultiplier tubes. *Nuclear Instruments and Method A*, 329:299–313, 1993.
- [77] R. Claus et al. A wave shifter light collector for a water cherenkov detector. *Nuclear Instruments and Method A*, 261:540–542, 1987.
- [78] T. Tanimori et al. Design and performance of semicustom analog ic including two tacs and two current integrators for 'super- kamiokande'. *IEEE Trans. Nucl. Sci.*, 36:497–501, 1989.
- [79] Hirokazu Ikeda et al. Front end hybrid circuit for super-kamiokande. *Nuclear Instruments and Methods A*, 320:310–316, 1992.
- [80] M. Nakahata et al. Calibration of Super-Kamiokande using an electron linac. *Nuclear Instruments and Methods A*, 421:113–129, 1999.
- [81] E. Blaufuss et al. ^{16}n as a calibration source for Super-Kamiokande. *Nuclear Instruments and Methods A*, 458:638–649, 2001.
- [82] Y. Hayato. NEUT. *Nuclear Physics Proceeding Supplements*, 112:171–176, 2002.
- [83] D. Casper. The nuance neutrino physics simulation, and the future. *Nuclear Physics Proceeding Supplements*, 112:161–170, 2002.
- [84] C. H. Llewellyn Smith. Neutrino reactions at accelerator energies. *Physics Reports*, 3:261, 1972.

- [85] R. A. Smith and E. J. Moniz. Neutrino reactions on nuclear targets. *Nuclear Physics*, B43:605, 1972.
- [86] D. Rein and L. M. Sehgal. Neutrino excitation of baryon resonances and single pion production. *Annual Physics*, 133:79, 1981.
- [87] D. Rein. Angular distribution in neutrino induced single pion production processes. *Zeitschrift fur Physik*, C35:43–64, 1987.
- [88] T. Kitagaki et al. Charged current exclusive pion production in neutrino deuterium interactions. *Physical Review D*, 34:2554–2565, 1986.
- [89] S. K. Singh, M. J. Vicente-Vacas, and E. Oset. Nuclear effects in neutrino production of delta at intermediate energies. *Physics Letters B*, 416:23–28, 1998.
- [90] D. Rein and L. M. Sehgal. Coherent π^0 production in neutrino reactions. *Nuclear Physics*, B223:29, 1983.
- [91] M. Gluck, E. Reya, and A. Vogt. Dynamical parton distributions of the proton and small x physics. *Zeitschrift fur Physik C*, 67:433–448, 1995.
- [92] Masayuki Nakahata et al. Atmospheric neutrino background and pion nuclear effect for kamioka nucleon decay experiment. *Journal of Physical Society of Japan*, 55:3786, 1986.
- [93] Torbjorn Sjostrand. High-energy physics event generation with PYTHIA 5.7 and JETSET 7.4. *Computer Physics Communications*, 82:74–90, 1994.
- [94] R.D. Woods and D.S. Saxon. *Physical Review*, 95:577–578, 1954.
- [95] L. L. Salcedo, E. Oset, M. J. Vicente-Vacas, and C. Garcia-Recio. Computer simulation of inclusive pion nuclear reactions. *Nuclear Physics A*, 484:557, 1988.

- [96] Glenn Rowe, Martin Salomon, and Rubin H. Landau. An energy dependent phase shift analysis of pion - nucleon scattering below 400-mev. *Physical Review C*, 18:584–589, 1978.
- [97] D. Ashery et al. True absorption and scattering of pions on nuclei. *Physical Review C*, 23:2173–2185, 1981.
- [98] R. Brun and F. Carminati. GEANT detector description and simulation tool. *CERN Programming Library Long Writeup W5013*, 1993.
- [99] C. Zeitnitz and T. A. Gabriel. The GEANT - CALOR interface and benchmark calculations of ZEUS test calorimeters. *Nuclear Instruments and Methods A*, 349:106–111, 1994.
- [100] E. Bracci. Compilation of cross sections : II k^- and k^+ induced reactions. *CERN/HERA*, 72-1, 1972.
- [101] A. S. Carroll et al. Pion - nucleus total cross-sections in the (3,3) resonance region. *Physical Review C*, 14:635–638, 1976.
- [102] Masaki Ishitsuka. L/E analysis of the atmospheric neutrino data from super-kamiokande, 2004. University of Tokyo doctoral thesis.
- [103] Scott Clark. Searches for proton decay with Super-Kamiokande detector, 2006. Boston University doctoral thesis.
- [104] A. Aguilar et al. Evidence for neutrino oscillations from the observation of $\bar{\nu}_e$ appearance in a $\bar{\nu}_\mu$ beam. *Physical Review D.*, 64:112007, 2001.
- [105] J. Hosaka et al. Three flavor neutrino oscillation analysis of atmospheric neutrinos in super-kamiokande. *Physical Review D*, 74:032002, 2006.

- [106] K. Abe et al. A measurement of atmospheric neutrino flux consistent with tau neutrino appearance. *Physical Review Letters*, 97:171801, 2006.
- [107] G. L. Fogli, E. Lisi, A. Marrone, D. Montanino, and A. Palazzo. Getting the most from the statistical analysis of solar neutrino oscillations. *Physical Review D*, 66:053010, 2002.
- [108] S. Fukuda et al. Determination of solar neutrino oscillation parameters using 1496 days of Super-Kamiokande-I data. *Physics Letters B*, 539:179–187, 2002.
- [109] R. N. Mohapatra, S. Nasri, and H.-B. Yu. Seesaw right handed neutrino as the sterile neutrino for LSND. *Physical Review D*, 72:033007, 2005.
- [110] G. C. McLaughlin et al. An active-sterile neutrino transformation solution for r-process nucleosynthesis. *Physical Review C*, 59:2873, 1999.
- [111] D. O. Caldwell, G. M. Fuller, and Y. Z. Qian. Sterile neutrinos and supernova nucleosynthesis. *Physical Review D*, 61:123005, 2000.
- [112] S. Fukuda et al. Tau neutrinos favored over sterile neutrinos in atmospheric muon neutrino oscillations. *Physical Review Letters*, 85:3999–4003, 2000.
- [113] S. Nakayama et al. Measurement of single π^0 production in neutral current neutrino interactions with water by a 1.3-gev wide band muon neutrino beam. *Physics Letters B*, 619:255–262, 2005.
- [114] A.M. Dziewonski and D.L. Anderson. Preliminary reference earth model. *Physics Earth and Planet. Inter.*, 25:297–356, 1981.
- [115] G. L. Fogli, E. Lisi, and A. Marrone. Four-neutrino oscillation solutions of the atmospheric neutrino anomaly. *Physical Review D*, 63(5):053008, Feb 2001.

- [116] Irina Mocioiu, Maxim Pospelov, and Radu Roiban. Breaking CPT by mixed non-commutativity. *Physical Review D*, 65:107702, 2002.
- [117] J. D. Bjorken and S. D. Drell. *Relativistic Quantum Fields*. New York, McGraw-Hill, 1965.
- [118] R. P. Feynman and S. Weinberg. *Elementary particles and the laws of physics*. Cambridge University Press, 1987.
- [119] M. E. Peskin and D. V. Schroeder. *An Introduction to Quantum Field Theory*. Westview Press, 1995.
- [120] A. Zee. *Quantum Field Theory in a Nutshell*. Princeton University Press, 2003.
- [121] S. Coleman and S. L. Glashow. High-energy tests of lorentz invariance. *Physical Review D*, 59:116008, 1999.
- [122] V. A. Kostelecky and M. Mewes. Lorentz and CPT violation in neutrinos. *Physical Review D*, 69:016005, 2004.
- [123] V. A. Kostelecky and M. Mewes. Lorentz and CPT violation in the neutrino sector. *Physical Review D*, 70:031902, 2004.
- [124] D. Colladay and V. A. Kostelecky. Lorentz-violating extension of the standard model. *Physical Review D*, page 116002, 1998.
- [125] Y. Grossman, C. Kilic, J. Thaler, and D. G. E. Walker. Neutrino constraints on spontaneous Lorentz violation. *Physical Review D*, 72:125001, 2005.
- [126] F. R. Klinkhamer and G. E. Volovik. Emergent CPT violation from the splitting of Fermi points. *International Journal of Modern Physics A*, 20:2795, 2005.

- [127] O. W. Greenberg. CPT violation implies violation of Lorentz invariance. *Physical Review Letters*, 89:231602, 2002.
- [128] S. L. Glashow, A. Halprin, P. I. Krastev, C. N. Leung, and J. Pantaleone. Comments on neutrino tests of special relativity. *Physical Review D*, 56:2433, 1997.
- [129] D. Hooper, D. Morgan, and E. Winstanley. Lorentz and CPT invariance violation in high-energy neutrinos. *Physical Review D*, 72:065009, 2005.
- [130] G. Barenboim, L. Borissov, and J. Lykken. Neutrinos that violate CPT, and the experiments that love them. *Physics Letters B*, 534:106–113, 2002.
- [131] M. D. Messier. Testing CPT conservation using atmospheric neutrinos. *The 3rd Meeting on CPT and Lorentz Symmetry (CPT 04), Bloomington, Indiana*, 2004.
- [132] V. D. Barger, S. Pakvasa, T. J. Weiler, and K. Whisnant. CPT-odd resonances in neutrino oscillations. *Physical Review Letters*, 85:5055, 2000.
- [133] L. B. Auerbach et al. Tests of Lorentz violation in muon antineutrino to electron antineutrino oscillations. *Physical Review D*, 72:076004, 2005.
- [134] G. L. Fogli, E. Lisi, A. Marrone, and G. Scioscia. Testing violations of special and general relativity through the energy dependence of $\nu_\mu \leftrightarrow \nu_\tau$ oscillations in the Super-Kamiokande atmospheric neutrino experiment. *Physical Review D*, 60(5):053006, Jul 1999.
- [135] M. C. Gonzalez-Garcia and Michele Maltoni. Atmospheric neutrino oscillations and new physics. *Physical Review D*, 70:033010, 2004.
- [136] O. Gagnon and G. D. Moore. Limits on Lorentz violation from the highest energy cosmic rays. *Physical Review D*, 70:065002, 2004.

- [137] S. K. Lamoreaux et al. New limits on spatial anisotropy from optically-pumped ^{201}Hg and ^{199}Hg . *Physical Review Letters*, 57(25):3125–3128, Dec 1986.
- [138] W-M Yao et al. *Review of Particle Physics*, volume 33. Institute of Physics, 2006.
- [139] S. W. Hawking. The unpredictability of quantum gravity. *Communications in Mathematical Physics*, 87:395 – 415, 1982.
- [140] V. D. Barger, W. Y. Keung, and S. Pakvasa. Majoron emission by neutrinos. *Physical Review D*, 25(3):907–910, Feb 1982.
- [141] V. D. Barger, J. G. Learned, S. Pakvasa, and T. J. Weiler. Neutrino decay as an explanation of atmospheric neutrino observations. *Physical Review Letters*, 82(13):2640–2643, Mar 1999.
- [142] G. L. Fogli, E. Lisi, A. Marrone, and D. Montanino. Status of atmospheric $\nu_\mu \rightarrow \nu_\tau$ oscillations and decoherence after the first K2K spectral data. *Physical Review D*, 67:093006, 2003.
- [143] Super-K Collaboration. Studies of exotic models using L/E analysis. *Internal reports and research in progress*.
- [144] Y. Ashie et al. Evidence for an oscillatory signature in atmospheric neutrino oscillation. *Physical Review Letters*, 93:101801, 2004.